The Pennsylvania State University

The Graduate School

College of Engineering

NOVEL HIGH-ALTITUDE METEOR OBSERVING STRATEGIES EMPLOYED AT THE JICAMARCA RADIO OBSERVATORY

A Dissertation in

Electrical Engineering

by

Boyi Gao

Submitted in Partial Fulfillment

of the Requirements

for the Degree of

Doctor of Philosophy

December 2016

The dissertation of Boyi Gao was reviewed and approved* by the following:

John Mathews
Professor of Electrical Engineering
Dissertation Advisor
Committee Co-Chair

Julio Urbina
Associate Professor of Electrical Engineering
Committee Co-Chair

Victor Pasko
Professor of Electrical Engineering
Graduate Program Coordinator

David Spencer
Professor of Aerospace Engineering

Kultegin Aydin
Professor of Electrical Engineering
Head of the Department of Electrical Engineering

*Signatures are on file in the Graduate School

ABSTRACT

One of the most controversial arguments within the radar meteor community is whether meteor head echoes above the traditional meteor zone (70~130 km above the Earth surface) can be observed by radars or not. Classical ablation theory, which assumes intensive evaporation following a temperature rise up to about 2000K, does not explain meteoroid-produced ionization at high altitudes where the atmosphere is rather thin. The mechanism for ionization at high-altitudes still remains an open question.

When it comes to high-altitude radar meteors (HARMs) experiment, there are three types of ambiguity issues: range ambiguity, Doppler speed ambiguity, and angle-of-arrival ambiguity. Range and Doppler speed ambiguities are related to the length of Inter-Pulse-Period (IPP), but interconnected. Range ambiguity is proportional to the length of IPP. In order to increase the unambiguous range, the length of IPP must be increased. Doppler speed ambiguity, however, is inversely proportional to the length of IPP. Consequently, a tradeoff must be made between range and Doppler speed ambiguities in terms of choosing the length of IPP. A new technique employed in this HARM observation experiment—Alternating Inter-Pulse-Periods (AIPPs)—enables us the resolve these two problems at the same time, without compromising one or the other. Additionally, for radar system with interferometric baselines larger than half of its operating wavelength, such as at Jicamarca Radio Observatory (JRO), angle-of-arrival ambiguity is introduced in the determination of angular positions of detected targets. Therefore, high-altitude radar meteors are usually interpreted as sidelobe contaminations with large ranges but lower altitudes. A new unambiguous, multi-baseline interferometric technique was recently employed for meteor observations at JRO for the first time. It yielded the true angle-of-arrival of HARM events. All these advanced techniques facilitate more accurate data interpretation and better understanding of the physics behind meteor-related phenomena.

The data presented herein are collected from August 4/5, 2014 experiment utilizing novel observing strategies to confirm the existence of high altitude radar meteors. In these observations a sequence of four alternating IPPs, 1723 μs, 1733 μs, 1747 μs, and 1759 μs, was used. The AIPP technique unambiguously recovered the instantaneous Doppler speeds of fast-moving meteor head echoes. The radar transmission was from two quarter-arrays sharing a common diagonal in the East-West direction. Signal reception was via three, quarter-array (Q) receivers and three adjacent (M) module receivers all of the same polarization. One extra quarter-array receiver of perpendicular polarization was also employed to monitor crosstalk. This arrangement offered the usual Q-Q and M-M interferometric baseline-pairs as well as new Q-M baselines that were rotated ~6° from the Q-Q and M-M baselines. For relatively high signal-to-noise ratio (SNR) meteors, this new radar configuration yields ambiguity resolution to the horizon and confirms the existence of HARM events.

TABLE OF CONTENTS

LIST OF FIGURES

LIST OF TABLES

DEDICATION

To Xilin Gao and Yulan Ni, my parents.

To Yixiao Gao, my brother and my inspiration. Congratulations on your achievement of winning a gold medal (22nd place) at the 25th China High School Biology Olympiad and being admitted to Tsinghua University. Your hard work has paid off!

To Shibao Ni, my deceased uncle. Words cannot express how much I love and miss you.

ACKNOWLEDGEMENTS

This research work would not have been accomplished without the support of many people. I am deeply grateful to those who have supported and encouraged me throughout this research.

First and foremost, I would like to thank my Lord and Savior, Jesus Christ, for His love and mercy toward me. I could not reach this far without His many blessings.

I would like to express the deepest appreciation to my advisor and committee chair, Dr. John Mathews, for his excellent guidance, training, patience, and support through the course of my graduate studies.

I would like to thank my committee members, Dr. Victor Pasko, Dr. David Spencer, and Dr. Julio Urbina, for reading through my dissertation and making valuable comments.

I would like to thank Freddy Galindo for code sharing and discussions regarding this research.

I would like to express my thanks to Dr. Marco Milla, the director of Jicamarca Radio Observatorio, for his help of initiating this experiment and collecting data. I would like to thank JRO staff for performing these observations. I also would like to thank Karim Kuyeng and Ramiro Yanque for clarifying many questions regarding these observations.

Finally I would like to thank my friends and the people at Faith Baptist Church who have encouraged, prayed for, and supported me in so many ways, especially Michael Crouse Jr., Dr. Timothy Gilmour, William Bourne, Dr. Jeremy Walter, Timothy Bastian, and Rev. Drew Fenstermacher.

All of you are so appreciated.

Chapter 1

Introduction

A **meteor**, commonly known as a “shooting star” or “falling star,” refers to the bright streak of light which appears in the night sky as a result of a small object, called a **meteoroid**, entering the Earth’s atmosphere. Most meteoroids disintegrate and burn up in the upper atmosphere, so they never reach the Earth’s surface. However, not so very often, a large meteoroid survives the transit through the Earth’s atmosphere and reaches the Earth’s surface. Such an object is classified as a **meteorite**. There are two principal sources of meteoroids entering the Earth’s atmosphere. One is the dust trails produced by sublimating comets as they orbiting the sun, which is the origin of meteor showers such as the Perseids and Leonids. The other is fragments from the asteroid belt beyond Mars, and dust particles from long decayed cometray trails [*Williams*, 1996]. Meteors from the former source are called **shower meteors**. These meteors appear to originate from the same fixed point in the sky, and the point in the sky from which the meteoroid appears to originate is called the radiant of a meteor shower. Meteors from the latter source are called **sporadic meteors**. They do not point back to a known radiant for a given shower, and are not considered part of meteor showers. In radio meteor science, **head echoes** are radar scattering from plasmas immediately surrounding meteoroids that move approximately at the velocity of meteoroids during their atmospheric flights [*Hey et al.*, 1947a; *McKinley and Millman*, 1949]. **Trail echoes** are radar scattering from plasmas left behind in the wakes. **Specular trail echoes** occur when the radar beam lies perpendicular to meteors’ trajectories and the meteoroid plasmas fill successive Fresnel zones. **Non-specular trail echoes** occur when meteoroids travel quasi-parallel to the radar beam and scatter as a result of field-aligned-irregularities [*Close et al.*, 2007].

1.1 The Significance of Studying Meteors

Every day billions of meteoroids impact and disintegrate in the Earth atmosphere. The current estimate of the meteoroid mass flux to Earth varies greatly—5-270 tons per day—with different estimation methods and assumptions [*Ceplecha et al.*, 1998; *Love and Brownlee*, 1993; *Mathews et al.*, 2001; *Nesvorny et al.*, 2010]. However, there is disagreement between different estimates of the total meteor mass flux to the Earth. Sporadic meteors, compared with shower meteors, provide a continuous, thus much greater, mass flux than the showers.

Meteoroids are important because of the hazard they pose to spacecraft. While the particles themselves are small, the impact speeds (up to 72 km/s for particles bound to the sun) are very large, so the potential damage to satellites and other spacecraft is significant. Due to their high speeds, meteoroids could cause mechanical damage upon impact with a spacecraft, or trigger an electrical anomaly even total system failure by producing electromagnetic pulses (EMPs) [*Close et al.*, 2010; *Close et al.*, 2013]. Meteoroids have been known to cause damages to space vehicles from time to time. For example, during the Perseus meteor shower the astronauts at the Mir-I space station heard collisions of meteor bodies, and the on-board solar cell power array was damaged. The Olympus spacecraft lost attitude control due to a gyro anomaly during the 1993 Perseid meteor shower [*Caswell et al.*, 1995]. Although control was restored, the anomaly terminated the mission due to expenditure of fuel. In the same year, NASA postponed the launch of the spacecraft originally due to be launched on August 4th in order to avoid the Perseus meteor storm which was expected on August 12th, and changed the pointing of the Hubble space telescope with remote control command to avoid the dust grains hitting its mirror. On November 18, 1998, the Astronavigation Department of China also took protective measures for their spacecraft to dodge the Leonid meteor storm. In November 1999, based on a proposal put forward by the Research Group of the “Effect of Recent Meteor Showers on the Space Missions of China" at the Purple Mountain Observatory, the Astronavigation Department readjusted the launch time table of the spacecraft "Shenzhou I," trying to avoid its encounter with the Leo meteor storm which took place on November 18th, and therefore guaranteed the successful completion of the "Shenzhou I" mission [*MA et al.*, 2008]. The ADEOS-II and ALOS satellites experienced power system failures during the 2003 Orionids and the 2011 Lyrids, respectively, and both spaceraft were lost. In 2004, the Jason-I satellite noted a momentum transfer, which resulted in a 30 cm change in its semimajor axis. This impact was followed by power spikes that occurred over the next 5 hours. In 2009, a gyro anomaly occurered on the Landsat 5 spacecraft also during the peak of the Perseid shower. The aforementioned incidents are excellent illustrations of why it is necessary to have an accurate knowledge of not only meteoroid mass flux but also its annual and seasonal dependence. Understanding the structure and orbit of a meteoroid is also important in assessing the hazard in case of a collision.

Furthermore, because of their high entry speeds, meteoroids udergo rapid frictiononal heating by collision with air molecules, and their constituent minerals subsequently vaporize. This provides the dominant source of various metals and silicon in the upper atmosphere. These vaporized metal materials are manifest as layers of neutral metal atoms (Na, Fe, Ca etc.) between about 80 and 105 km, and as sporadic E layer between 90 and 140 km. Below 85 km, the metals form compounds such as oxides and carbonates which condense to form meteoric smoke particles. It is suggested that these nm-sized particles provide ice nuclei for the formation of noctilucent clouds in the summer high latitude mesosphere [*Megner et al.*, 2006], and polar stratospheric clouds in the wintertime polar stratosphere [*Curtius et al.*, 2005]. Meteors might well be responsible for depositing metallic materials via sputtering at altitudes higher than the traditional meteor zone (70-120 km above Earth surface) and consequently induce the anomalous radar echoes that come from the upper E region and lower F region of the ionosphere (a.k.a. 150-km echoes) observed at JRO [*Balsley*, 1964].

1.2 The Visibility of Meteors

In order to determine the physical and chemical nature of the meteoroid, one must understand the interaction between the meteoroid and the atmosphere.

The visibility of meteors is a consequence of the high speed of meteoroids in interplanetary space. Before entering the region of the Earth's gravitational influence, their speeds range from a few kilometers per second up to as high as 72 kilometers per second. As they approach the Earth, within a few Earth radii, they are accelerated to even higher speeds by the planet's gravitational field. As a consequence, the minimum speed with which a meteoroid can enter the atmosphere is equal to the Earth's escape speed of 11 kilometers per second. Even at this minimum speed, the kinetic energy of a meteoroid would be 6×10^4 Joules per gram of its mass. This can be compared with the energy of about 4×10^3 Joules per gram produced by chemical explosives, such as TNT. As the meteoroid is slowed down by friction with atmospheric gas molecules, this kinetic energy is converted into heat. Even at the low atmospheric density at altitudes of 100 kilometers (6×10^{-10} gram per cubic centimetre compared with 10^{-3} gram per cubic centimetre at sea level), this heat is sufficient to vaporize and ionize the surface material of the meteoroid and dissociate and ionize the surrounding atmospheric gas as well [*Bronshten*, 1983; *McKinley*, 1961; *Opik*, 1959]. Electronic transitions effected by this excitation of atmospheric and meteoroidal atoms produce a luminous region, which travels with the meteoroid and greatly exceeds its dimensions. At deeper levels in the atmosphere, a shock wave may be produced in the air ahead of the meteoroid. This shock wave interacts with the solid meteoroid and its vapour in a complex way. About 0.1 to 1 percent of the original kinetic energy of the meteoroid is transformed into visible light.

This great release of energy destroys meteoroids of small mass—particularly those with relatively high speeds—very quickly. This destruction is the result both of ablation (the loss of mass from the surface of the meteoroid by vaporization or as molten droplets) and of fragmentation caused by aerodynamic pressure that exceeds the crushing strength of the meteoroid. For these reasons, numerous meteors end their observed flight at altitudes above 80 kilometers, and penetration to as low as 50 kilometers is unusual. Nevertheless, some meteoroids survive to much lower altitudes owing to a combination of relatively low entry speed (< 25 kilometers per second), large mass (>100 grams), and fairly high crushing strength (>10^7 dynes per square centimetre). Those that are recoverable as meteorites lose their kinetic energy before the meteoroid is completely destroyed. They are effectively stopped by the atmosphere at altitudes of 5 to 25 kilometers. Following this atmospheric braking, they begin to cool, their luminosity fades, and they fall to the Earth at low terminal speeds of 100 to 200 metres per second. This "dark flight" of the meteoroid may be several minutes in duration, in contrast to the few seconds of visible flight (Excerpt from Meteor and Meteoroid. (2016). In *Encyclopedia Britannica*. https://www.britannica.com/topic/meteor/Basic-features-of-meteors).

The aforementioned classical ablation theory, which assumes meteoroids collide with atmospheric molecules, intensively vaporize following a temperature rise up to about 2000K, thus produce light and ionization, does not explain meteor-produced ionization and luminosity at high-altitudes (>130km). The mechanism for ionization at high-altitudes still remains an open question.

The ionization and luminosity of most meteors are usually a combination of ablation and fragmentation. As a result, the observed light curves producd by such meteors would be very complex, which could not be explained by any model with only one process considered.

1.3 Radio Observation of Meteors

Meteors have been investigated using radars for decades, and Mathews [2004] gives a detailed history of radar meteors. The earliest published suggestion of meteor effects on radio propagation might be that of Nagaoka [1929]. He described the metallic composition of a meteoroid, and suggested that submicron dust would be scattered along the meteor path and would result in ionization in the ionosphere. But these fine particles would form nuclei to collect the surrounding ions. Therefore, the ionized layer was temporarily disturbed and thus disrupted radio communications. Nagaoka's conclusion, however, was sort of an electron cleanup effect caused by meteoric dust, which was the opposite of those explanations coming afterward. The first reference to possibly confirmed meteor effects on radio propagation was that of Skellett [1931], who stated that "the transmission of radio signals might be markedly affected by the presence of meteors along the path" and that meteor-induced ionization patches caused the sudden drops of the virtual height to the ionosphere. Skellett also explored the mass and energy influxes placed into the ionosphere by meteors in his following paper [*Skellett*, 1932]. He pointed out that meteors expended a large part of their energy in the Kennelly-Heaviside region in the form of ionization along their paths. A companion paper by Schafer and Goodall [1932] observed the changes of the virtual heights of the Kennelly-Heaviside layer during the Leonid meteor shower, and proposed that "meteors might cause sufficient ionization in the upper atmosphere to affect radio-wave propagation." Eckersley [1937] reported some irregular ionic clouds in the E layer of the ionosphere and stated that "there is some nearly constant external source of ionization" based on the features of the observed momentary ionospheric echoes. He also suggested that the responsible agents might be small meteors or high-speed particles of cosmic origin. Skellett [1938] argued that the short-lived ionic cloud was "precisely the sort of thing to be expected from the passage of a small meteor." Pierce [1938] was the first to note the necessary conditions for radar scattering from a meteor-trail. He stated that, “Under these conditions it is seen that no (radar) energy will be reflected to its source unless a perpendicular may be passed from the source to the path of the meteor; and that if this condition is fulfilled the energy so reflected may be calculated very easily.” Later experimental work showed that the main radio echo is obtained only when the aerial beam is directed at right angles to the track of the meteor [*Lovell*, 1947].

Advances in radar and transient display/recording technologies made during World War II provided for very significant improvements in study of radar meteors. Head echoes were first reported by Hey et al. [1947b], who observed the Giacobinid (now called Draconid) meteor storm of 1946 with a 150 kW 55MHz radar system. Hey and Stewart [1947b] reported the first modern-radar observations of meteors. These observations were made in 1946 using a 60 MHz radar system with a 32° HPBW vertically directed antenna. In a remarkable paper, McKinley and Millman [1949] proposed the concept of meteor zone in which the great majority of the radar echoes from meteors occur. They also suggested two mechanisms for the production of meteoric ionization: knietic energy transfer through collisions involving both meteoric and air particles, and radiation energy transfer produced by ultraviolet light from the meteor. The authors further described a possible scattering mechanism of meteor trail echoes, which explains the role of radar view angle with respect to the meteor and the reasons for observational lags of these trail echoes. McKinley propsed in his later work [*McKinley*, 1955] the hypothesis of a ‘moving ball’ type of scattering or reflecting agent accompanying the head of the meteor echoes. McIntosh [1962] distinguished meteor head echoes from trail echoes to clarify the terminologies which caused confusions.

Meteor research using modern High-Power Large-Aperture (HPLA) radar began with Chapin & Kudeki [1994], who gave stunning meteor results from the Jicamarca 50 MHz VHF radar in Peru. In the same year, Pellinen-Wannberg and Wannberg [1994] published their observations of meteors using the European Incoherent Scatter (EISCAT) UHF radar, which operates at a nominal frequency of 930 MHz. Since then, meteor observations have been conducted with most HPLA radar facilities around the world, such as the VHF(46.8MHz) /UHF(430 MHz) radar system at Arecibo Observatory in Puerto Rico [*Mathews et al.*, 1997], the 440 MHz Millstone Hill incoherent scatter radar facility at MIT Haystack Observatory [Erickson et al., 2001], the VHF(163-253 MHz)/UHF (414-440 MHz) ARPA Long-Range Tracking and Instrumentation Radar (ALTAIR) at the U.S. ballistic missile test range on Kwajalein in the Pacific Ocean [Close et al., 2002], the 449.3 MHz Poker Flat Advanced Modular Incoherent Scatter Radar (PFISR) in Alaska [*Mathews et al.*, 2008], the 1290 MHz radar at Sondrestrom Research Facility (SRF) in Greenland [*Mathews et al.*, 2008], the 442.9 MHz Resolute Bay Incoherent Scatter Radar (RISR) in Canada [Malhotra and Mathews, 2011], the 46.5 MHz Middle and Upper atmosphere (MU) radar in Japan [Kero et al., 2012], and the 53.5 MHz Middle Atmosphere Alomar Radar System (MAARSY) located on the Norwegian island of Andøya [Chau et al., 2014]. What is common for these radars is that they all have very large apertures and transmit power in MW.

1.4 High-Altitude Radar Meteors

Reports of high-altitude optical and radar meteors have been given occasionally for 15 years or more. The evidence of high altitude meteors observed using optical systems is convincing. Fujiwara *et al.* [1998] were perhaps the first to unambiguously identify high altitude meteor events. They utilized both image-intensified TV (IITV) cameras and standard photographic techniques to observe Leonid fireballs in 1995 and 1996. They identified two Leonid fireballs with TV-determined onset heights of approximately 160 km and terminal heights at or just below 90 km with estimated errors of no more than a few hundred meters. They reviewed earlier publications and noted that IITV camera systems are significantly more sensitive than standard photographic methods and thus useful for observing meteors at lower luminosity and greater heights than was previously possible. The Fujiwara *et al.* observations were followed by those of Spurný *et al.* [2000b], who also used photographic and all-sky IITV to observe Leonid fireballs. Observing from China during the 1998 shower, Spurný *et al.* identified 13 high-altitude Leonid fireballs summarized in their paper. The all-sky IITV-determined beginning heights of these events ranged from 146 km to 199 km. The corresponding photographically-determined beginning heights ranged from 116 km through 126 km, ending heights ranged from 73 km through 103 km. Nine of the events had all-sky IITV beginning heights clustered near 160 km. During the same campaign Spurný *et al* [2000a] utilized separate narrow field-of-view (FOV; 25° and 25°×35°) IITV systems that they refer to as LLTV (Low-Light TV). These observations yielded seven very-high beginning altitude events. Of these seven events, three were among those reported in Spurný et al. [2000b] using the all-sky IITV cameras. The greater sensitivity and resolution of the narrow-FOV LLTV system revealed significantly higher beginning heights as shown in Figure 1 of Spurný et al. [2000a]. In light of the above results, Koten *et al.* [2001] reported carefully searching their double-station video data archive and finding three meteor events, two eta-Aqarid and one Perseid, with beginning heights near 150 km along with a single Lyrid with a beginning height above 130 km. They gave the light curves for each of these events noting the diffuse, intermediate, and sharp phases. These phases are now considered to correspond to sputtering and rapid diffusion above and pure ablation below with the intermediate regime being a mix of the two. Koten *et al.* [2006], while reviewing past observations and the observational convergence towards sensitivity to high altitude meteors, significantly extended the prior investigations with a tour de force statistical analysis of 164 meteor events with beginning heights above 130 km. Most of these events were from various Leonids showers with a few from other showers and four sporadic meteors—however, their overall database seems highly biased towards showers. Recently Olech *et al.* [2013] reported a large Orionid fireball that was observed with the Polish Fireball Network of video and photographic cameras. They noted a beginning height of 168.4 ± 0.6 km and a terminal height of 69.4 ± 0.6 km with a maximum magnitude of -14.7 ± 1 at 77.7 ± 1.0 km associated with the brightest of four flares. Furthermore, a transition from sputtering to ablative processes was observed at about 115 km altitude.

Despite the convincing evidence of high-altitude optical meteors, the radar meteor community remains skeptical of the claimed high-altitude (>130 km) radar meteor (HARM) observations. There are two major scenarios giving rise to this skepticism. First, unlike single-camera optical observations, HPLA (High-Power, Large-Aperture) radars such as those at Arecibo Observatory are range-sensitive, but they depend on how the narrow radar beam is formed to exclude unwanted returns from off-center beams [*Mathews*, 2004]. That is, for radars without interferometric capabilities, there is no angular information indicating where detected targets are actually located except for beam selectivity. Secondly, for three-receiver radars with interferometric baselines larger than half of the operating wavelength, there is ambiguity in the determination of angular positions of detected targets. Due to angular ambiguity, sidelobe contamination has been the often-cited objection to apparent HARM events.

Reports of HARM events are not only infrequent, but also full of skepticism. Brosch *et al.* [2001] reported observing 1998 and 1999 Leonid radar meteors at altitudes up to about 400 km using a ~1 GHz beam-steering military array radar. These observations, nevertheless, are widely thought to be of space debris and satellites. Khayrov [2009] noted in his figures several meteor events at altitudes up to 218 km. However, whether these meteor events were returns from space debris or meteor-zone meteors in the antenna sidelobe structure is difficult to judge from the plots given. Brosch *et al.* [2010] reported 11 meteors with beginning heights greater than 150 km, and one at 247 km, observed using the European Incoherent Scatter Scientific Association

(EISCAT) VHF radar. These 11 events were out of a total sample of 22,698 meteors detected in 24 hours of observing. Vierinen et al. [2014], nonetheless, persuasively argued that these apparently high-altitude meteors could be interpreted as meteors observed by the strong spillover sidelobes. These sidelobes are caused by the directly exposed feed bridge and are at approximately 45°~80° from the main lobe of the EISCAT VHF antenna. Vierinen et al. further pointed out that neither the range aliasing nor the angular ambiguity was eliminated in the study of Brosch et al. [2013]. Recently Li et al. [2014] reported observations of high-altitude meteor trail-echoes made using the Sanya VHF phased array in China. Even though the Sanya array has interferometric capability, its baselines of $\sqrt{2}\lambda$ (east-west) and $2\sqrt{2}\lambda$ (north-south) result in significant angular ambiguity. Additionally, its 16° (E-W) × 36° (N-S) 3-dB beam is too wide compared to its angular ambiguity region of $\pm 20.7° \times \pm 10.2°$ (using the beam axis as reference), especially along the north-south baseline. In their paper, neither the sidelobe pattern of the Yagi array was discussed, nor was the intrinsic angular ambiguity issue in radar interferometry addressed. Gao and Mathews [2015a] reported a high-altitude meteor event with a beginning height of 170 km using the Jicamarca Radio Observatory (JRO) main array. In addition to providing apparent ranges, they presented further evidences, such as $\mathbf{k} \perp \mathbf{B}$ clustered trail echoes [*Malhotra et al.*, 2007], SNR-matching of meteor head echoes using the radiation pattern of JRO array [*Chau and Woodman*, 2004], and sidelobe analysis [*Gao and Mathews*, 2015b]. They also noted that, theoretically, the principle sidelobes of potential interest are over 50 dB below the main lobe gain. Nevertheless, they still could not conclusively confirm high altitude meteors due to the intrinsic angular ambiguity issue in interferometry.

In this study, we present the novel observing strategies for high-altitude radar meteors at Jicamarca Radio Observatory with the goal to eliminate range, Doppler, and angle-of-arrival ambiguities, and consequently confirm the existence of high-altitude radar meteors.

Chapter 2

Multi-Baseline Interferometric Technique

The results presented herein all derive from observations using Jicamarca Radio Observatory (JRO) 50 MHz radar conducted from 20:19:34, 4th to 12:24:58 5th August 2014 local time (PET). This experiment is specifically designed to observe high-altitude radar meteors (HARMs).

2.1 Jicamarca Radio Observatory

The Jicamarca Radio Observatory (JRO) was constructed in the valley of Jicamarca near Lima, Peru (Figure 2-1). Its main VHF radar operates at 50 MHz, thus has a wavelength of 6 meters in free space. It was built as a joint venture of the National Bureau of Standards and the Instituto Geofísico del Perú in 1960. A major objective of the observatory was to measure properties of the ionosphere and exosphere by analysis of radio signals scattered by the background fluctuations in electron density (known as incoherent scattering).

The main antenna at JRO consists of two superimposed polarizations at right angles to each other (Refer to Figure 2-2). Each polarization of every quarter is connected to separate feed lines, which makes it possible to transmit electromagnetic waves with any desired polarization. The so-called "upper polarization" is in northeast (NE) direction and the "lower polarization" is in southeast (SE) direction [*Ochs*, 1965].

Figure 2-1. Jicamarca Radio Observatory (Wikipedia)

Figure 2-2. The two polarizations of the JRO main array radar (Biblioteca Pleyades).

The antenna is placed 0.3-wavelength above a reflecting screen of poultry netting. The dipoles are spaced one-half wavelength on centers. The whole antenna is divided into quarters. Each quarter is further subdivided into 16 identical square modules, 6 wavelength on one side, containing 288 dipole antennas each. JRO's main antenna is the largest of the incoherent scatter radars in the world. It has 18,432 cross-polarized dipoles covering an area of nearly 85,000 square meters [*Ochs*, 1965].

The maximum transmission line length difference between dipoles in the module is 5 wavelengths. Equal length aluminum coaxial transmission lines 6 inches in diameter run to the centers of all of these modules. These 6-inch lines are connected to the modules by RG-17 cables so that the direction of the main lobe can be steered away from zenith through changing cable lengths.

What makes the Jicamarca Radio Observatory so important is its unique location at the geomagnetic equator. JRO is the equatorial anchor of the Western Hemisphere chain of incoherent scatter radar (ISR) observatories extending from Lima, Peru to Søndre Strømfjord, Greenland. It is the premier scientific facility in the world for studying the equatorial ionosphere. The magnetic dip angle at JRO is about 1°, but varies slightly with altitude and year. The radar can accurately determine the direction of the Earth's magnetic field (**B**) and can be pointed perpendicular to **B** throughout the ionosphere. The study of the equatorial ionosphere is rapidly becoming a mature field due in large part to the contributions made by research on radio science at JRO.

The accurate coordinates of JRO are listed in Table 2-1.

Table 2-1. JRO coordinates and on-axis pointing direction

Latitude	11.951481° S
Longitude	76.874383° W
Altitude	533.253887 meters
Antenna Tilt Angle	1.488312°
Antenna Diagonal Angle	6.166695°
On-Axis Declination	12.881982° S
On-Axis Hour Angle	4.757593 minutes W

2.2 Experiment Setup

Meteor observations reported here were made using the East and West quarter sections of Jicamarca main array (~144 m × ~144 m) with NE (Up) linear polarization for transmission (Refer to Figure 2-3). In total seven simultaneous receiving channels were employed. Channels A, B, and C are quarter receiving channels of the same linear polarization (NE) as the transmitting quarters. Channels D, E, and F are three adjacent 1/64th-array module receivers also of the same polarization (NE). Channel G is an extra receiver that employs the perpendicular-dipoles (SE) in one quarter-section to observe the cross-polarization component of the received signals. The polarizations of all the transmitters and receivers are summarized in Table 2-2.

The JRO array was phased to point on-axis, off-vertical by ~ −1.488° in the y-direction. Note that the x-axis is rotated with respect to the East-West baseline by ~ 51.17° (See Figure 2-3). The two-way (transmission and reception combined) 3-dB beamwidth is ~0.4° (E–W) × 1° (N–S) for quarter receiving configuration, and ~0.5° × 1.4° for its module receiving companion.

Together, channels A-F provide 3 independent interferometric receiving configurations to derive the angular positions of our targets of interest. Quarter-receive (Q-Q) pairs C-A and B-C define our primary x- and y-axes for interferometry (shown in Figure 2-3). The module receive-pairs (M-M) E-F and D-E share the x- and y-axes. However, quarter-module (Q-M) receiving pairs B-F and E-A define another coordinate system with x′- and y′-axes, rotated ~6.226° clockwise with respect to the previously defined coordinates. It is the addition of these extra receiving pairs that breaks the periodic ambiguity pattern of the 1/64th-module antennas, and therefore offers unambiguous angular results in combination with the traditionally utilized Q-Q and M-M interferometric receiving pairs.

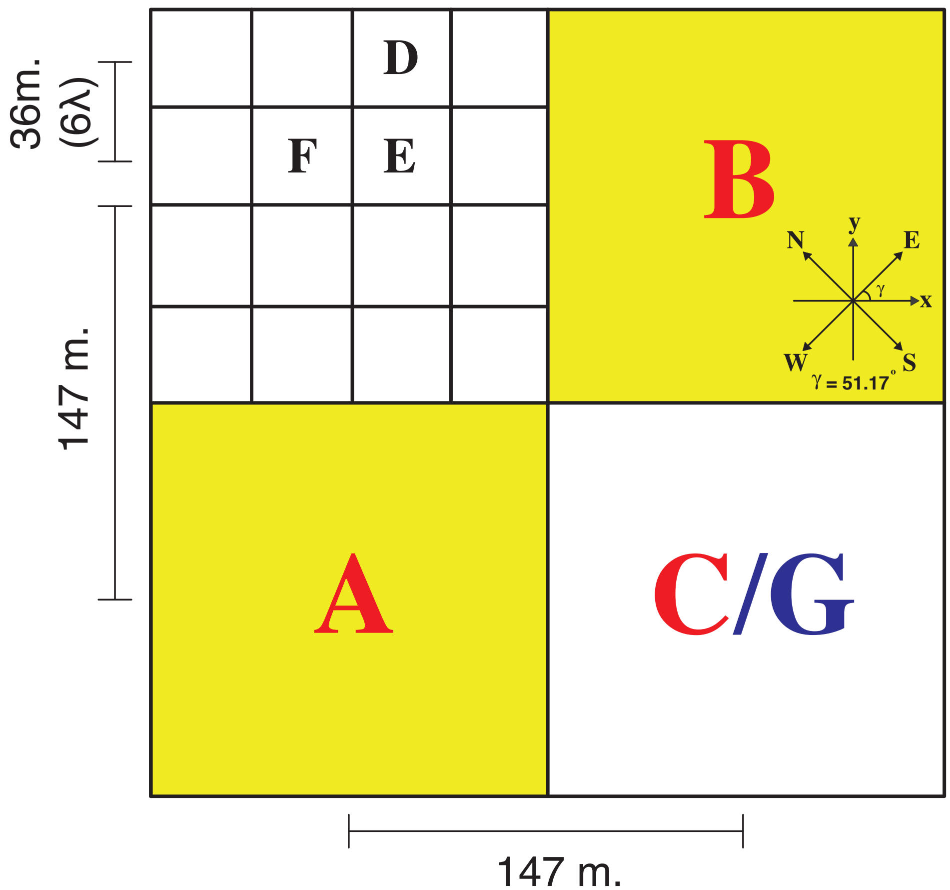

Figure 2-3. Radar configuration for meteor observation experiment. East and West quarters were used for transmission, which are indicated in yellow. Channels A, B and C are quarter receivers while Channels D, E, and F are module receivers. These 6 receiving channels are of the same polarization as the transmitting quarters (NE). Channel G is an extra quarter receiver with orthogonal polarization (SE) to monitor the cross-talks of the detected targets.

Table 2-2. Polarizations of transmitting and receiving channels

Polarization	Up (NorthEast)	Down (SouthEast)
Transmission	East and West quarters	N/A
Reception	Quarter Receivers A, B, C Module Receivers D, E, F	Quarter Receiver G

As we indicate in the abstract and above, note again that we designate the quarter-receiving pairs B-C and C-A as Q-Q (short for quarter-quarter), module-receiving pairs D-E and E-F as M-M (short for module-module), and the new quarter-module-receiving pairs E-A and B-F as Q-M (short for quarter-module). The Q-M receiving configuration has a baseline spacing of 165.98 meters, while Q-Q and M-M have baseline spacings of 147 meters and 36 meters, respectively. Note that each of the interferometric configurations has different periodic angular ambiguity properties across the sky. This feature is the key to resolve angular ambiguities and is discussed in detail in Section 2.3.

Figure 2-4 shows the normalized radiation pattern for one module receiver, one quarter receiver, and two diagonal quarter transmitters, respectively. The module arrays form the basic radiating elements of the main JRO array. Each quarter has 4×4 modules, so its radiation pattern is simply that of the module array multiplied by its corresponding 4×4 array factor. Similarly, the radiation pattern of the transmission is the superposition of that of two diagonally positioned quarter arrays.

The radiation pattern in the far field is calculated based on the relations between visibility spectrum $\mathrm{V}(f, x, y)$ and brightness spectrum $B\left(f, \theta_x, \theta_y\right)$ by Kudeki and Sürücü [1991], which is actually a Fourier transform from 2-dimensional planar space to angular space.

The normalized two-way (transmit-receive) radiation pattern for the quarter (Q) receiving configuration is shown in Figure 2-5. This result reflects the net beam-pattern in space of a single receiver with a constant RCS (radar cross-section) scatterer in the far-field. According to these two figures, there are relatively significant x/y-axis sidelobes (~ -60 dBi below the peak) that might allow contamination—we pay particular attention to this possibility.

The main radar parameters for the meteor mode are summarized in Table 2-3.

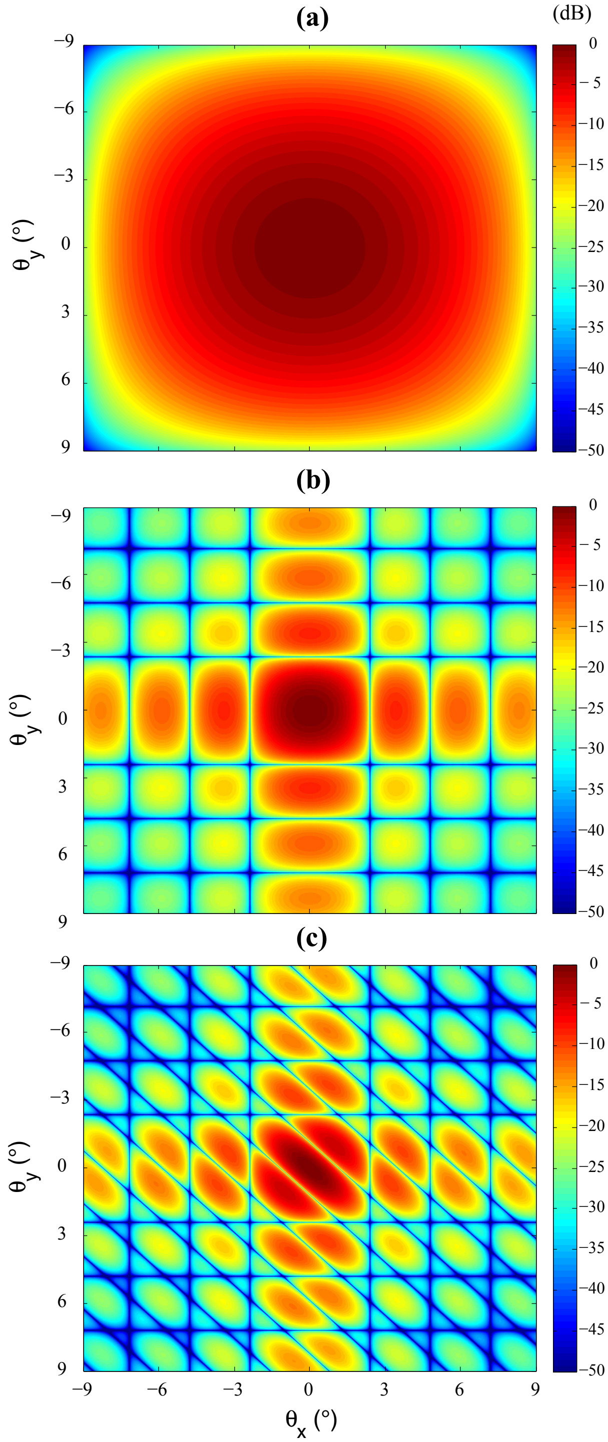

Figure 2-4. Normalized radiation pattern for (a) one Module receiver, (b) one Quarter receiver, and (c) two diagonal quarter transmitters. This result assumes an ideal array composed of ideal elements comprised of coaxial, collinear dipoles in each polarization above a ground screen.

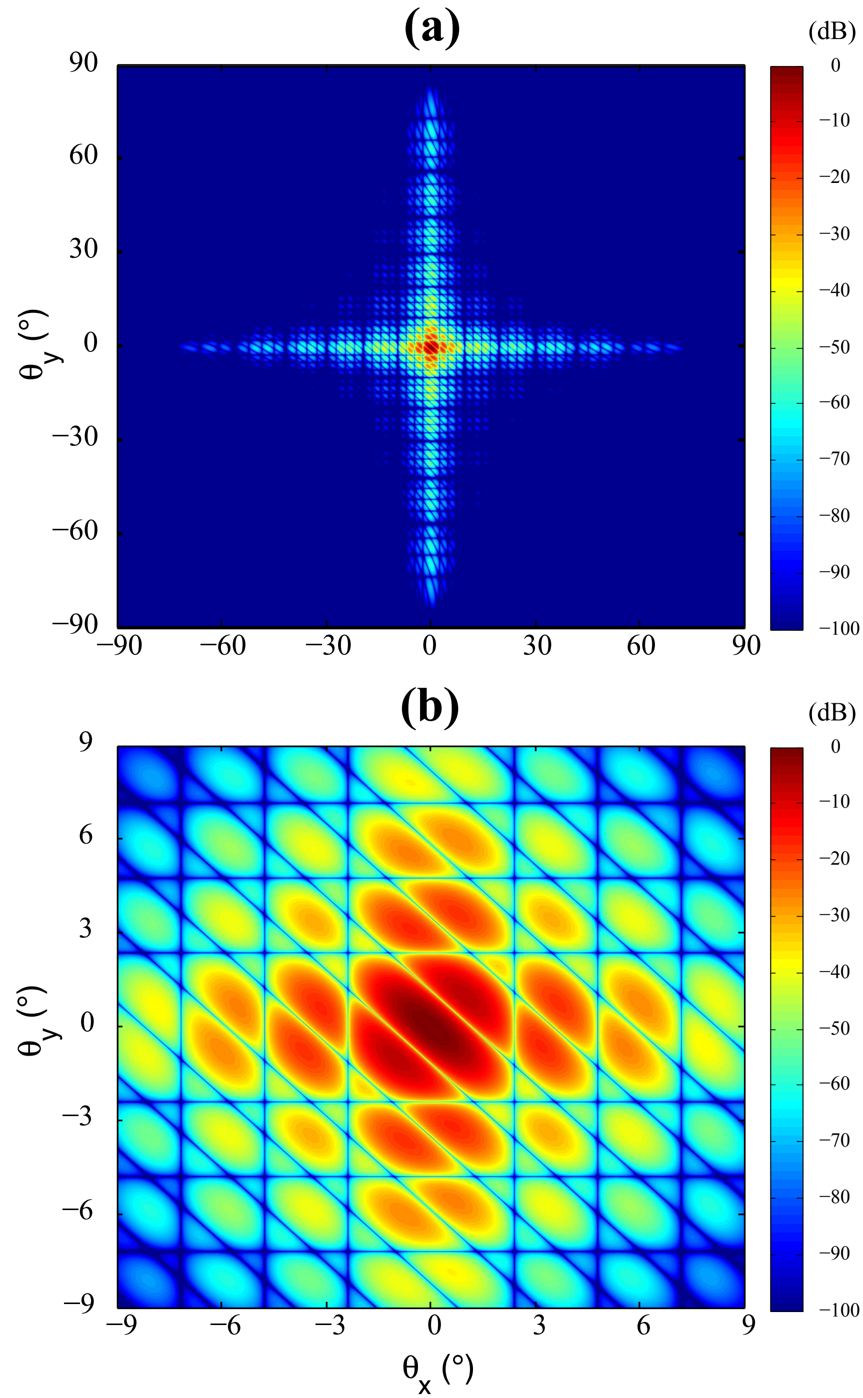

Figure 2-5. Normalized two-way (transmit-receive) radiation pattern for the quarter (Q) receiving configuration. (a) 180° view, and (b) details in 18° view. This pattern assumes an ideal array composed of ideal elements including the coaxial, collinear (COCO) antenna elements and ground screen.

Table 2-3. Radar parameters for meteor observations

IPPs	Pulse Width	H_0	dH	H_f	Number of Channels
258.45 km (1723 μs)	3 km (20 μs)	49.95 km	150 m (1 μs)	256.2 km	7
259.95 km (1733 μs)					
262.05 km (1747 μs)					
263.85 km (1759 μs)					

2.3 Angular Ambiguity and the Effective Unambiguous Region

In interferometry, the angular position of a target of interest is derived using the following formula:

$$\sin(\theta) = \frac{\lambda}{d}\frac{\Delta\phi}{2\pi} \tag{2.1}$$

where λ is the radar wavelength, d is the distance between the phase centers of two antennas with identical receivers, $\Delta\phi$ is the phase of cross-correlation function (CCF) of the raw voltages from the two receivers that reflects the phase-path difference between the target in the far field and the receivers.

However, $e^{j\Delta\phi}$ is a periodic function with period 2π. Conventionally $\Delta\phi$ is defined in the interval of $[-\pi, \pi]$. Hence the resultant angular position of the target is in the range of

$$\theta \in \left[-\sin^{-1}\left(\frac{\lambda}{2d}\right), \sin^{-1}\left(\frac{\lambda}{2d}\right)\right] \tag{2.2}$$

Thus, when two receiving antennas are spaced by a distance of more than λ/2, a periodic angular ambiguity is introduced due to the uncertainty of multiples of 2π in calculating the phase difference $\Delta\phi$.

This problem can be dealt with by using multiple antenna array elements with specific spatial arrangement along the same baseline [*Jones et al.*, 1998]. For example, if we use three antennas along the same baseline, but with different spacings, d_1 and d_2, the effective unambiguous region becomes

$$\theta_E \in \left[-\sin^{-1}\left(\frac{\frac{\lambda}{2}}{GCF(d_1, d_2)}\right), \sin^{-1}\left(\frac{\frac{\lambda}{2}}{GCF(d_1, d_2)}\right)\right] \tag{2.3}$$

where $GCF(d_1, d_2)$ is the greatest common factor of d_1 and d_2.

In the case of the well-known Jones' configuration [*Jones et al.*, 1998], $d_1 = 2\ \lambda$, $d_2 = 2.5\ \lambda$, therefore $GCF(d_1, d_2) = 0.5\lambda$. This yields an effective unambiguous region of [-90°, 90°]—i.e., from horizon-to-horizon in the baseline direction. In principle, when two such orthogonal baselines are employed, any target (with sufficient SNR) can be located unambiguously across the whole sky. Note that $GCF(d_1, d_2)$ is not necessarily an integer—it more convenient to measure it in terms of operating wavelength λ.

In these observations, the Q-Q and Q-M baselines are at an angle of ~6.226°. No simple mathematical formula is found for the effective unambiguous region, mainly due to the complexity introduced by the rotation of new baselines relative to the other two. Instead, a simple technique called "ambiguity mapping" is introduced to obtain a straightforward and intuitive explanation of how this newly-introduced multi-baseline interferometry functions. The basic idea is as follows. A stationary point target is assumed to be at the beam center (near to zenith in this case), and multiples of 2π are added into phase $\Delta\phi$ to obtain all of the possible ambiguous angular positions all over the whole sky. Then compare all the ambiguity results from the different baselines to determine if they overlap each other at locations(s) other than beam-center. If there is no overlap, the effective unambiguous region is all-sky—i.e., [-90°, 90°]. Otherwise, half of the overlapping angular position is the boundary of the effective unambiguous region.

In these observations, the results of ambiguity mapping from Q-Q are used as reference to compare with those from Q-M and M-M. The combination of these three baselines is used to de-alias angular ambiguity in interferometric interpretation of each event.

To further illustrate the concept of ambiguity mapping, possible ambiguous angular positions near zenith are plotted in Figure 2-6, where any two adjacent ambiguous angular positions are separated by 2π phase difference. Additionally, note that all possible angular positions of a single target (independent of gain and thus SNR) are spread from horizon to horizon. In order to describe these different ambiguity regions, the term "ambiguity index" is

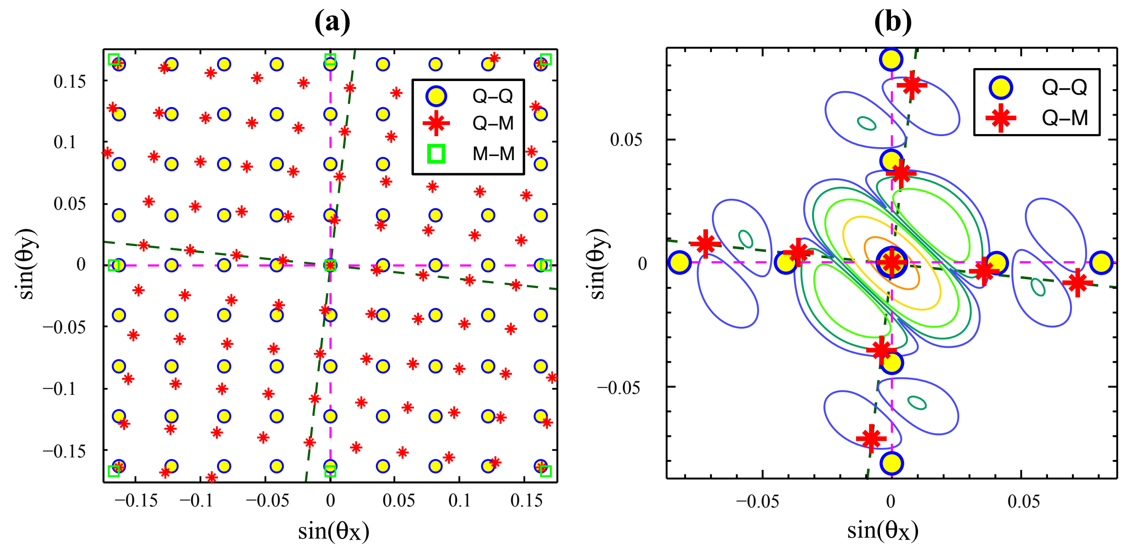

Figure 2-6. An illustration of ambiguity mapping. (a) Ambiguity mapping over $\pm 10°$, with angular ambiguous positions of Q-Q shown in yellow circles, Q-M in red stars, and M-M in green squares. The primary axes of Q-Q and M-M are shown in pink dashed lines. Primary axes for Q-M are shown as the dark green dashed line. Note that the ambiguity mapping can be extended to $\pm 90°$. (b) Ambiguity mapping of $\pm 5°$, with the Figure 2-5 transmit/receive radiation pattern plotted in the background. For simplicity, we only show the angular ambiguous positions along primary axes of Q-Q, where relatively stronger sidelobes are expected.

introduced based on the multiples of 2π introduced to the net antenna-to-antenna phase difference of interferometric result. The on-axis nearly-zenith region for JRO is designated as "Region 0". Index "0" also indicates that no extra phase is added to the interferometric result. "Region 1" has 2π added to interferometric phase difference while "Region 2" has $2\times2\pi$ added and so forth. The indexing extends equivalent interferometric pointing from horizon to horizon. Indexing can also be negative such that all four quadrants are considered.

The boundaries of each ambiguity region along one baseline is defined as:

$$\sin(\theta) \in \left[(2N-1)\left(\frac{\lambda}{2d}\right), (2N+1)\left(\frac{\lambda}{2d}\right)\right] \tag{2.4}$$

while the center of each ambiguity region is given by

$$\theta_N = \sin^{-1}\left(N\frac{\lambda}{d}\right)\ rad \tag{2.5}$$

where N is ambiguity index.

Different baselines d would yield different ambiguity region coverage, which leads to different off-zenith angles corresponding to the indexing numbers. In this paper, we use the Q-Q receiving pair as the indexing reference. Region 0 is zenith and Region 25 reaches below horizon. And the relationships between ambiguity indices and their corresponding off-zenith angles are listed in Table 2-4.

Using Q-Q as reference, we calculated the angular differences between it and the other two receiving configurations (M-M, Q-M) according to ambiguity mapping. In order to preserve linearity, we express the angular differences in the form of $\Delta\sin\theta$ instead of angle θ. The results are shown in Figure 2-7 where, due to symmetry, only a quarter of the sky is plotted.

Based on the net radiation pattern shown in Figure 2-4 and Figure 2-5, our focus is along one of the primary axes. This is where sidelobe contamination would most likely occur, as the sidelobe gain is highest there. Since the patterns along both axes are nearly the same (to within transmit pattern differences), we only show here the angular differences along x-axis in Figure 2-8.

According to the Figure 2-8 ambiguity mapping results, there are no locations where two angle-aliased targets overlap each other except at zenith. This demonstrates the validity of using multi-baseline interferometry to get an effective all-sky unambiguous region.

However, the angular differences illustrated in Figure 2-7 and Figure 2-8 are calculated without taking target signal-to-noise ratio (SNR) into consideration. In general, the observations are subject to SNR limitations and to various non-thermal interference sources as well as to systematic observation errors introduced by non-ideal array features that are inherent to any array radar observations. Thus the interferometrically-derived target angular position reflects a certain error that is highly dependent on the SNR of the given target. We will discuss this issue in detail in the following section when analyzing a representative high-altitude radar meteor (HARM) event.

Table 2-4. Q-Q ambiguity indices and their corresponding off-zenith angles

Ambiguity Index	1	2	3	4	5	6	7	8
Off-Zenith Angle	2.339°	4.682°	7.034°	9.397°	11.78°	14.18°	16.60°	19.06°
Ambiguity Index	9	10	11	12	13	14	15	16
Off-Zenith Angle	21.55°	24.09°	26.68°	29.33°	32.05°	34.85°	37.75°	40.77°
Ambiguity Index	17	18	19	20	21	22	23	24
Off-Zenith Angle	43.94°	47.28°	50.85°	54.72°	59.00°	63.89°	69.85°	78.40°

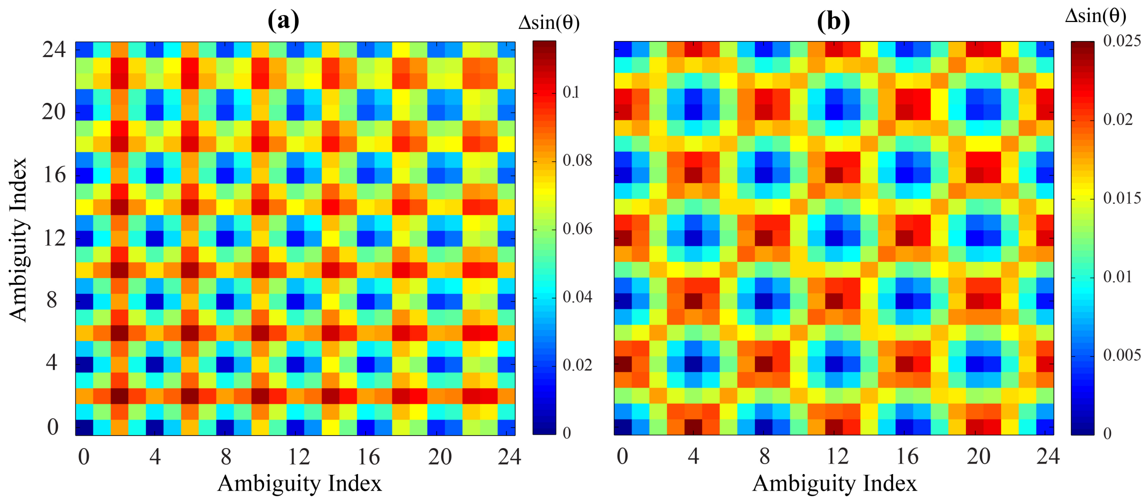

Figure 2-7. Angular differences from ambiguity mapping of a stationary point target from (a) Q-Q and M-M receiving configurations, (b) Q-Q and Q-M receiving configurations. The target is assumed to be overhead, and mapped all across the sky by adding multiples (ambiguity index) of 2π into the derived phase $\Delta\phi$ from the CCF (cross-correlation function). Note that the angular differences are shown in the form of $\Delta\sin\theta$ to preserve linearity. Due to symmetry, only a quarter of the sky is plotted here. The center of Region 0 is the on-axis pointing direction of the JRO array.

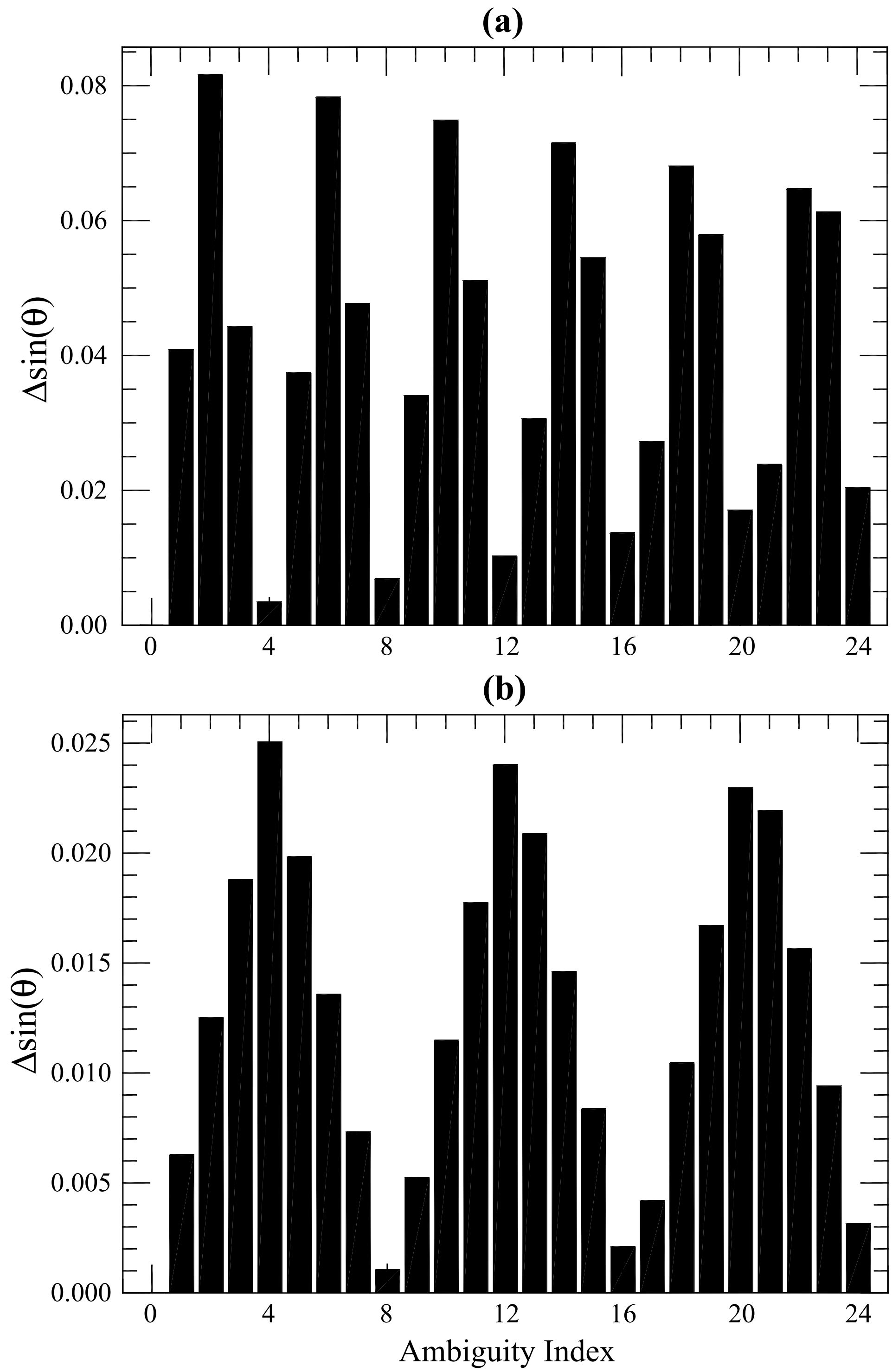

Figure 2-8. Angular differences from ambiguity mapping along one primary axis from (a) Q-Q and M-M receiving configurations, (b) Q-Q and Q-M receiving configurations. Note that the angular differences are shown in the form of $\Delta\sin\theta$ to preserve linearity. Note the differences in scales and periodicity.

2.4 Observational Results of HARM events

All three receiving configurations described above were calibrated separately based on the well-studied fact that the sufficiently averaged Equatorial Electrojet (EEJ) return is clustered at the radar **k⊥B** locus [*Kudeki and Farley*, 1989; *Woodman*, 1971] due to the aspect sensitivity of this scattering mode. This approach establishes the reference for our interferometric interpretations. Additionally, a radio beacon was used for monitoring any sudden phase changes of all of the receiving channels.

While ultimately relying on multi-baseline interferometry for our conclusions, we also employ the basic fact that using both the Q-Q and M-M configurations simultaneously produces concentric beams with different main-beam and sidelobe widths (similar to the UHF/VHF system at Arecibo [*Mathews*, 2004]). Thus, one easy and intuitive method to distinguish whether a target was from near overhead is to count how many sidelobe/null structures were observed with each receiving configuration, respectively, for any given event. In principle, for a given event the wider M-M receiving configuration displays fewer lobe/null structures than the narrower, but more sensitive, Q-Q counterpart. Further, the observed and modeled patterns only match over specific, identifiable regions of the sky.

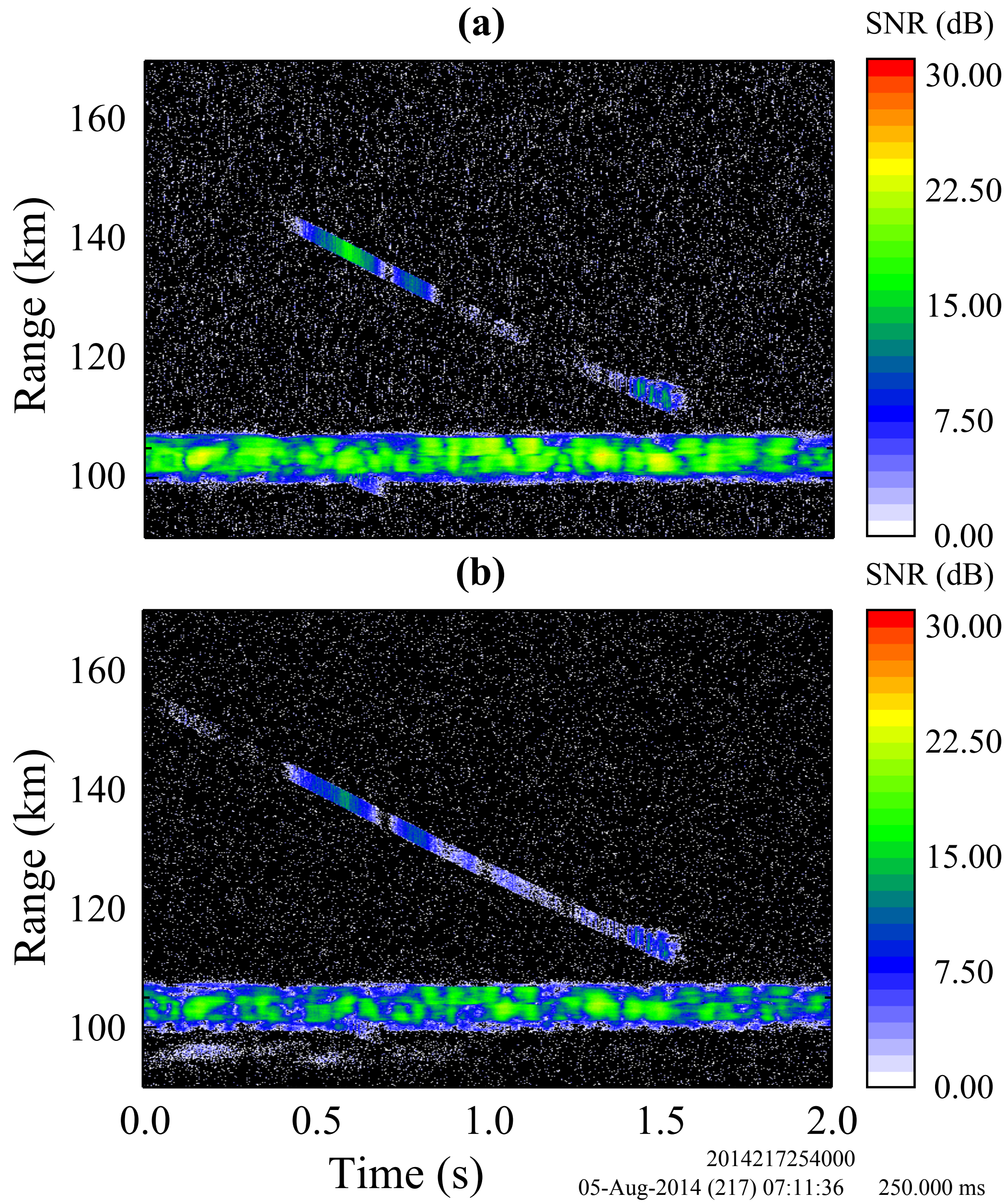

Figure 2-9. The Range-Time-Intensity (RTI) plots of a high-altitude radar meteor (HARM) event observed with (a) quarter-quarter (Q-Q) receiving configuration, and its counterpart (b) module-module (M-M) receiving configuration. Note that more lobe/null structures were observed in the panel (b) M-M receiving configuration the wider, but less sensitive, beam configuration. As discussed in the text, for this moderate-SNR event, this is evidence of overhead detection.

Figure 2-9 shows an example of a high-SNR high-altitude radar meteor (HARM) event with a Doppler speed of ~53.36 km/s approaching the radar. It has a beginning height of 152$\pm$0.15 km and ending height ~110$\pm$0.15 km with a weak terminal flare. Note that there are more lobe/null structures observed in panel (b) due to the wider beam width of M-M receiving configuration. However, the SNR in panel (a) is higher because of the greater main-beam sensitivity of Q-Q receiving configuration. Overall, this event is too weak for our multi-baseline interferometric analysis, as high SNR is required to minimize phase noise. The noise level for each receiving configuration is automatically determined using the method introduced by Hildebrand and Sekhon [1974]. This method makes use of the observed Doppler spectrum and physical properties of white noise. It does not involve knowledge of the noise level of the radar system and is suitable for automatic computation.

Figure 2-10 shows another, especially distinctive, HARM event. Note that the panel (a) narrow-beam head-echo trajectory is significantly shorter than the panel (b) wide-beam result. Also note that the terminal flare is only visible in panel (b) suggesting that the flare occurred just outside the narrower beam Q-Q beam even though this configuration has higher main-beam sensitivity than the M-M configuration.

In order to better interpret the Figure 2-10 HARM event, Figure 2-11 shows this event as observed with the wide-beam M-M configuration after statistical processing for removal of the EEJ return. This processing, which reveals the meteor event range-spread trail-echo, is based on the fact that the EEJ has a well-defined phase structure that is statistically distinct from the meteor trail-echo return. The EEJ “filter” identifies the mean and standard deviation of power, Doppler, and phase of EEJ at each range that are then removed thus separating the meteor event from EEJ. The details and applications of the EEJ filtering is discussed in Section 2.5.

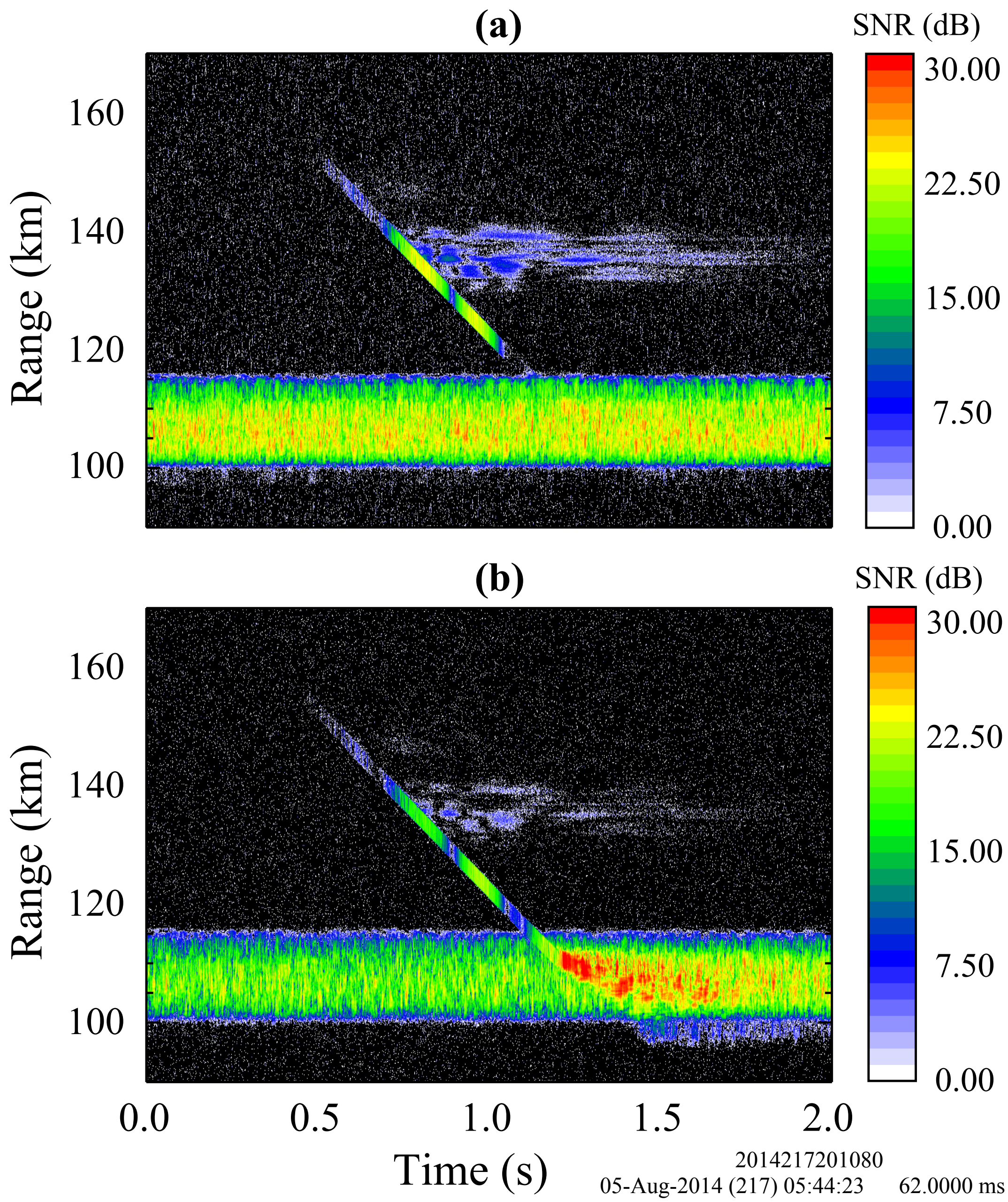

Figure 2-10. A high-SNR HARM event exhibiting both trail-echoes and terminal flares. Shown are the RTI plots from the (a) narrow-beam Q-Q receiving configuration, and (b) wide-beam M-M receiving configuration. Notice the terminal flare in (b) is in the traditional meteor zone, another convincing evidence of overhead detection. The radial speed of this meteor event is ~60.33 km/sec.

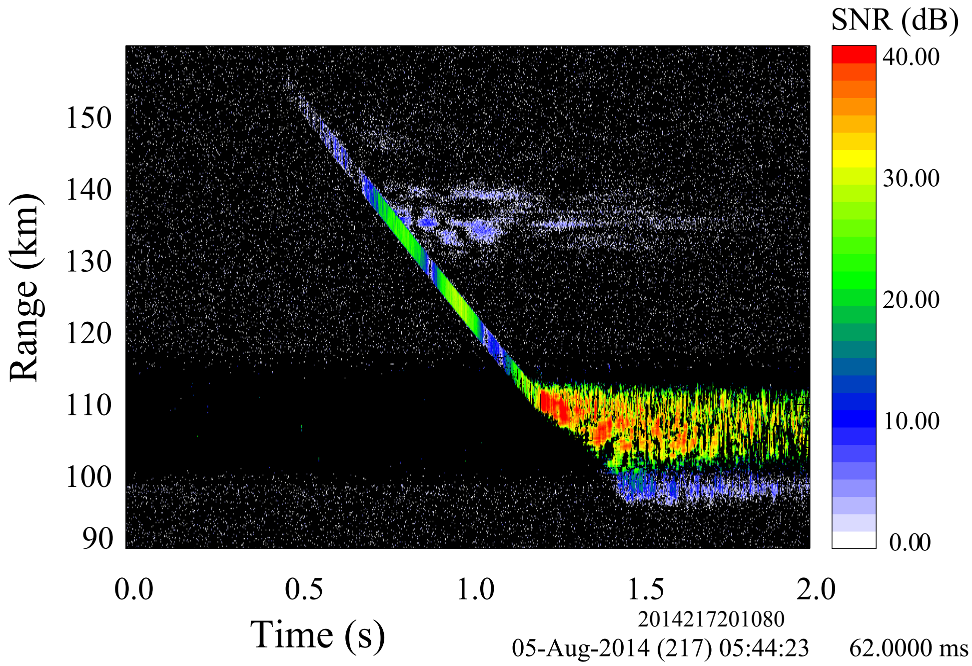

Figure 2-11. Figure 2-10 (b) HARM event, observed with M-M interferometric baselines, after statistical EEJ filtering. Note that the head-echo is not visible below ~110 km range.

The Figure 2-11 HARM event was detected at a beginning height of 153$\pm$0.15 km, and ended with terminal flares and RSTEs (range-spread trail-echoes) spreading down to 97$\pm$0.15 km. It has a radial speed of ~60.33 km/s towards the radar, and a radial deceleration of ~3.04 km/s^2. The terminal flaring takes place within the traditional meteor zone and exhibits features resembling those commonly observed at JRO. The fact that the associated terminal flaring ranges from 97 — 113 km and is near to but is separate from the EEJ region supports our contention that this HARM event occurred near zenith.

This event also produced high-altitude trail-echoes at ranges from 130 to 140 km. The interferometric results shown in Figure 2-12 indicate that they originate from the **k⊥B** region for the JRO radar. This further constrains the meteor trajectory to the vicinity of the JRO **k⊥B** region. Note from panel (c) that the RTI plot of trail echoes of this HARM event resembles features of previously introduced "dragon" events (Figure 9 in *Gao and Mathews* [2015a]). These echoes extend ~10km in range and exhibit very diffuse features. We now suspect, based on these results, that the events we named "Dragons" in *Gao and Mathews* [2015a] are most likely trail-echoes from HARM events for which the head-echoes were too weak to be observed.

We also analyzed the head-echo of the Figure 2-10 HARM event in the manner of *Gao and Mathews* [2015a] with the results shown in Figure 2-13. The SNR matching technique applied here [*Chau et al.*, 2008] gives excellent agreement between the measured SNR and the expected relative SNR (See Figure 2-13 panel (c)). This further suggests that the meteoroid radar meteor head-echo passed through the JRO main beam.

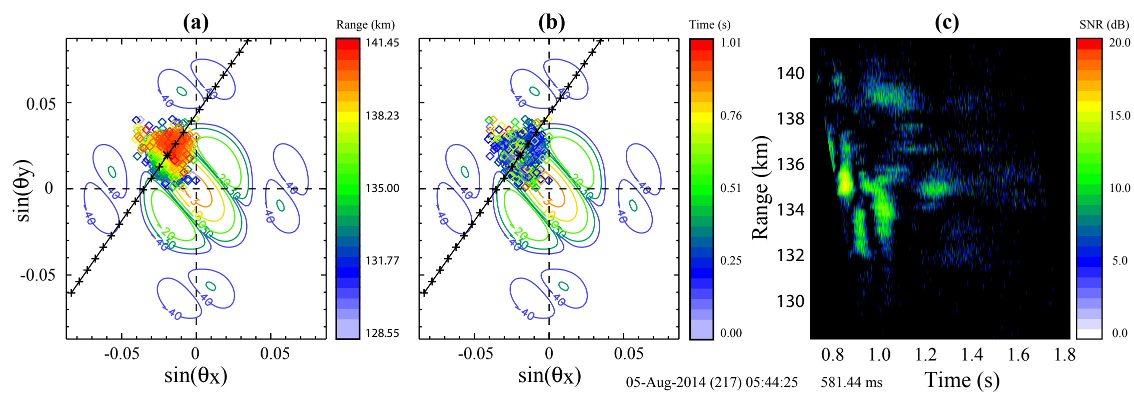

Figure 2-12. Details of the high-altitude trail-echoes associated with the HARM event shown in Figure 2-10. Shown are the interferometric results of the trail echoes as a function of (a) range and (b) time. The theoretical two-way radiation pattern (in dB) is also plotted in the background. (c) Detailed RTI plot of the trail echoes. Note that the trail-echo comes exclusively from the $\mathbf{k} \perp \mathbf{B}$ scattering region.

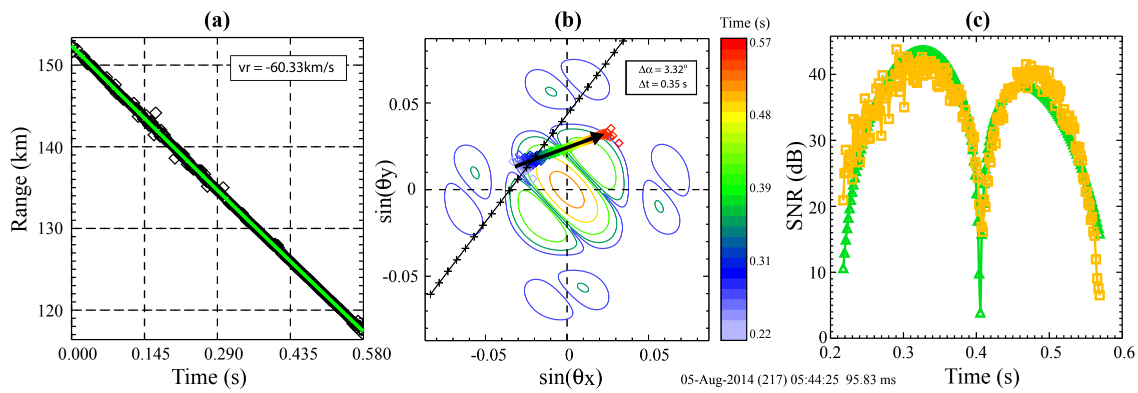

Figure 2-13. The head-echo characterization of the HARM event in Figure 2-10. (a) Range vs. time; (b) $\sin\theta_x$ vs. $\sin\theta_y$; (c) SNR vs. time. In panel (a), the fitted range vs. time trajectory is given in green. The fitted slope corresponds to a 60.33 km/s line-of-sight speed towards the radar. Panel (b) gives the unwrapped interferometric trajectory of the head echoes as a function of time. Only the two antenna-lobe structures with high SNR and seen by both receiving configurations are shown here. The phase-fitting trajectory is given as the thick black solid line. The thin solid line overlaid with plus signs indicates the radar **k⊥B** region at the altitude of 100 km at JRO. The theoretical radiation pattern (in dB) is also plotted in the background. In panel (c), the measured SNR versus time is plotted in yellow, while the expected relative SNR, based on the theoretical antenna pattern and angular positions from panel (b), is denoted in green.

We now demonstrate the utility of the new multi-baseline interferometric technique that, in comparison with that employed in *Gao and Mathews* [2015a] is no longer ambiguous. As shown in Figure 2-3 As shown in the Q-M receiving pairs B-F and E-A offer an extra independent set of angular positions of the meteor head-echo, which can be used to resolve the phase ambiguity issues intrinsic to Q-Q or M-M interferometry alone.

Figure 2-14 gives an illustration of how we removed phase ambiguity via comparison of the various receive configurations. In panel (f), the dark red arrow (Q_{ambi}) indicates where the meteor head echo trajectory was according to analysis of the Q-Q receiving pair results without further adjustment. The dark green arrow (N_{ambi}) shows the result using the newly-employed Q-M receiving pairs. The combination of these two receiving configurations, adjusted by the 2π ambiguity factor, indicates convergence only when the two results overlap each other yielding the unambiguous angular position. Since the M-M receiving pairs have the largest ambiguity square of the three, it is used as a reference to which direction de-aliasing the phases of the other two configurations should proceed. In this particular case, the trajectory was moved 2π in $+y$ direction for Q-Q receiving pairs, and 2π in $+y'$ direction for Q-M receiving pairs. Then the results from three independent measurements are in perfect agreement, as shown in Figure 2-14 panel (f), in which ‘Q’ is for Q-Q, ‘N’ for Q-M, ‘M’ for M-M receiving pairs, respectively. This new interferometric technique, outlined in Figure 2-6 to Figure 2-8, thus gives us the true, unambiguous (labeled “FINAL”) angular position of this particular, high-SNR meteor head-echo event. It is found to be near-zenith over its entire high-SNR trajectory.

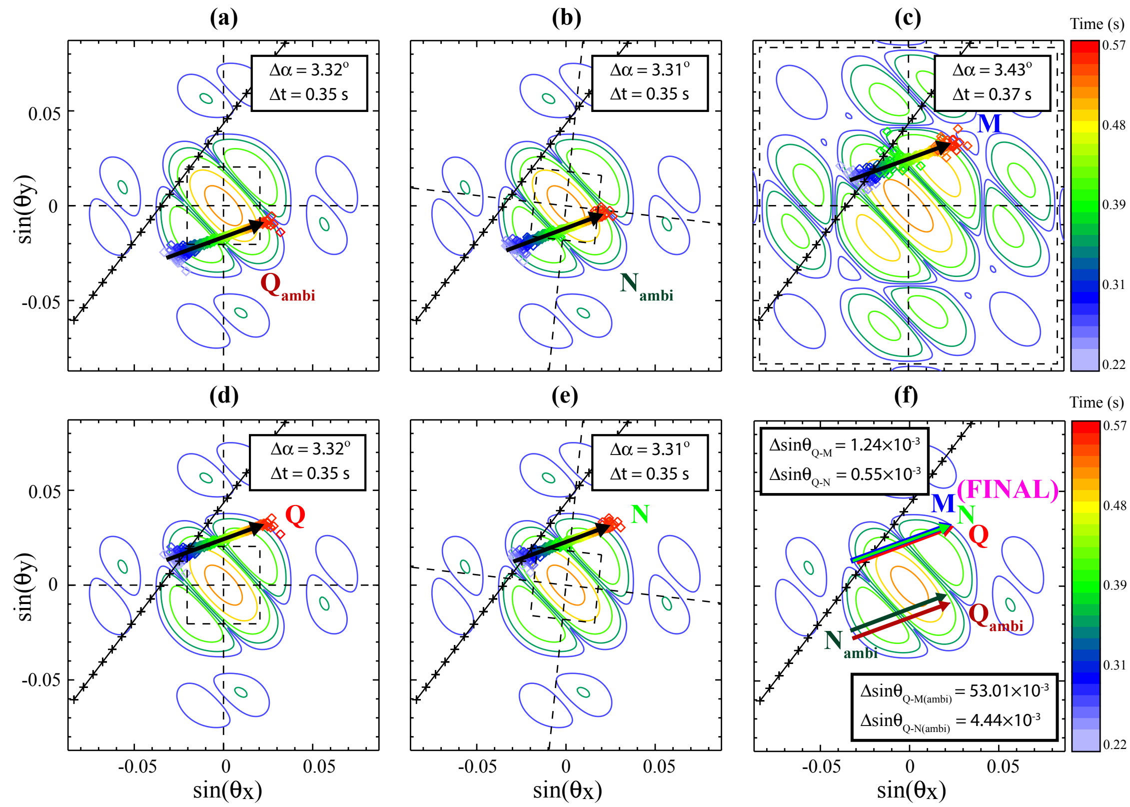

Figure 2-14. Interferometric results for the HARM head-echo event shown in Figure 2-10. Individual mode angular results derived from the (a) Q-Q receiving pairs, denoted as Q_{ambi}, the (b) Q-M receiving pairs, denoted as N_{ambi}, and (c) M-M receiving pairs, denoted as M. Note that this event lies totally within the M-M ambiguity region. The dashed squares indicate the ambiguous square regions for each receiving pair while the orthogonal dashed lines indicate the directions of the primary axes in each configuration. The final angular results after phase de-aliasing from the (d) Q-Q receiving pairs, denoted as Q, and the (e) Q-M receiving pairs, denoted as N. (f) Using the Q-Q receiving pairs as reference, the angular differences between different receiving configurations before and after phase de-aliasing are given. The goal here is to minimize both angular differences to the noise level. The final "converged" trajectory is labeled FINAL, which is the overlapping angular positions indicated by M, N, and Q. Note that the angular positions are shown as sinθ to preserve linearity.

The angular errors of Q-Q, Q-M, and M-M receiving configuration for this specific HARM event are 1.28×10^{-3}, 1.15×10^{-3}, 2.76×10^{-3} (listed in Table 2-5 in $\sin\theta$), respectively. These are the root mean square (RMS) errors derived from angular fitting in interferometry. But according to Figure 2-7 panel (b), the desired angular difference between Q-Q and Q-M in ambiguity region (8, 0) is $\Delta\sin\theta = 1.0\times10^{-3}$. The angular error ($1.28\times10^{-3}$ and 1.15×10^{-3}) slightly exceeds the ideal angular difference (1.0×10^{-3}), which limits the usefulness of this combination in ambiguity region (8, 0). However, fortunately, the ideal angular difference between Q-Q and M-M in ambiguity region (8, 0) is $\Delta\sin\theta = 6.8\times10^{-3}$, which is well in excess of the observed error level (2.76×10^{-3}). Therefore, we conclude that the location of this specific HARM event has been unambiguously identified.

As discussed in previous section, the precision of this technique is highly dependent on the SNR of the detected targets. For example, we chose to use only the two antenna-lobe structures with high SNR in Figure 2-10 for interferometric analysis. The event signal components from other low-SNR lobes are too noisy to derive interferometric results as phase de-aliasing is impossible.

For completeness, we have also analyzed the Figure 2-10 HARM head-echoes assuming they were seen in the antenna sidelobes. From the discussion regarding Figure 2-5, it is reasonable to assume that, if this HARM event were indeed observed in one of the more distant (far from zenith) sidelobes, it would be from one along the primary axes. Taking the result of ambiguity mapping into consideration, we assume the meteor head-echo is actually located in Figure 2-7 ambiguity region (8, 0) — ~19° off zenith—along the x-axis.

Table 2-5. RMS angular errors of the representative HARM event for each receiving configuration.

Receiving Configurations	Root Mean Square Angular Error (sin θ)
Quarter-Quarter (Q-Q)	1.28×10^{-3}
Quarter-Module (Q-M)	1.15×10^{-3}
Module-Module (M-M)	2.76×10^{-3}

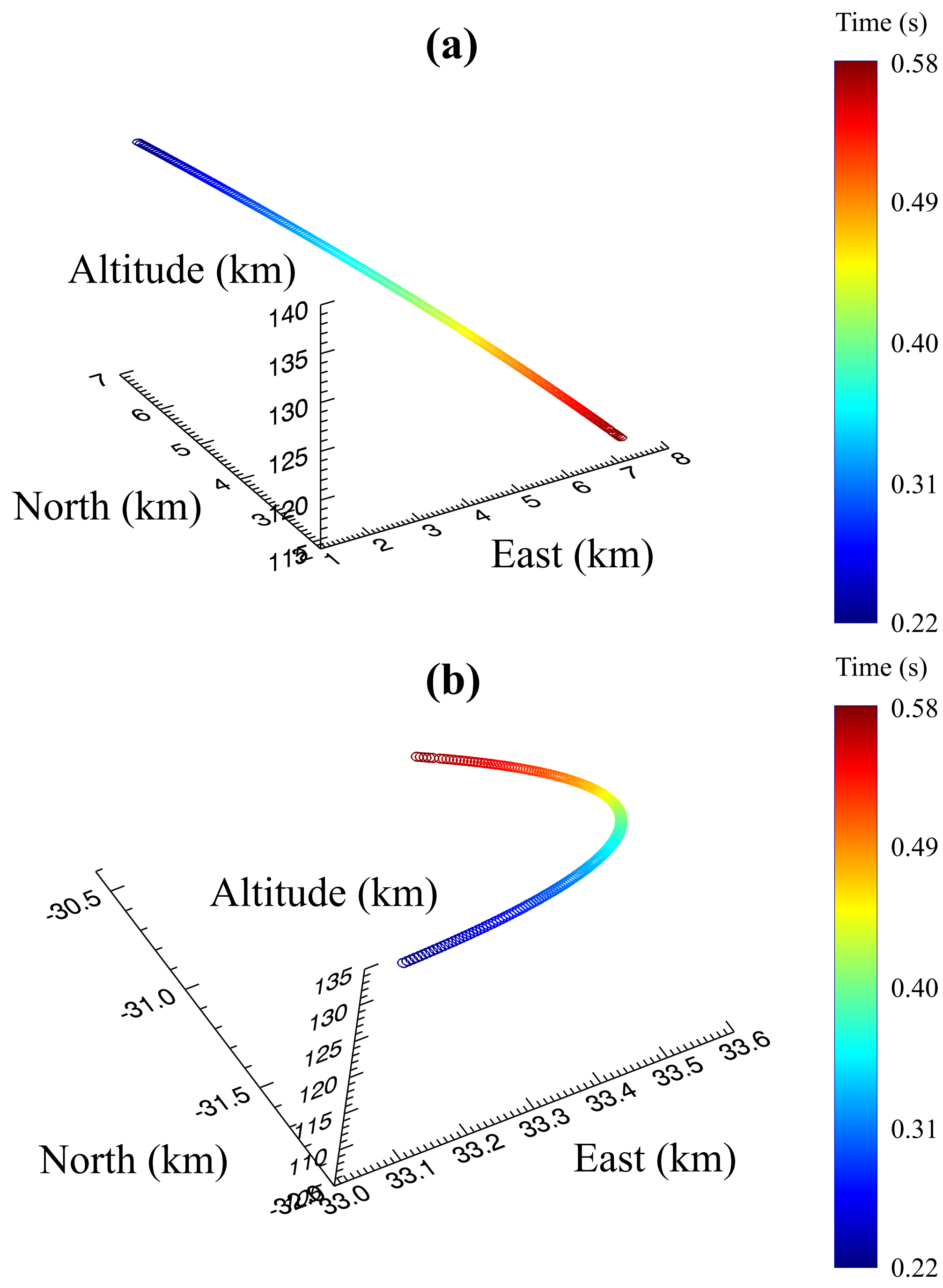

Figure 2-15. The 3D trajectory of the HARM head-echo in Figure 2-10 (a) at zenith and (b) when moved to ambiguity region (8, 0), about 19° off zenith. Note the resolvable—given sufficient SNR—significant trajectory curvature implied by the sidelobe detection interpretation.

Range and angular position information were used to reconstruct a 3D trajectory of the meteor, shown in Figure 2-15. It is interesting that the trajectory, after being moved ~19° off zenith along the x-axis, ended with a significant curvature that is physically unrealistic for a meteoroid. Additionally, the beginning altitude only drops from 153 km to 144 km and it still qualifies as a HARM event. Note that all of the analysis shown above used only the two lobes with the highest SNR (refer to Figure 2-10) nonetheless implying that the intrinsic radar scattering cross-section of the meteor would have to be ~50 dBi larger than the same event in the main-lobe region.

Furthermore, the **k⊥B**-clustered high-altitude trail-echo further constrains the trajectory to the vicinity of **k⊥B** region of JRO. The two-way sidelobe level along **k⊥B** region at ~11° off zenith is theoretically ~80 dBi lower than the peak—in practice this figure is smaller (larger gain) but still very significant. That is, head-echoes visible in the distant sidelobes would indicate a very major event as we explore next, since sensitivity drops so quickly when moving away from zenith along the **k⊥B** line (refer to Figure 2-4 and Figure 2-5)

The radar equation is given as

$$SNR = \frac{P_R}{P_N} = \frac{\dfrac{P_T G_T G_R \lambda^2 \sigma}{(4\pi)^3 R^4}}{k(T_0 + T_s)B} \tag{2.6}$$

where P_R is the received power, P_N is the noise power. $P_T = 1$ MW is the transmitted power, $G_T = 41$ dBi is the transmission gain, $G_R = 38$ dBi is the reception gain, $\lambda = 6$ m is the operating wavelength, σ is the radar cross section (RCS) which we want to evaluate, $R = 135$ km is the range of the meteor head echo where we have the highest $SNR = 25$ dBi, $k = 1.38\times10^{-23}$ J/K is Boltzmann constant, $B = 1$ MHz is the bandwidth of the receivers, $T_0 = 290$ K is noise reference temperature, which is customarily taken to be room temperature, $T_S = 10000$ K is the sky temperature.

Using radar equation (2.6), the RCS of this HARM event is estimated to be 1.035×10^{-2} m^2 if detected in the main beam, while it is of order $10^{3\sim6}$ m^2 if detected with one of the sidelobes at ~11° off zenith along $\mathbf{k}\perp\mathbf{B}$ region (assuming the sensitivity is 50~80 dBi lower). Taking both the sidelobe level and $\mathbf{k}\perp\mathbf{B}$ constraints into consideration, it is highly unlikely that this event could be picked up in any sidelobe.

We observed a total number of 54 HARM events during this meteor observation experiment. All of these HARM events took place at around local sunrise when radial speeds tend to be the largest. Their apparent beginning and ending heights, along with times of occurrence, are shown in Figure 2-16.

Note that not all the head echoes listed here are analyzable. Some head echoes are so weak compared with their associated trail echoes that they could not be isolated or analyzed. Thus we cannot rule out the possibility of sidelobe contamination for all 54 events. However, HARM events with SNRs higher than 30 dB do show convincing evidence of overhead detections by applying the multi-baseline interferometric techniques.

Out of these 54 HARM events, the head echoes of 52 events have high enough SNRs and could be isolated from their associated trail echoes. The details of their occurrence times, Doppler speeds, 3-D absolute speeds, and highest SNRs are summarized in Table 2-6. The average Doppler (line-of-sight) speed is 48.69 km/s with a minimum of 15.65 km/s (Event # 2014217281052) and a maximum of 64.69 km/s (Event # 2014217257065). The average absolute speed, derived from meteors' 3-D position information, is 61.75 km/s with a minimum of 41.40 km/s (Event # 2014217276064) and a maximum of 71.43 km/s (Event # 2014217254000).

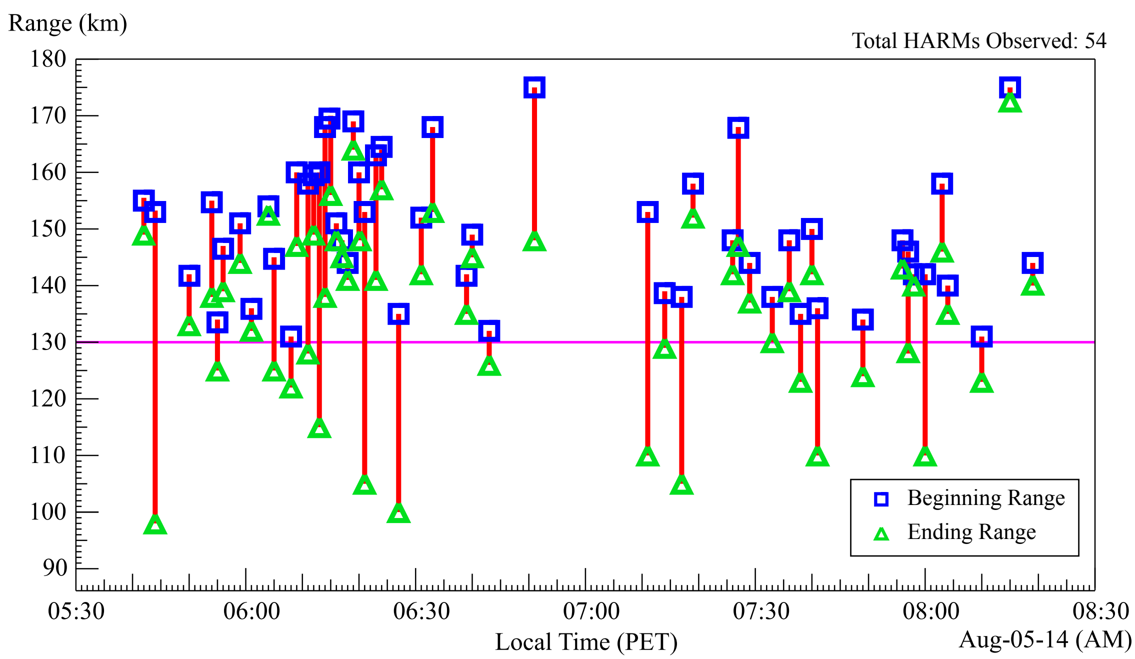

Figure 2-16. Statistics of HARM events in this dataset with apparent beginning ranges higher than 130 km.

Table 2-6. High-altitude radar meteor head echoes

Event Number	Time	Doppler Speed (km/s)	Absolute Speed (km/s)	Highest SNR (dB)
2014217200030	05:41:53	57.07	61.34	20
2014217201080	05:44:24	60.33	63.54	43
2014217205051	05:50:35	52.50	62.34	25
2014217207056	05:54:01	62.46	69.26	20
2014217207060	05:54:05	34.96	46.68	22
2014217208096	05:56:21	61.62	69.62	18
2014217210028	05:58:33	51.45	52.85	15
2014217211079	06:01:04	43.22	57.19	20
2014217216016	06:08:22	51.28	59.31	25
2014217216078	06:09:25	52.66	60.37	25
2014217217087	06:11:14	62.39	64.56	20
2014217217092	06:11:20	61.75	69.73	15
2014217218067	06:12:35	63.82	67.88	32
2014217219048	06:13:56	57.32	58.16	12
2014217220012	06:15:00	43.96	66.47	15
2014217220086	06:16:14	49.93	60.08	15
2014217222017	06:18:26	48.23	69.06	18
2014217222089	06:19:37	64.04	67.98	15
2014217220093	06:19:42	45.26	68.22	15
2014217230012	06:20:01	58.98	59.39	25
2014217230098	06:21:27	58.67	59.47	30
2014217225031	06:23:40	60.42	63.39	15
2014217225065	06:24:14	60.46	62.32	14
2014217227058	06:27:27	61.47	65.54	20
2014217229071	06:31:02	53.97	55.56	15
2014217230074	06:32:44	60.11	66.20	16

Event Number	Time	Doppler Speed (km/s)	Absolute Speed (km/s)	Highest SNR (dB)
2014217235013	06:40:05	57.31	60.31	15
2014217235023	06:40:15	24.24	59.59	28
2014217237015	06:43:27	58.45	61.69	15
2014217241087	06:51:20	61.11	68.21	15
2014217254000	07:11:36	58.33	71.43	31
2014217255034	07:13:50	56.13	64.07	20
2014217257065	07:17:42	64.49	67.02	23
2014217258059	07:19:16	42.73	70.11	25
2014217262051	07:25:50	42.35	58.34	18
2014217263005	07:28:43	37.03	69.30	21
2014217264029	07:28:47	19.79	58.70	20
2014217266063	07:32:43	32.67	62.60	43
2014217268036	07:35:36	51.04	68.17	25
2014217269082	07:38:02	37.61	45.99	40
2014217271024	07:40:25	57.45	66.58	25
2014217271026	07:40:26	53.02	57.29	45
2014217276064	07:49:26	39.78	41.40	15
2014217280043	07:55:46	47.08	56.20	40
2014217280097	07:58:40	51.00	65.01	32
2014217281052	07:57:36	15.65	62.35	20
2014217283035	08:00:39	55.14	58.33	22
2014217284086	08:03:10	23.80	56.64	25
2014217285019	08:03:43	39.66	64.67	35
2014217288078	08:09:43	19.80	56.47	21
2014217291091	08:14:56	16.27	60.09	23
2014217294040	08:19:06	31.51	54.15	26

2.5 Statistical EEJ Filtering

Plasma concentration irregularities in the ionosphere are generally highly elongated along the geomagnetic field [*Farley and Hysell*, 1996]. This is particularly true for the density waves generated by plasma instabilities at equatorial latitudes, such as, Equatorial Electrojet (EEJ). This anisotropy is known as “aspect sensitivity” and has been studied for decades. Radar backscatter from such irregularities, e.g. EEJ, is highly aspect sensitive [*Kudeki and Farley*, 1989]. EEJ echoes are the strongest when the radar is pointed nearly perpendicular to the magnetic field, which is commonly referred to as the $\mathbf{k}\perp\mathbf{B}$ region. This characteristic of EEJ could be taken advantage of to serve as a refernce phase of the JRO interterferometric baselines, thus to calibrate the JRO array [*Chau et al.*, 2008]. However, EEJ echoes also contaminated meteor return signals, due to its occurrence altitudes (~100-120km) lie within the traditional meteor zone (70-120 km above Earth surface) where most radar meteors are observed. Therefore, a filter capabale of separating meteor return signals from EEJ echoes is in need to exam the hidden features of meteors contaminated by the strong night-time EEJ echoes over JRO.

At the altitudes where EEJ occurs, the received radar signal is mainly comprised of three parts, meteor returns, EEJ echeos, and noise (including background noise and system noise).

$$V_R = V_{Meteor} + V_{EEJ} + V_{Noise} = A_M e^{j\phi_M} + A_{EEJ} e^{j\phi_{EEJ}} + A_N e^{j\phi_N} \qquad (2.7)$$

where V_R is the complex voltage of the received signal. V_{Meteor}, V_{EEJ} and V_{Noise} represent the complex voltages of meteor returns, EEJ echoes, and noise, respectively. A_M and ϕ_M are the amplitude and phase of the complex voltage V_{Meteor}, A_{EEJ} and ϕ_{EEJ} are the amplitude and phase of the complex voltage V_{EEJ}, A_N and ϕ_N are the amplitude and phase of the complex voltage V_N.

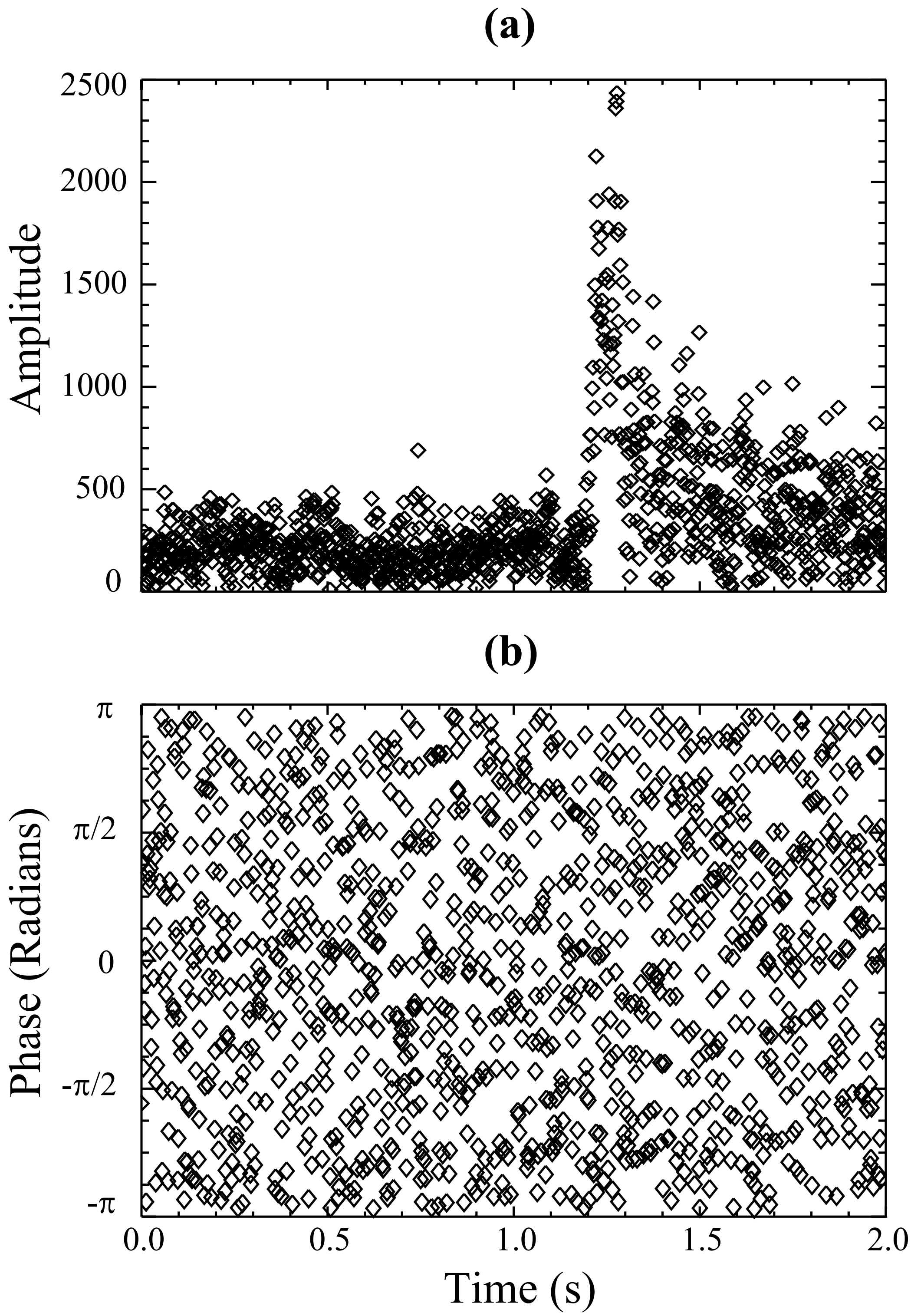

Figure 2-17. (a) Amplitude in arbitrary unit, and (b) phase of raw voltage at 110 km in Channel D.

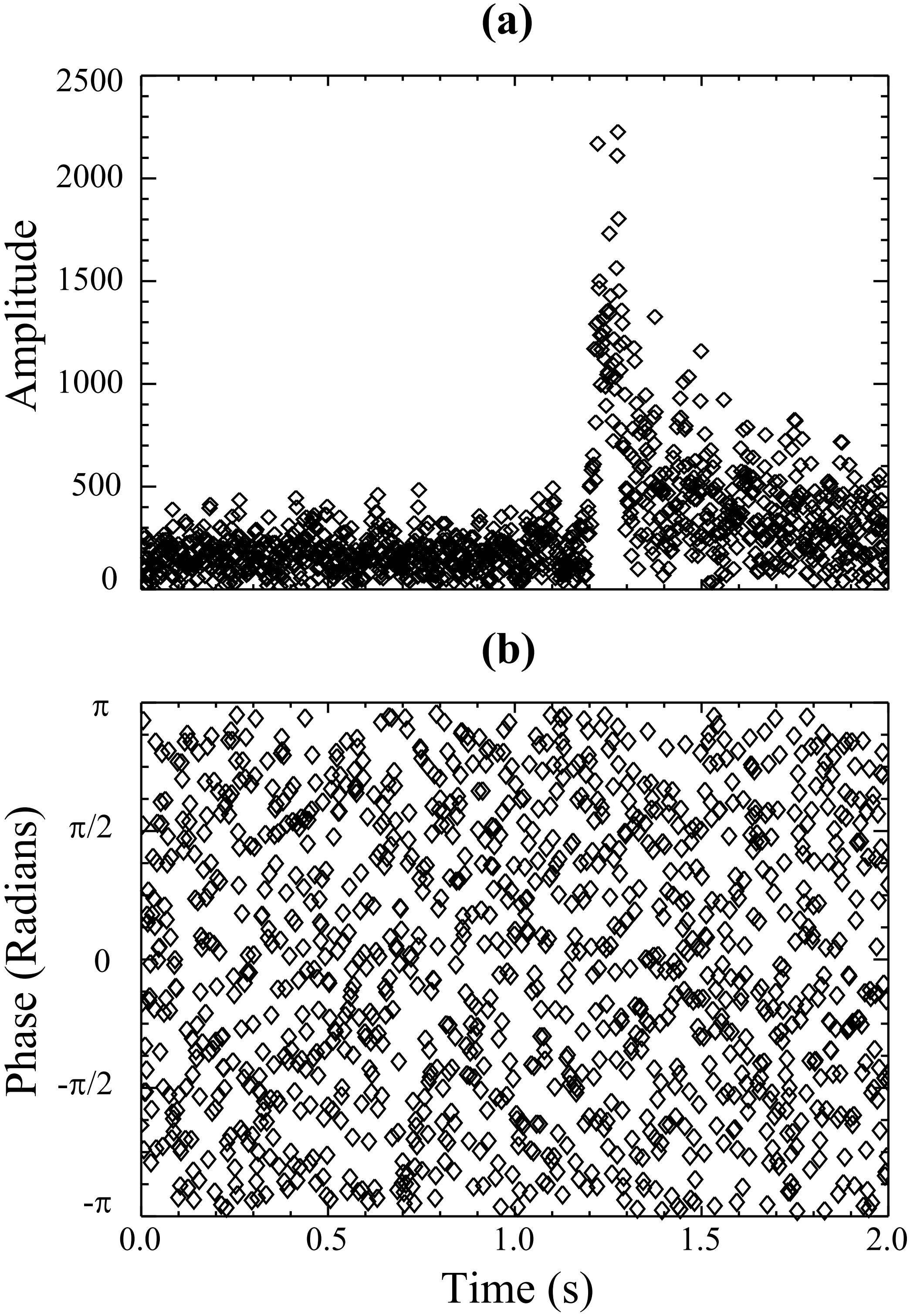

Figure 2-18. (a) Amplitude in arbitrary unit, and (b) phase of raw voltage at 110 km in Channel E.

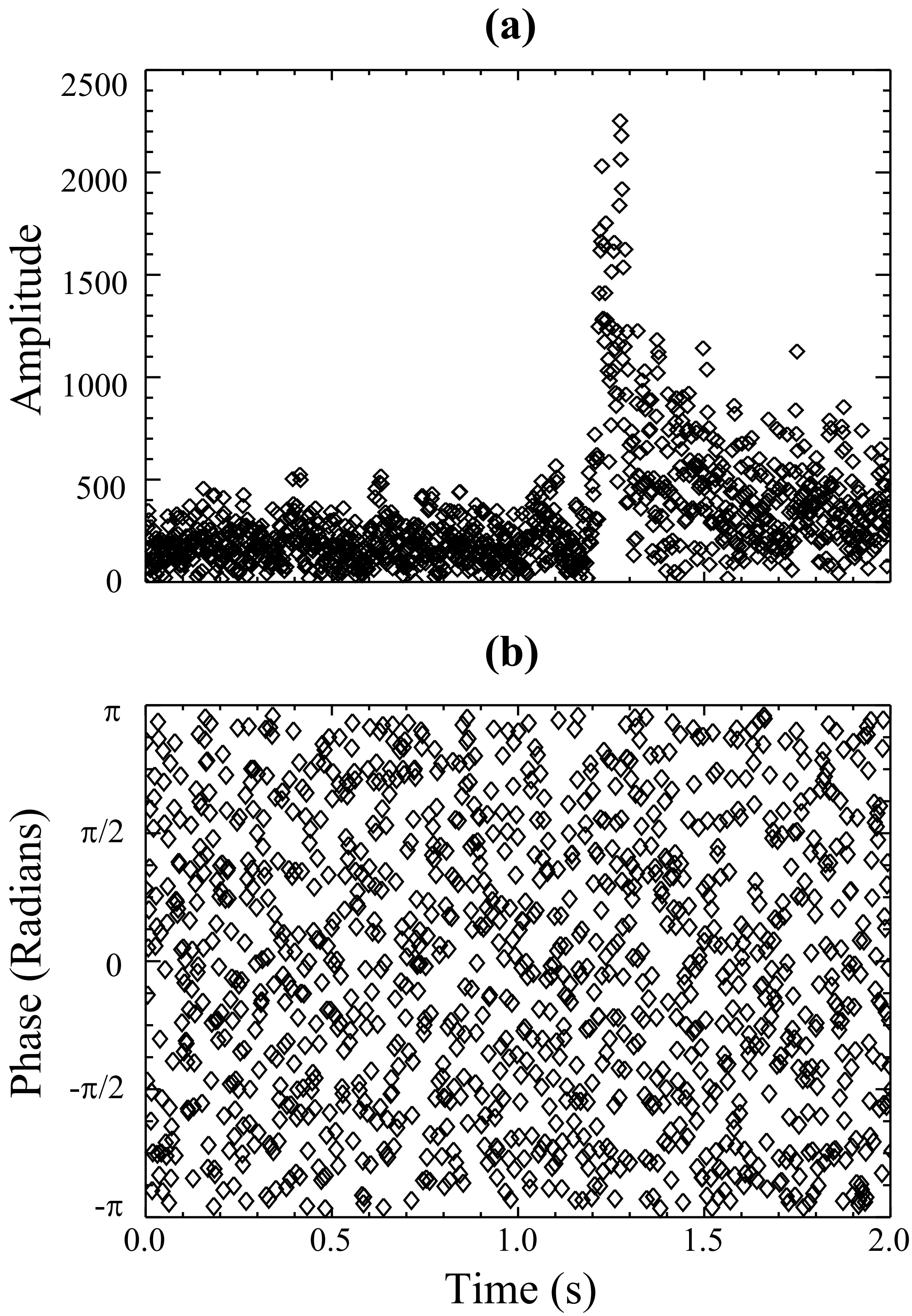

Figure 2-19. (a) Amplitude in arbitrary unit, and (b) phase of raw voltage at 110 km in Channel F.

We know that the sufficiently averaged Equatorial Electrojet (EEJ) return is clustered at the radar **k⊥B** locus [*Kudeki and Farley*, 1989; *Woodman*, 1971]. If this characteristic still holds true without time averaging, EEJ echoes V_{EEJ} can be easily subtracted from the received signal V_R. The complex voltages of three module-receiving channels, D, E, and F, are plotted in Figure 2-17, Figure 2-18 and Figure 2-19, respectively. The chosen altitude is 110 km in Figure 2-10 (b) where the well-developed EEJ layer is interrupted by an HARM event. We can see from the phase plots of all three channels that the behavior of the phase of the received signal resembles random noise. Therefore, it is not possible to simply subtract EEJ echoes V_{EEJ} from the received signal V_R, since V_{EEJ} does not have a valid instantaneous mean value to represent its time-averaged characteristics.

What we propose here is to use the statistical characteristics of EEJ in its power, Doppler, and interferometric domain to separate EEJ from meteors. The fundamental approach is the same as choosing a threshold to suppress noise, that is, treating EEJ echoes as noise. However, unlike random noise, most of the time, EEJ echoes have distinguishable features in Doppler as well as in interferometric results. These features can be used to further separate meteors from EEJ, which usually leads to more satisfactory results.

The statistical EEJ filtering investigates the characteristics of EEJ echoes in four independent domains, as plotted in Figure 2-20, (a) power, (b) Doppler, (c) interferometric baseline EF, and (d) interferometric baseline DE. Note in Figure 2-20 Panel (a) that power domain is the least distinguishable in terms of separating meteors from EEJ echoes, as the return signals of both meteors and EEJ coherently add up across different channels. Nevertheless, the power domain offers some information to calculate the statistical mean value and standard deviation of the power of EEJ echoes. Also note in Figure 2-20 Panel (b) and (c) that the features of EEJ echoes are very distinguishable from meteor head and trail echoes in Doppler and interferometric baseline EF.

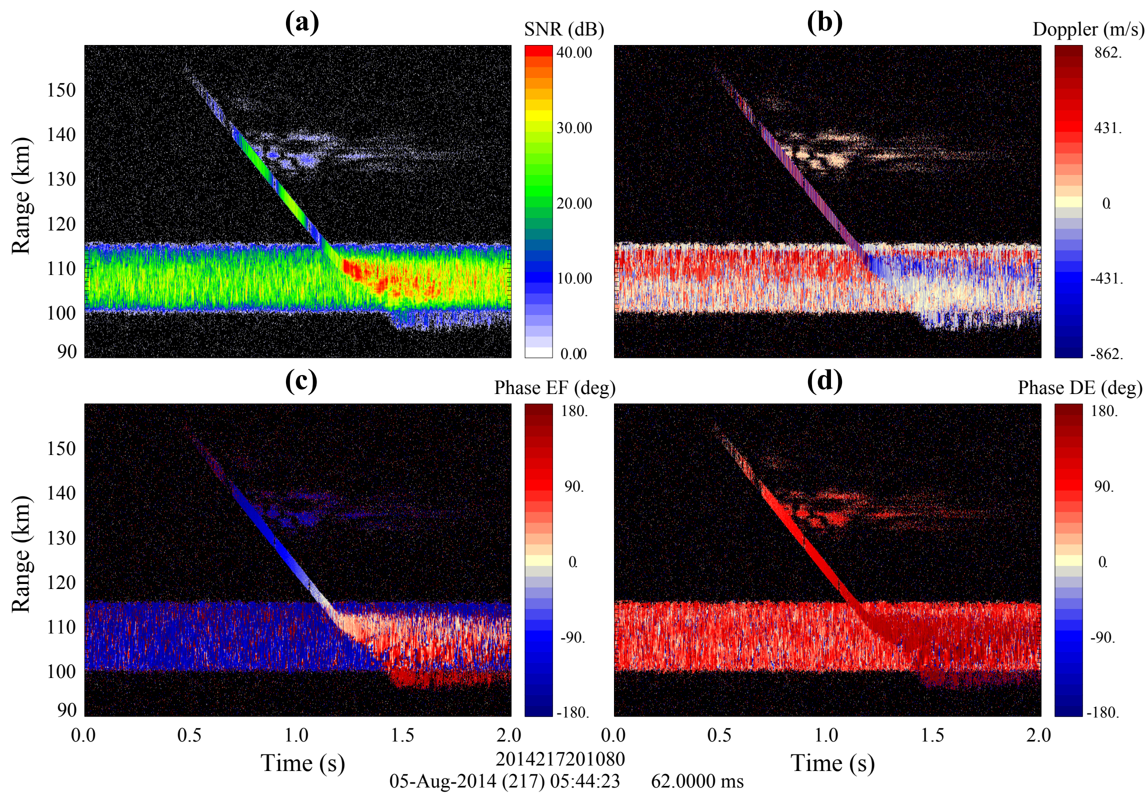

Figure 2-20. Figure 2-10 (b) HARM event before statistical EEJ filtering. (a) The Range-Time-Intensity (RTI) plot. (b) Doppler speeds (ambiguous) from pulse to pulse. (c) Phase difference (ambiguous) between module receivers E and F. (d) Phase difference (ambiguous) between module receivers D and E. “2014217201080” is the event number in the format of Year+DOY(Day of Year)+File Number+Block Number.

The detailed flow chart of this statistical EEJ filtering is shown in Figure 2-21. First of all, some well-developed EEJ echoes close in time to being interrupted by meteor events, but still free of meteors, are chosen as reference EEJ. Through averaging over time, the statistical characteristics of reference EEJ are calculated, such as, mean power μ_{P_j} and standard power deviation σ_{P_j}, mean Doppler μ_{D_j} and standard Doppler deviation σ_{D_j}, mean phase difference $\mu_{\phi_{j,EF}}$, $\mu_{\phi_{j,DE}}$, and standard phase difference deviation $\sigma_{\phi_{j,EF}}$, $\sigma_{\phi_{j,EF}}$, according to interferometric baselines EF and DE respectively. *j* denotes the height index in all these notations.

From time i when meteor occurs, the difference between the total power $P_{T_{(i,j)}}$ and the mean EEJ power μ_{P_j} is calculated. If the absolute difference $\Delta P_{(i,j)} = \left|P_{T_{(i,j)}} - \mu_{P_j}\right|$ is no greater than the standard power deviation σ_{P_j}, data point (*i, j*) is treated as noise and discarded. If $\Delta P_{(i,j)} > \sigma_{P_j}$ holds true, the power value of data point (*i, j*) is updated to $P_{T_{(i,j)}} - \mu_{P_j}$. In essence, EEJ echoes are treated as noise, and $\mu_{P_j} + \sigma_{P_j}$ is selected as noise threshold.

A very similar process is employed to filter out EEJ echoes in Doppler domain. However, the difference and the challenge, compared with power domain, are to determine the resultant Doppler of meteor returns. At the time of reception, the phases of meteor returns and EEJ echoes are coupled together. Therefore the received complex voltage at time *t* is

$$V_t = V_{Meteor} + V_{EEJ} = A_M e^{j\omega_M t} + A_{EEJ} e^{j\omega_{EEJ} t} \tag{2.8}$$

where t denotes a random time when the return signal is recorded, ω_M and ω_{EEJ} denote the angular frequency of meteor returns and EEJ echoes, respectively.

After time interval τ, which is the time duration of one IPP, the next received complex voltage of the same targets at time $t + \tau$ is

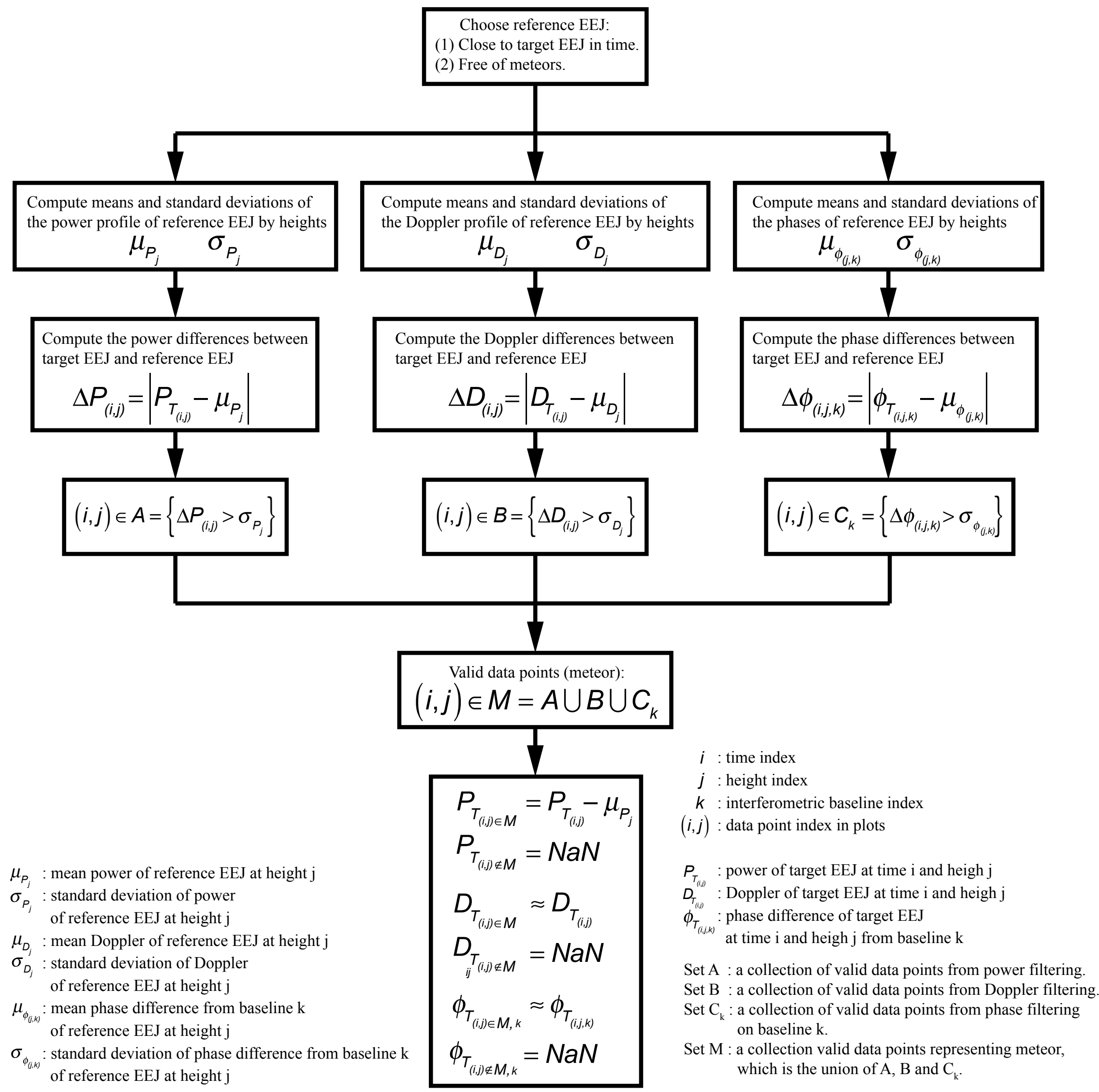

Figure 2-21. Detailed flow chart of statistical EEJ filtering.

$$V_{t+T} = V_{Meteor} + V_{EEJ} = A_M e^{j\omega_M(t+\tau)} + A_{EEJ} e^{j\omega_{EEJ}(t+\tau)} \tag{2.9}$$

Auto-correlating these two complex voltages gives

$$V_t * V_{t+T}{}^* = \left(A_M e^{j\omega_M t} + A_{EEJ} e^{j\omega_{EEJ} t}\right) * \left(A_M e^{-j\omega_M(t+\tau)} + A_{EEJ} e^{-j\omega_{EEJ}(t+\tau)}\right)$$

$$= A_M{}^2 e^{-j\omega_M \tau} + A_{EEJ}{}^2 e^{-j\omega_{EEJ}\tau} \tag{2.10}$$

$$+ A_M A_{EEJ} e^{j(\omega_M t - \omega_{EEJ}(t+\tau))} + A_{EEJ} A_M e^{j(\omega_{EEJ} t - \omega_M(t+\tau))}$$

The first two terms are related to the Doppler speeds of the meteor returns and EEJ echoes from IPP to IPP, respectively. The last two terms are unknown since they require knowledge of the instantaneous Doppler speeds of EEJ echoes at any given time. Consequently, we simply keep the Doppler values unchanged for data points (*i, j*) if $\Delta D_{(i,j)} > \sigma_{D_j}$. Obviously, the higher the meteor-to-EEJ power ratio, the more accurate this approximation is.

The same procedures are applied to get the phase differences from interferometric baselines EF and DE. And the result after applying this statistical EEJ filtering is shown in Figure 2-22.

Upon careful examination of the results shown in Figure 2-22, we notice that the phase differences of meteor returns and EEJ echoes according to interferometric baseline EF are significantly different. It means the meteor and the EEJ are located at two distinguishable angular positions over the JRO sky. We utilized this information to further clean up the EEJ echoes and yielded the results shown in Figure 2-23.

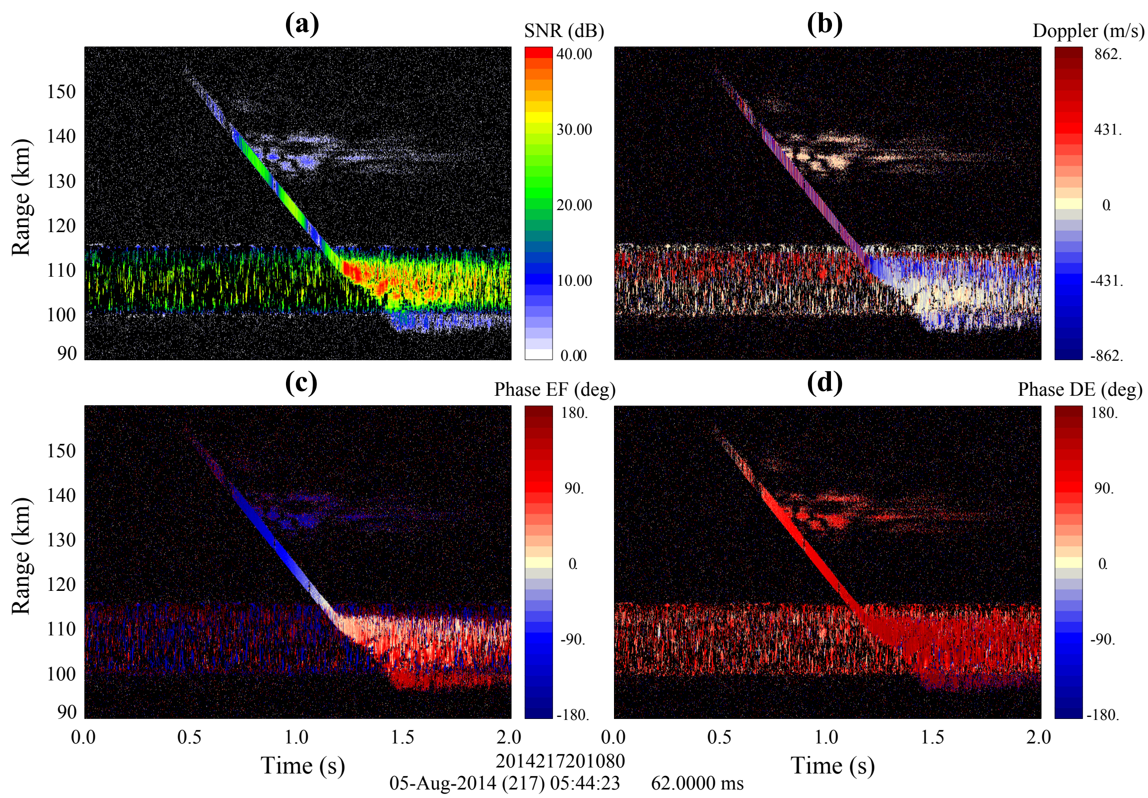

Figure 2-22. Figure 2-10 (b) HARM event after statistical EEJ filtering. (a) The Range-Time-Intensity (RTI) plot. (b) Doppler speeds (ambiguous) from pulse to pulse. (c) Phase difference (ambiguous) between module receivers E and F. (d) Phase difference (ambiguous) between module receivers D and E.

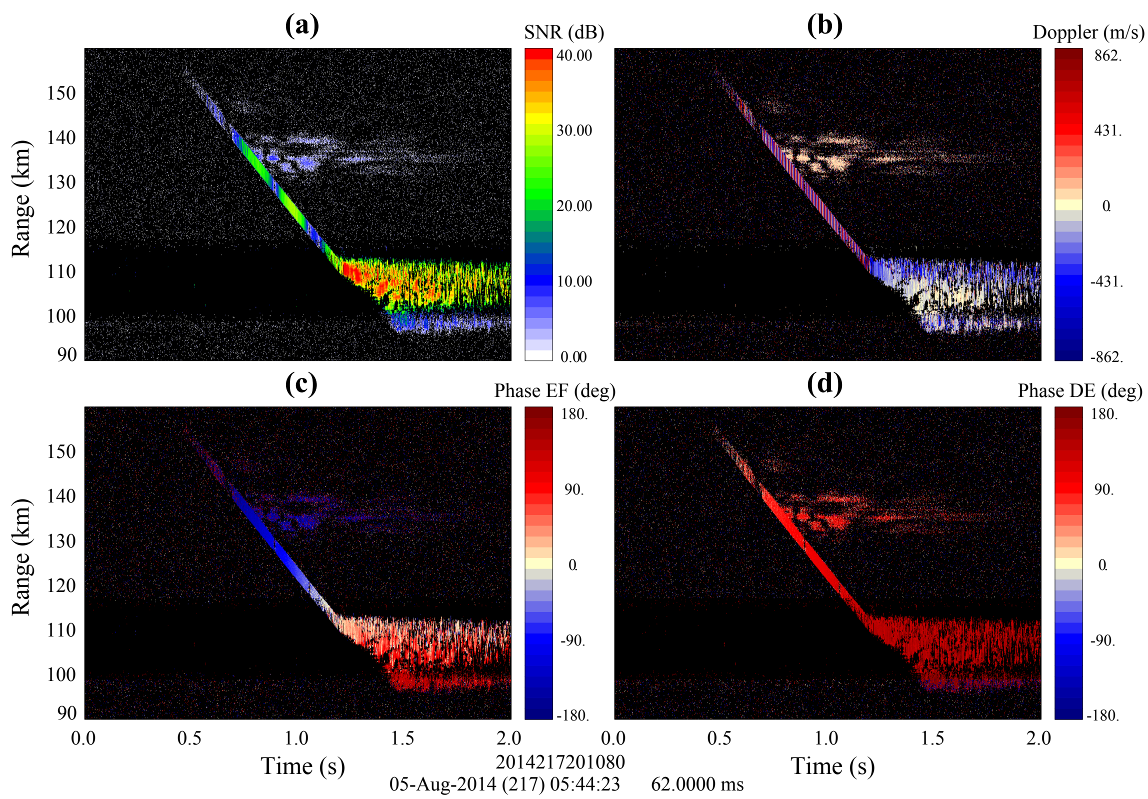

Figure 2-23. Figure 2-10 (b) HARM event after further statistical EEJ filtering according to phase differences from interferometric baseline EF. (a) The Range-Time-Intensity (RTI) plot. (b) Doppler speeds (ambiguous) from pulse to pulse. (c) Phase difference (ambiguous) between module receivers E and F. (d) Phase difference (ambiguous) between module receivers D and E.

2.6 Conclusions

We herein confirm our observations of high-altitude radar meteors (HARMs) based on the following evidence:

1. For the JRO near-zenith concentric beams, the wider Module-Module (M-M) receiving configuration observed more lobe/null structures in the head-echo trajectory than the narrower Quarter-Quarter (Q-Q) receiving counterpart;
2. High-altitude trail-echoes generated by the observed HARM events were ALL located at the **k⊥B** regions of the JRO array;
3. The SNR-matching to the beam-pattern technique for meteor head-echoes indicates an overhead flyby in the main beam;
4. The interferometric results from three independent antenna configurations (Quarter-Quarter, Quarter-Module, and Module-Module receiving configurations) yield an unambiguous angular trajectory of the observed meteor head-echoes allowing identification of multiple HARM events.
5. Thus far there has been no indication of meteors in distant sidelobes of the JRO beam. We additionally conclude that it is unrealistic to detect HARM (or any meteor) events with high-SNR features in the noise-dominated sidelobes of the JRO array.

Further, we now identify the "Dragon" trail-like events as always occurring at the **k⊥B** locus with meteor events for which the head-echoes are not always visible.

Chapter 3

Alternating Inter-Pulse Periods Technique

The current estimates of the meteoroid mass flux to Earth varies greatly—5-300 tons per day—with different estimation methods and assumptions [*Ceplecha et al.*, 1998; *Love and Brownlee*, 1993; *Mathews et al.*, 2001; *Nesvorny et al.*, 2010; *Plane*, 2012]. The meteoric mass influx is of special interest due to its influence on various upper atmosphere phenomena including the neutral and ion layers comprised of atomic metals such as Fe, Na, and K [*Chu et al.*, 2011; *Kane and Gardner*, 1993; *Raizada et al.*, 2015; *Zhou et al.*, 1999], sporadic-E [*Haldoupis et al.*, 2003; *Mathews*, 1998], and noctilucent clouds that are likely seeded by meteoric dust [*Blix et al.*, 1995]. According to the meteoroid momentum equation [*Bronshten*, 1983; *Mathews et al.*, 2003], the Doppler speed and deceleration is necessary to accurately estimate meteoroid mass thus enabling better estimates of the whole-earth micrometeoroid mass influx.

One commonly used technique applied to narrow-beam HPLA (High-Power, Large-Aperture) radar meteors for estimating meteoroid speeds is simply finding the range-change-rate through linear or second order polynomial fitting to the head-echo trajectory [*Chau and Woodman*, 2004]. As simple and straightforward as this approach is, this method requires sufficient sample points to overcome range and time resolution issues as well as noise, etc. This method often yields reasonable estimates of meteoroid speed evolution but only in an average sense. The "instantaneous" Doppler speed at a given time is not available and, often, because of poor range-rate resolution, no estimate of deceleration is available.

At, for example, 430 MHz the meteor line-of-sight Doppler shift can be estimated on an intra-pulse basis even for short (e.g., 20 μs) pulses as significant Doppler-induced phase shift occurs over this time interval [*Mathews et al.*, 2003]. At lower frequencies pulse-to-pulse estimation of Doppler speed using a single-lag autocorrelation (ACF) technique is widely used as this yields sufficiently measureable phase shift [*Gao and Mathews*, 2015a; 2015b]. For example, the two-way Doppler shift ($\Delta f = 2f_0 v/c$, where c is the speed of light, v is the radial speed, and f_0 is the operating frequency) for a 70 km/s radial speed meteor is 200.8 kHz at 430 MHz and 23.35 kHz at 50 MHz. Assuming a 20 μs transmitted pulse these Doppler shifts correspond to an intrapulse phase change of 1446° at 430 MHz but only 168° at 50 MHz. Taking SNR and system imperfections into consideration, such small phase change within one pulse is not significant enough to apply intra-pulse Doppler matching technique at 50 MHz. However, using the pulse-to-pulse autocorrelation for a 1 ms IPP yields 8406° phase shift at 50 MHz. This result is 2π ambiguous thus, while this method can be very accurate for measuring decelerations of meteoroids, the absolute Doppler speed can be significantly ambiguous. As transmitting a much longer pulse is not desirable because, while increasing the phase shift within one pulse, range resolution is sacrificed. This leaves us with using pulse-to-pulse Doppler estimates at JRO and methods for overcoming the 2π ambiguity must be considered.

The concept of utilizing non-uniform IPP in pulse Doppler radar is not new. *Maier* [1993] pointed out that non-uniform IPP pulse-Doppler radar waveforms could be used to suppress range ambiguities and to unambiguously determine frequencies above the Nyquist rate for the average pulse repetition interval (PRI), although its practical effectiveness was not tested. In this chapter, we introduce the alternating inter-pulse period (AIPP) specifically designed for meteor observations at Jicamarca Radio Observatory. It serves to de-alias range ambiguities of targets at higher altitude, such as satellites, and to accurately determine the unambiguous Doppler speed of fast-moving meteors.

Table 3-1. Alternating IPP Range Windows

Range Window 1	49.95 – 256.2 km
Range Window 2	313.8 – 514.65 km
Range Window 3	577.65 – 773.1 km
Range Window 4	841.5 – 1031.55 km

3.1 Range De-aliasing

The IPPs employed here are a sequence of 1723 μs, 1733 μs, 1747 μs, and 1759 μs (258.45 km, 259.95 km, 262.05km, and 263.85 km in range alias, respectively) as listed in Table 2-3. These four IPPs are carefully chosen prime numbers with distinct differences, 10 μs, 14 μs, 12 μs, and −36 μs. This sequence of alternating IPPs gives us an equivalent unambiguous range of 1044.3 km.

Taking the sampling window within each IPP into consideration (H0 = 49.95 km, Hf = 256.2 km), the unambiguous ranges corresponding to the Table 2-3 set of IPPs can be divided into 4 range windows, which are summarized in Table 3-1. Assuming a slowly-evolving (with respect to the AIPP sequence) point target located at a nearly constant range with respect to our radar, the Range-Time-Intensity (RTI) plots will show different patterns based on which range window the target is located in. Section 3.1.1 to 3.1.4 displays possible outcomes.

3.1.1 Case 1: Point Target in Range Window 1

Figure 3-1 illustrates the case when the target is located in Range Window 1. t_x indicates the time when each pulse was sent out, and t_r denotes the time when the return signal was received. Note that t_r may extend beyond the time of next transmit pulse. That is, t_r may extend into the following IPP. The recorded time difference between the transit and receive time is given as

$$\Delta t = t_{r1} - t_{x1} = t_{r2} - t_{x2} = t_{r3} - t_{x3} = t_{r4} - t_{x4} = \frac{2R_{target}}{c} \tag{3.1}$$

where R_{target} is the range of the target, c is the speed of light.

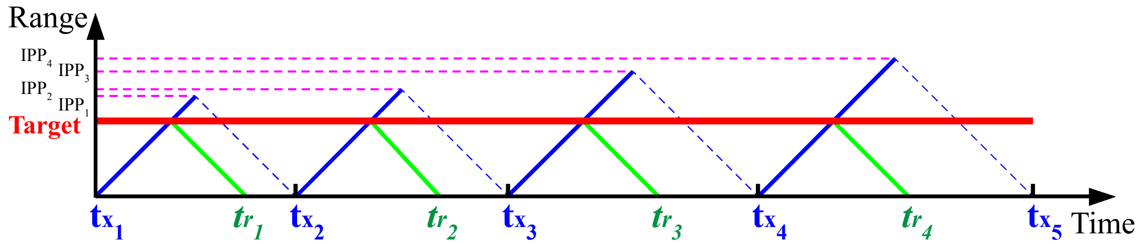

Figure 3-1. Point target in Range Window 1.

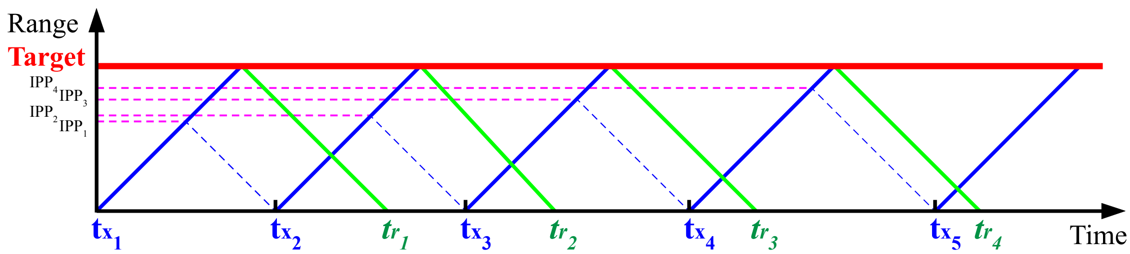

Figure 3-2. Point target in Range Window 2.

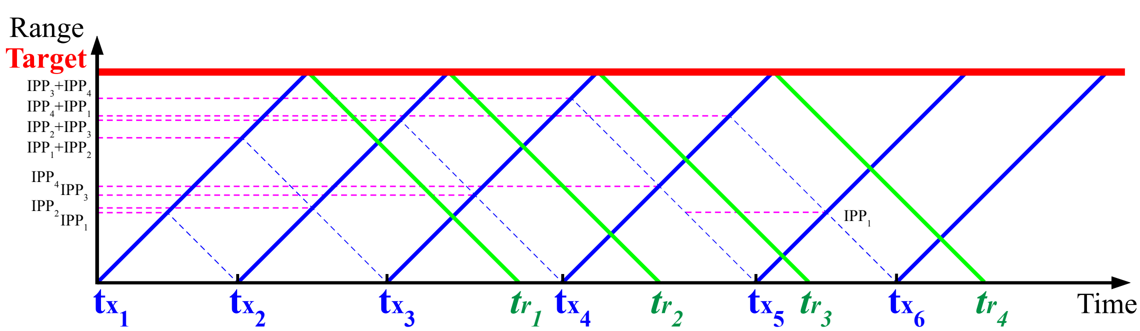

Figure 3-3. Point target in Range Window 3.

In this particular situation, even though the IPPs we employ were alternating, the time difference Δt reflects the true range of the target. That is, the AIPP technique does not affect the RTI plots for targets in Range Window 1. Typical targets in this range span include meteors, the Equatorial Electro-Jet, Sporadic-E, FAI blobs, etc.

3.1.2 Case 2: Point Target in Range Window 2

Figure 3-2 illustrates when the target is located in Range Window 2. Again, t_x indicates the time when each pulse was sent out, and t_r denotes the time when the return signal was received. We still have the "true" receiving time as in Equation (3.1).

However, due to the recording mechanics of the receiving system, the time reference is no longer the time when the pulse was sent out. Instead, it is the time when the following pulse was transmitted. Therefore, the apparent time differences are

$$\begin{aligned}
\Delta t_1 &= t_{r1} - t_{x2} = t_{r1} - t_{x1} - \tau_{IPP_1} = \Delta t - \tau_{IPP_1} \\
\Delta t_2 &= t_{r2} - t_{x3} = t_{r2} - t_{x2} - \tau_{IPP_2} = \Delta t - \tau_{IPP_2} \\
\Delta t_3 &= t_{r3} - t_{x4} = t_{r3} - t_{x3} - \tau_{IPP_3} = \Delta t - \tau_{IPP_3} \\
\Delta t_4 &= t_{r4} - t_{x5} = t_{r4} - t_{x4} - \tau_{IPP_4} = \Delta t - \tau_{IPP_4}
\end{aligned} \tag{3.2}$$

where τ_{IPP} is the individual IPP durations measured in μs, and Δt is the true time difference given in Equation (3.1). The numbered subscripts refer to individual IPPs in the AIPP sequence.

We can derive the offsets between two adjacent received-signal time differences as

$$\Delta t_{1\_2} = \Delta t_1 - \Delta t_2 = \Delta t - \tau_{IPP_1} - \left(\Delta t - \tau_{IPP_2}\right) = \tau_{IPP_2} - \tau_{IPP_1} = 10\ \mu s$$
$$\Delta t_{2\_3} = \Delta t_2 - \Delta t_3 = \Delta t - \tau_{IPP_2} - \left(\Delta t - \tau_{IPP_3}\right) = \tau_{IPP_3} - \tau_{IPP_2} = 14\ \mu s$$
$$\Delta t_{3\_4} = \Delta t_3 - \Delta t_4 = \Delta t - \tau_{IPP_3} - \left(\Delta t - \tau_{IPP_4}\right) = \tau_{IPP_4} - \tau_{IPP_3} = 12\ \mu s \tag{3.3}$$
$$\Delta t_{4\_1} = \Delta t_1 - \Delta t_1 = \Delta t - \tau_{IPP_4} - \left(\Delta t - \tau_{IPP_1}\right) = \tau_{IPP_1} - \tau_{IPP_4} = -36\ \mu s$$

Notice from the above equations that, even if the target is at a constant range, the apparent ranges due to alternating IPPs are different from one IPP to the next. This results in staggered ranges in the uncompensated RTI plots.

3.1.3 Case 3: Point Target in Range Window 3

Figure 3-3 illustrates the case when the target is located in Range Window 3. The "true" receiving time is again as shown in Equation (3.1). However the time reference is aliased by two IPPs. Therefore,

$$\Delta t_1 = t_{r1} - t_{x3} = t_{r1} - t_{x1} - \tau_{IPP_1} - \tau_{IPP_2} = \Delta t - \left(\tau_{IPP_1} + \tau_{IPP_2}\right)$$
$$\Delta t_2 = t_{r2} - t_{x4} = t_{r2} - t_{x2} - \tau_{IPP_2} - \tau_{IPP_3} = \Delta t - \left(\tau_{IPP_2} + \tau_{IPP_3}\right)$$
$$\Delta t_3 = t_{r3} - t_{x5} = t_{r3} - t_{x3} - \tau_{IPP_3} - \tau_{IPP_4} = \Delta t - \left(\tau_{IPP_3} + \tau_{IPP_4}\right) \tag{3.4}$$
$$\Delta t_4 = t_{r4} - t_{x6} = t_{r4} - t_{x4} - \tau_{IPP_4} - \tau_{IPP_1} = \Delta t - \left(\tau_{IPP_4} + \tau_{IPP_1}\right)$$

Therefore, the differences of receiving times are,

$$\Delta t_{1\_2} = \Delta t_1 - \Delta t_2 = \tau_{IPP_3} - \tau_{IPP_1} = 24\ \mu s$$
$$\Delta t_{2\_3} = \Delta t_2 - \Delta t_3 = \tau_{IPP_4} - \tau_{IPP_2} = 26\ \mu s$$
$$\Delta t_{3\_4} = \Delta t_3 - \Delta t_4 = \tau_{IPP_1} - \tau_{IPP_3} = -24\ \mu s \tag{3.5}$$
$$\Delta t_{4\_1} = \Delta t_1 - \Delta t_1 = \tau_{IPP_2} - \tau_{IPP_4} = -26\ \mu s$$

Equation (3.5) also indicates staggered ranges in the corresponding RTI plot, but with a different pattern than in Case 2.

3.1.4 Case 4: Point Target in Range Window 4

In a similar manner, the differences of receiving times for point targets in Range Window 4 are,

$$\begin{aligned}
\Delta t_{1_2} &= \Delta t_1 - \Delta t_2 = \tau_{IPP_4} - \tau_{IPP_1} = 36\ \mu\text{s} \\
\Delta t_{2_3} &= \Delta t_2 - \Delta t_3 = \tau_{IPP_1} - \tau_{IPP_2} = -10\ \mu\text{s} \\
\Delta t_{3_4} &= \Delta t_3 - \Delta t_4 = \tau_{IPP_2} - \tau_{IPP_3} = -14\ \mu\text{s} \\
\Delta t_{4_1} &= \Delta t_1 - \Delta t_1 = \tau_{IPP_3} - \tau_{IPP_4} = -12\ \mu\text{s}
\end{aligned} \tag{3.6}$$

Equation (3.6) indicates a mirrored pattern relative to Case 2.

3.1.5 Case 5: Point targets above Range Window 4

For targets above Range Window 4, this technique yields a repetitive pattern as in Case 1-4. Thus we cannot distinguish their true ranges due to the ambiguity (range aliasing) issues. This situation can be remedied by extending the AIPP sequence developed here. In the observations outlined here, our principle targets are meteors located in Range Window 1. We are also concerned with Low-Earth Orbit (LEO) satellites with orbital altitudes lower than ~1000 km. Consequently; targets above Range Window 4 are not in the scope of our discussion except that these satellite returns would be aliased into the net AIPP range window. Nevertheless, as pointed out above, higher unambiguous ranges could always be achieved simply by increasing the number of IPPs in the AIPP sequence utilized.

3.1.6 Summary

As discussed above, targets in different range windows will yield different patterns in their Range-Time-Intensity (RTI) plots. These patterns offer us the necessary information to de-alias range ambiguity of detected targets. As is clear in Figure 3-1 to, and then from Equations (3.1) to (3.6), different and distinctive RTI patterns are observed for targets in each of the four range windows. These patterns are modeled as shown in Figure 3-4. Observational examples of these patterns from point targets (satellites) in different ranges windows are shown in Figure 3-5.

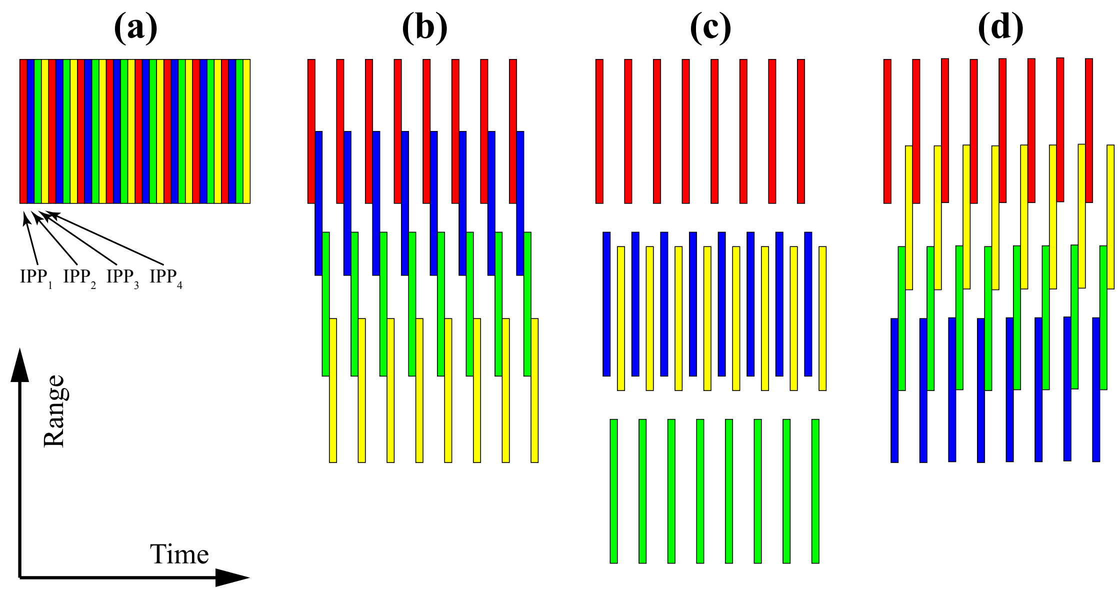

Figure 3-4. Different RTI pattern for point targets in (a) Range Window 1, (b) Range Window 2, (c) Range Window 3, and (d) Range Window 4. Different colors indicate pulses with alternating IPPs.

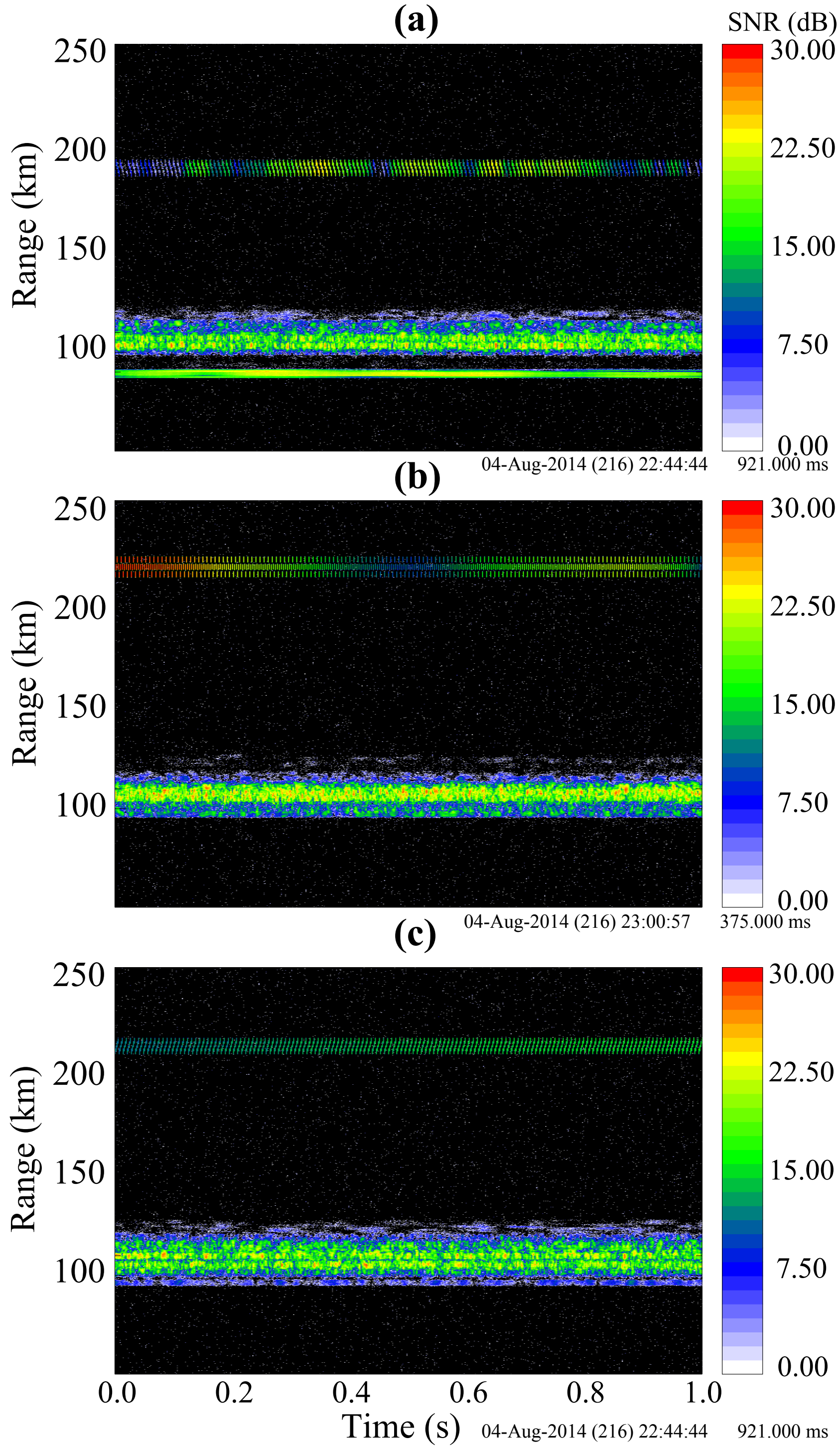

Figure 3-5. RTI plots of targets (satellites) at higher altitudes in (a) Range Window 2, (b) Range Window 3, and (c) Range Window 4. These patterns are modeled for different range windows in Figure 3-4. Notice that in all three RTI plots the return from the EEJ is not altered since it is located in Range Window 1

3.2 Doppler Speed De-aliasing

3.2.1 Doppler Speed from Pulse to Pulse

The fraction of a wavelength a (coherent over the IPP scale) target has moved during two adjacent Inter-Pulse Periods (IPPs) can be determined very precisely by finding the pulse–to-pulse phase auto-correlation function (ACF) of the return signals for adjacent IPPs. This yields the line-of-sight Doppler speed of the detected objects.

Suppose the received (complex) baseband voltages from two adjacent IPPs are:

$$\begin{aligned} V_t &= e^{j\omega_D t} \\ V_{t+\tau} &= e^{j\omega_D (t+\tau)} \end{aligned} \tag{3.7}$$

where t is a randomly chosen time reference, τ is the length of IPP, $\omega_D = 2\pi f_D$ is the Doppler angular speed, with f_D being the Doppler frequency.

Formally the phase ACF from pulse to pulse (or pulse-to-pulse cross-correlation) yields

$$ACF = V_t \times V_{t+\tau}{}^* = e^{j\omega_D t} \times e^{-j\omega_D (t+\tau)} = e^{-j\omega_D \tau} = e^{j\Delta\phi} \tag{3.8}$$

Therefore, the phase difference from pulse to pulse is:

$$\Delta\phi = -\omega_D \tau = -2\pi f_D \tau \tag{3.9}$$

The relationship between Doppler frequency and Doppler speed is given as:

$$f_D = \frac{2v_D}{c} f_0 = \frac{2v_D}{\lambda_0} \tag{3.10}$$

where f_0 is the operating frequency of the carrier, c is the speed of the carrier waves in the medium, in this case, the speed of light, $\lambda_0 = c/f_0$ is the carrier wavelength. As the radar observes the net scattered Doppler shift, the wavenumber is referred to as the scattering wavenumber $k_s = 4\pi/\lambda_0$.

Combine Equation (3.9) and (3.10), we have the Doppler speed of a moving target from pulse to pulse:

$$v_D = \frac{\lambda_0}{2} f_D = -\frac{\lambda_0 \Delta\phi}{4\pi\tau} \tag{3.11}$$

$\Delta\phi$ is potentially 2π ambiguous, but when there is no phase ambiguity, i.e., when $\Delta\phi$ reflects the true phase progression from IPP to IPP, the resultant v_D gives the true (unaliased) Doppler speed of the detected target. The uniformity of IPPs is not a concern in this case.

Similar to angular ambiguity in interferometry discussed in Section 2.3, that is that $e^{j\Delta\phi}$ in Equation (3.8) is a periodic function with period 2π. Conventionally $\Delta\phi$ is only computed in the interval of $[-\pi, \pi]$. Hence the resultant Doppler speed of a moving target is in the range of

$$[v_D] \in \left[-\frac{\lambda_0}{4\tau}, \frac{\lambda_0}{4\tau}\right] \tag{3.12}$$

where $[v_D]$ indicates that the Doppler speed is ambiguous as a result of phase wrapping.

Consequently, the ambiguity in Doppler speed is introduced herein.

3.2.2 Doppler Speed Ambiguity Removal

As AIPP is employed in this dataset, the Doppler plots of meteor head-echoes also show a rapid IPP-to-IPP “striping”—shown in Figure 3-6 Panel (b)—in what would otherwise be the smoother Doppler progression shown in Figure 3-6 Panel (a). This is the collective result of phase wrapping and the non-uniform sampling of phase progression due to use of the AIPP sequence. This rapid phase/Doppler discontinuity can be used, as shown next, to recover the true, unambiguous Doppler speed of meteor head-echoes.

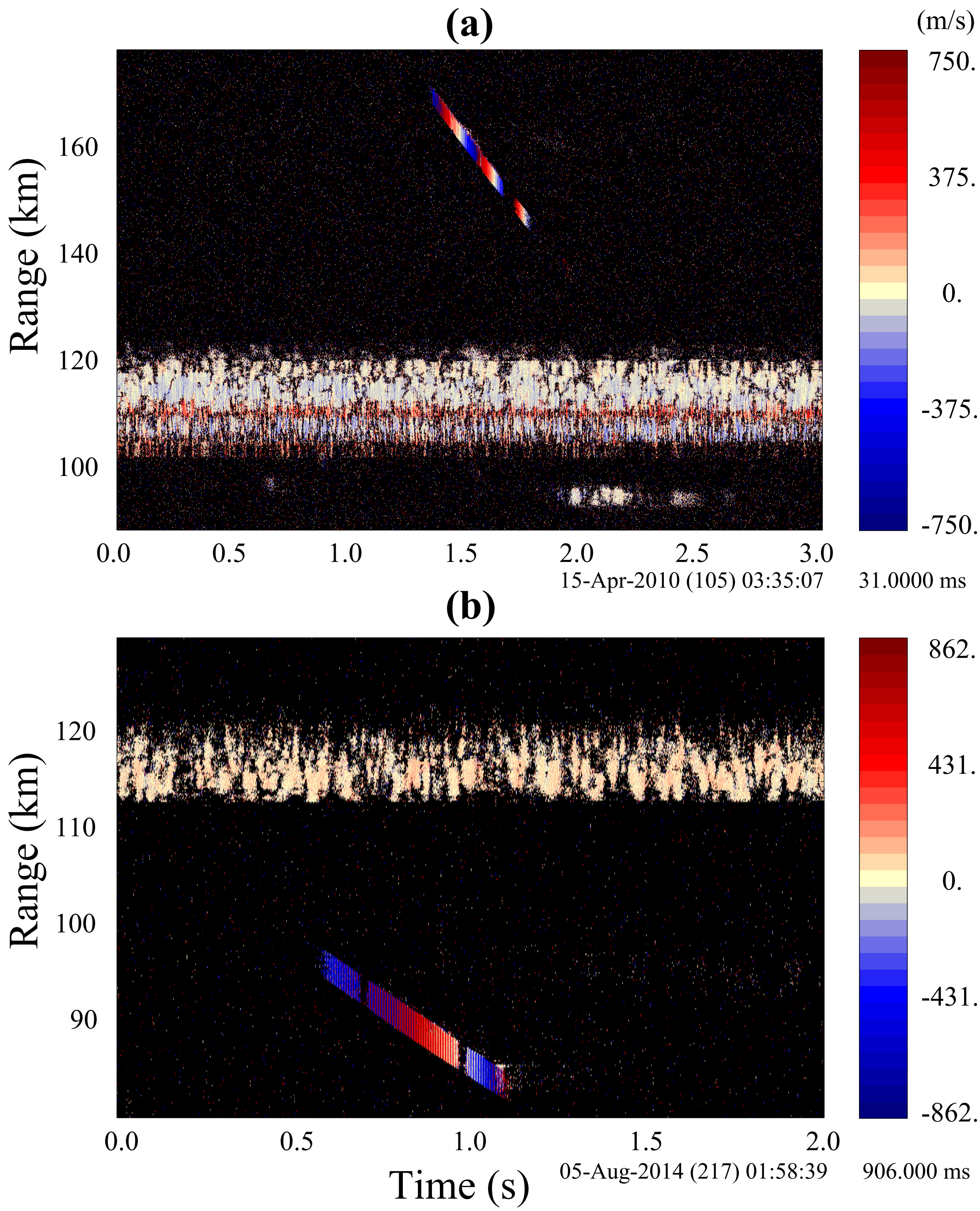

Figure 3-6. Doppler comparison. (a) Meteor event from 2010-04-15 observation with constant 2ms IPP. (b) Meteor event from 2014-08-05 observations with the 4 IPP alternating IPP sequence. Note that the Doppler evolution in (a) is smooth while in (b) there is Doppler "striping". Doppler processing in this assumes a constant IPP thus introducing the striping. In both cases the FAI scattering is smooth and centered near zero Doppler.

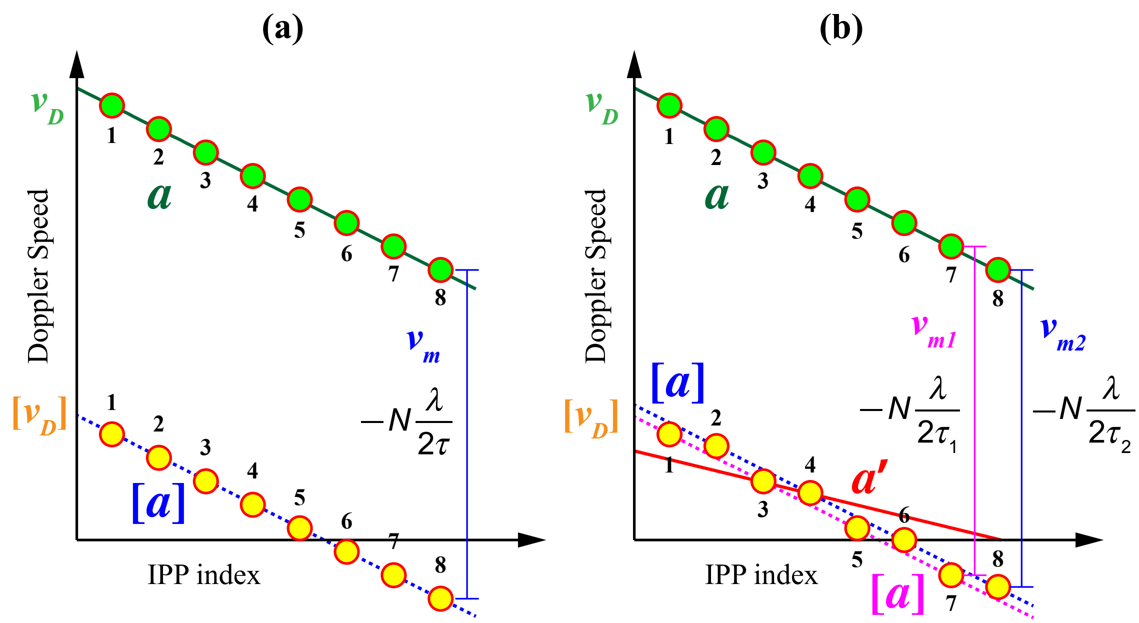

Figure 3-7. Illustration of Doppler speed ambiguity due to phase wrapping with (a) constant IPP, τ, and (b) two alternating IPPs, τ_1 and τ_2. Each circle represents the apparent or real Doppler speed point derived from the phase difference from IPP to IPP. Green circles denote true Doppler speeds v_D. Yellow circles represent the ambiguous Doppler speeds $[v_D]$. v_m $(= -N\lambda_0/2\tau)$ represents the missing Doppler speed due to N cycles of phase wrapping.

The true Doppler speed of a detected target can be expressed in two parts, the ambiguous (aliased) Doppler speed and the missing Doppler speed due to phase wrapping:

$$v_D = -\frac{\lambda\Delta\phi}{4\pi\tau} = -\frac{\lambda}{4\pi\tau}([\Delta\phi] + N2\pi) = -\frac{\lambda[\Delta\phi]}{4\pi\tau} - N\frac{\lambda}{2\tau} = [v_D] + v_m \tag{3.13}$$

where $\Delta\phi$ is the actual phase difference from IPP to IPP, $[\Delta\phi] \in [-\pi, \pi]$ denotes the wrapped phase difference, N is an arbitrary integer indicating the missing multiples of 2π due to phase wrapping. $[v_D]$ symbolizes the ambiguous Doppler speed , and v_m represents the missing Doppler speed due to phase wrapping.

As shown in Figure 3-7 panel (a), when constant IPP—τ is unchanging—is used, all ambiguous Doppler speeds from IPP to IPP ($[v_D]$) are shifted equally $v_m = -N\frac{\lambda}{2\tau}$ from their true values v_D. As a result, the temporal rate of change of ambiguous Doppler speeds $[a]$ is the same as the original temporal rate of change of true Doppler speeds, a.

$$\begin{aligned} a = \frac{v_{D_2} - v_{D_1}}{\tau} = \frac{-\frac{\lambda\Delta\phi_2}{4\pi\tau} - -\frac{\lambda\Delta\phi_1}{4\pi\tau}}{\tau} = \frac{-\frac{\lambda[\Delta\phi_2]}{4\pi\tau} - N\frac{\lambda}{2\tau} - \left(-\frac{\lambda[\Delta\phi_1]}{4\pi\tau} - N\frac{\lambda}{2\tau}\right)}{\tau} \\ = \frac{-\frac{\lambda[\Delta\phi_2]}{4\pi\tau} - \left(-\frac{\lambda[\Delta\phi_1]}{4\pi\tau}\right)}{\tau} = \frac{[v_{D_2}] - [v_{D_1}]}{\tau} = [a] \end{aligned} \tag{3.14}$$

According to Equation (3.14), N gets cancelled out. This leaves no hint for us to find the missing multiples N of 2π. Therefore, true Doppler speeds could not be recovered with constant IPP.

However, when alternating IPPs are employed, τ is not a constant anymore. As shown in Figure 3-7 panel (b), there are slight differences in the apparent Doppler speeds (total phase shift) from one IPP to another due to processing assumptions of a constant τ. These differences cause discontinuity in the ambiguous Doppler speeds $[v_D]$ as seen in the “striping” shown in Figure 3-6 panel (b), and could be used to recover the true Doppler speeds of detected targets.

Using two alternating IPPs (τ_1 and τ_2) as an example, the relationship between the temporal rate of change of ambiguous Doppler speeds (a') and the original temporal rate of change of true Doppler speeds (a) is given as:

$$
\begin{aligned}
a = \frac{v_{D2} - v_{D1}}{\tau_1} = \frac{-\frac{\lambda\Delta\phi_2}{4\pi\tau_2} - -\frac{\lambda\Delta\phi_1}{4\pi\tau_1}}{\tau_1} &= \frac{-\frac{\lambda[\Delta\phi_2]}{4\pi\tau_2} - N\frac{\lambda}{2\tau_2} - \left(-\frac{\lambda[\Delta\phi_1]}{4\pi\tau_1} - N\frac{\lambda}{2\tau_1}\right)}{\tau_1} \\
&= \frac{-\frac{\lambda[\Delta\phi_2]}{4\pi\tau_2} - \left(-\frac{\lambda[\Delta\phi_1]}{4\pi\tau_1}\right)}{\tau_1} - N\frac{\lambda}{2\tau_1}\left(\frac{1}{\tau_2} - \frac{1}{\tau_1}\right) \\
&= \frac{[v_{D2}] - [v_{D1}]}{\tau_1} - N\frac{\lambda}{2\tau_1}\frac{\tau_1 - \tau_2}{\tau_1\tau_2} = a' - N\frac{\lambda}{2\tau_1}\frac{\tau_1 - \tau_2}{\tau_1\tau_2}
\end{aligned}
\tag{3.15}
$$

According to Equation (3.15), N is not cancelled out. But the original temporal rate of change of true Doppler speeds (a) is still unknown. In order to get N, a must be determined first.

When the temporal change of every other Doppler speed points is examined, the time difference between every other points becomes constant ($\tau_1 + \tau_2$). Consequently, it reduces to the case of constant IPP—only longer—as in Figure 3-7 panel (a).

$$
\begin{aligned}
a = \frac{v_{D3} - v_{D1}}{\tau_1 + \tau_2} = \frac{-\frac{\lambda\Delta\phi_3}{4\pi\tau_1} - -\frac{\lambda\Delta\phi_1}{4\pi\tau_1}}{\tau_1 + \tau_2} &= \frac{-\frac{\lambda[\Delta\phi_3]}{4\pi\tau_1} - N\frac{\lambda}{2\tau_1} - \left(-\frac{\lambda[\Delta\phi_1]}{4\pi\tau_1} - N\frac{\lambda}{2\tau_1}\right)}{\tau_1 + \tau_2} \\
&= \frac{-\frac{\lambda[\Delta\phi_3]}{4\pi\tau_1} - \left(-\frac{\lambda[\Delta\phi_1]}{4\pi\tau_1}\right)}{\tau_1 + \tau_2} = \frac{[v_{D3}] - [v_{D1}]}{\tau_1 + \tau_2} = [a]
\end{aligned}
\tag{3.16}
$$

Therefore, the missing multiples of 2π due to phase wrapping is found as:

$$
N = (a' - [a])\frac{2\tau_1}{\lambda}\frac{\tau_1\tau_2}{\tau_1 - \tau_2}
\tag{3.17}
$$

After the determination of N, true phase difference $\Delta\phi$ could be derived by adding multiples of 2π back to wrapped phase difference $[\Delta\phi]$ accordingly. Therefore, true Doppler speeds are recovered.

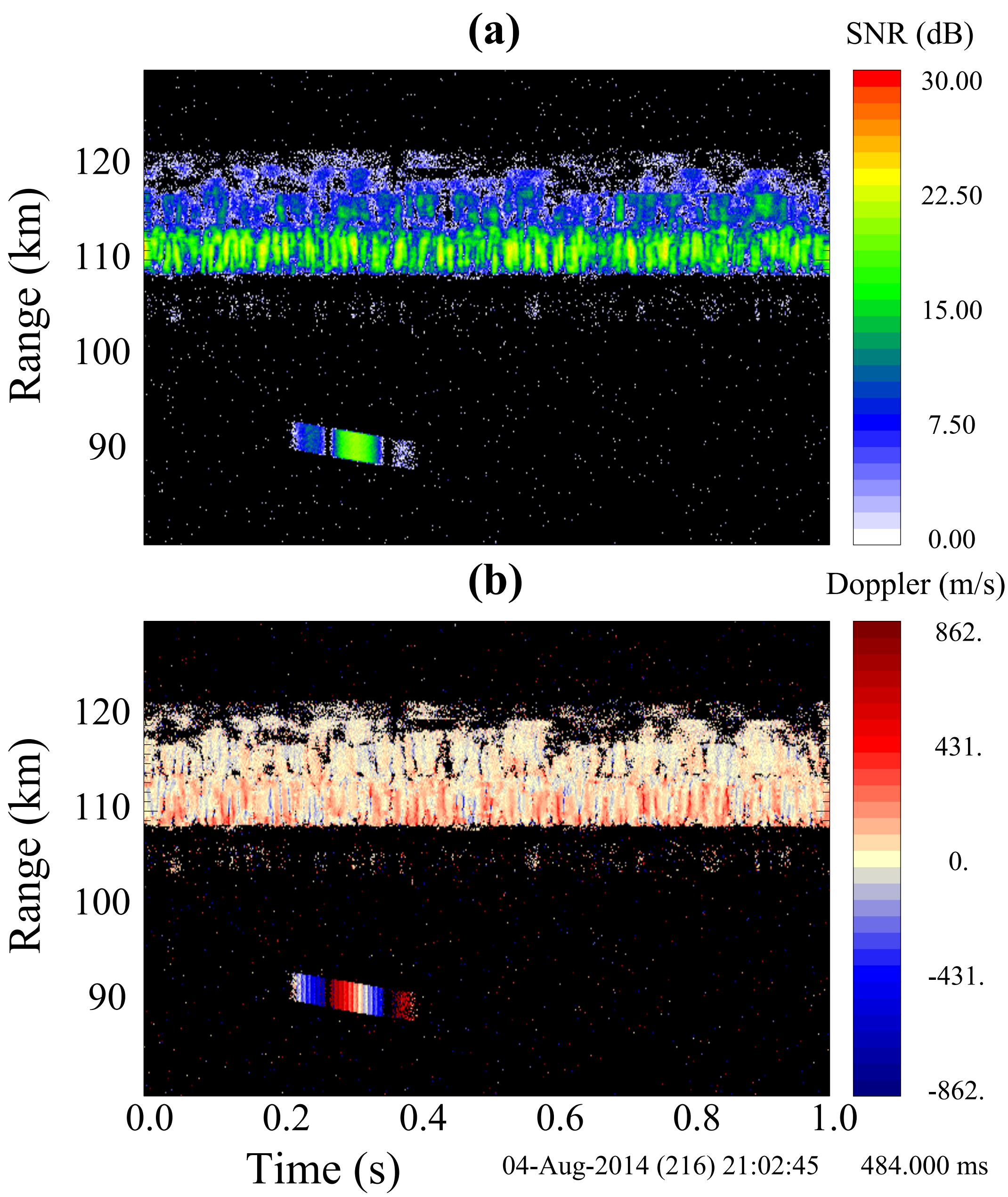

Figure 3-8. (a) Range-Time-Intensity (RTI) plot, and (b) Doppler plot of an example meteor event for which Doppler de-aliasing using AIPP information will be illustrated. Notice the “striping” in the Doppler plot of the meteor head-echo.

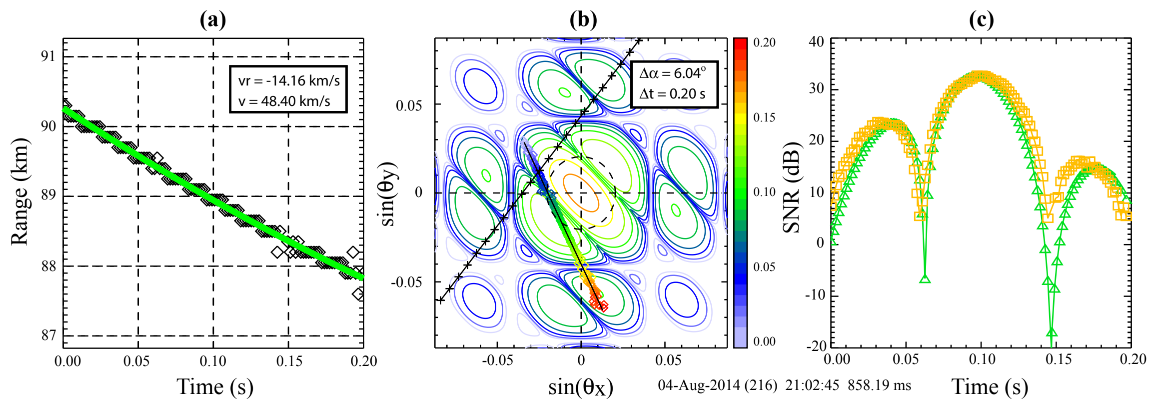

Figure 3-9. Further characterization of the head-echo meteor event shown in Figure 3-8. (a) Range vs. time; (b) $\sin\theta_x$ vs. $\sin\theta_y$ (c) SNR vs. time. In panel (a), the fitted range vs. time trajectory is given in green. The fitted slope corresponds to a 14.16 km/s line-of-sight speed towards the radar. The absolute speed calculated from the 3-D (range and angular) position information is 48.40 km/s. Panel (b) gives the unwrapped interferometric trajectory of the head echoes as a function of time. The phase-fitting trajectory is given as the thick black solid line. The meteor trajectory is from northeast to southwest with an elevation angle of 23.20°. The thin solid line overlaid with plus signs indicates the radar $\mathbf{k}\perp\mathbf{B}$ region at the altitude of 100 km at JRO. The theoretical radiation pattern (in dB) is also plotted in the background. In panel (c), the measured SNR versus time is plotted in yellow, while the expected relative SNR, based on the theoretical antenna pattern and angular positions from panel (b), is denoted in green.

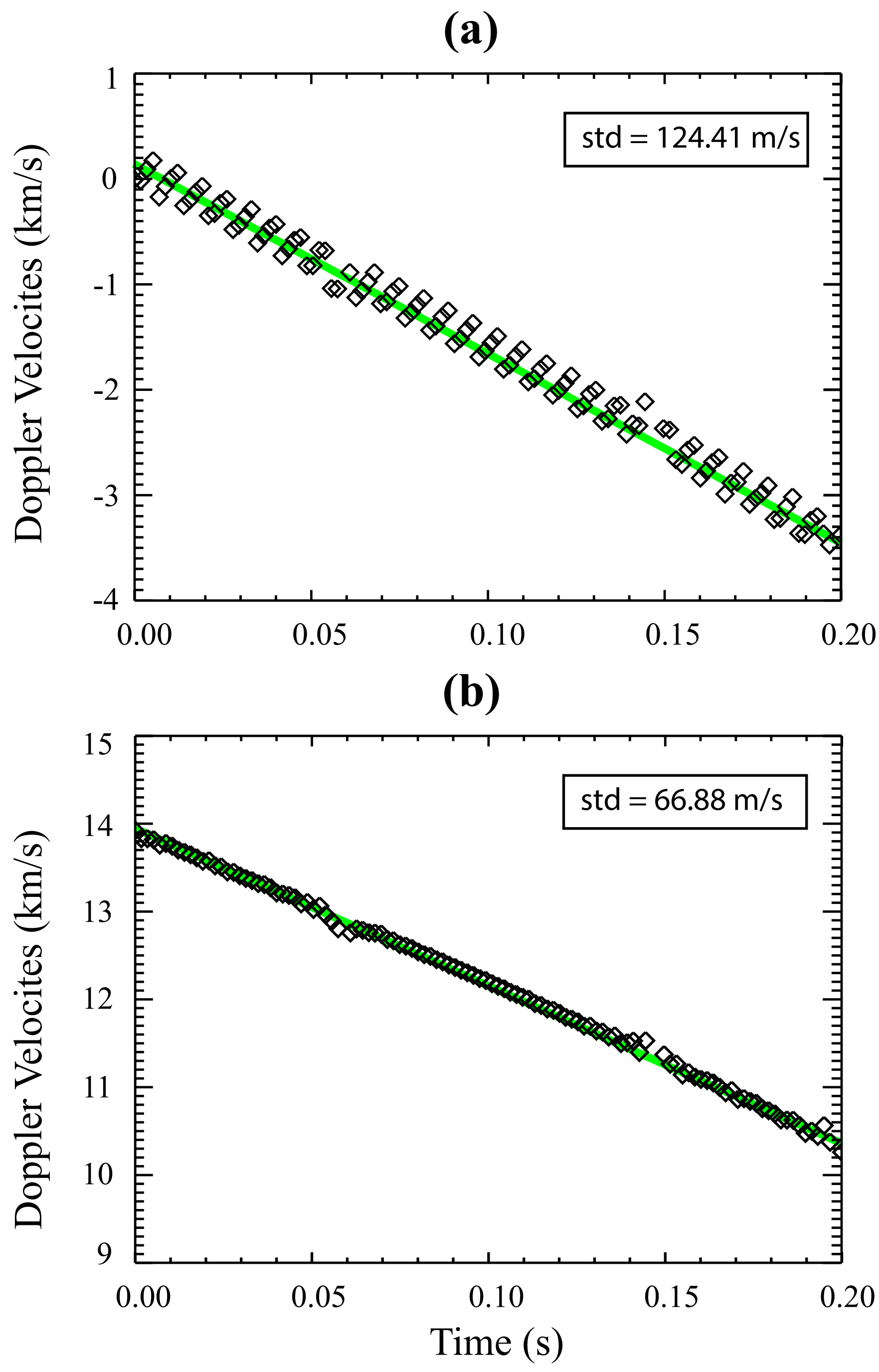

Figure 3-10. Doppler speeds of the meteor event shown in Figure 3-8 (a) before, and (b) after phase ambiguity removal. The missing Doppler speed in this case is due to N=−8 cycles of phase wrapping. Green lines are linear fitting of Doppler speed data points. The standard deviations between Doppler data points and linear fitting are also calculated.

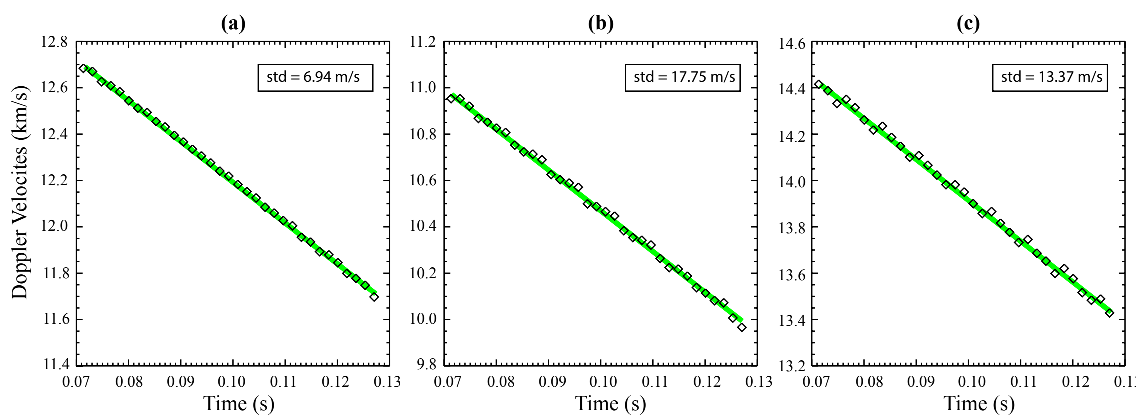

Figure 3-11. Doppler de-aliasing sensitivity test. Results of (a) adding the correct integer N=−8 (×2π), (b) adding one extra cycle—N+1 (×2π), (c) adding one less—N−1 (×2π), to the phase difference $\Delta\phi$ from IPP to IPP. Green lines are the linear fitting of Doppler speeds according to each correction integer N. The standard deviations between Doppler data points and linear fitting are also calculated. Note that this technique is very sensitivity to incorrect phase correction.

The meteor event shown in Figure 3-8 is chosen as an example to illustrate how Doppler speed ambiguity is removed by using the technique discussed above. Its head-echo characterizations are plotted in Figure 3-9. This meteor event took place in the traditional meteor zone. It has a beginning height of 90.3$\pm$0.15 km and ending height ~87.9$\pm$0.15 km, with a line-of-sight speed of ~14.16 km/s approaching the radar. The meteor head-echo passed through three antenna lobe structures causing well-defined nulls. The layered structure at from ~110 km to ~120 km is the weak nighttime Equatorial Electro-Jet (EEJ), and the faint layer at ~105km is likely a faint Sporadic-E layer [Malhotra et al., 2008].

Figure 3-10 shows the Doppler speed progression of the meteor head-echo event given in Figure 3-8. In the process for determining the ambiguity integer N, all Doppler points are lined up employing the technique introduced in *Gao and Mathews* [2015b] to address the phase ambiguity issue in interferometry. This process removes the "zig-zag" effect that occurs when the phase evolution exceeds 2π during observation. Panel (a) shows the ambiguous AIPP Doppler speeds. It is obvious that every four points—we used four alternating IPPs in this AIPP example—gives the temporal rate of change($[a]$), which is the same as the original temporal rate of change of true Doppler speeds (a). Notice also the discontinuity (a') caused by phase wrapping and non-uniform sampling of phase progression with alternating IPPs. Panel (b) shows the result after Doppler ambiguity removal with N=$-$8 (×2π) added back onto the ambiguous phase difference $[\Delta\phi]$ to recover the true Doppler speeds. Note that the Doppler speed progression becomes continuous after the adjustment. Negative *N* indicates that the phase evolution corresponds to a Doppler speed towards the receiver, while positive *N* indicates that the Doppler speed is moving away from the receiver.

The initial guess of integer N is obtained from range-change-rate in Figure 3-9 Panel (a). Then the search for the correct integer N is completed through minimizing the standard deviation error between the Doppler fitting and the actual Doppler data points.

The AIPP technique to determine absolute Doppler speeds is very robust and resistant to errors. Only when the correct N—the correct amount of phase—is added back to the ambiguous phase difference [$\Delta\phi$], does the final Doppler progression become continuous. Figure 3-11 illustrates the sensitivity of this Doppler recovery technique. Panel (a) shows a smooth Doppler progression when the correct multiples $N=-8$ ($\times 2\pi$) phase is added. Also $N=-8$ yields the minimal standard deviation error, thus indicates the optimal de-aliasing result. Panel (b) and (c) show that when there is difference of only $\pm 2\pi$ from the correct phase adjustment, the Doppler discontinuity still exists and is easily detected. Therefore, the AIPP Doppler speed ambiguity removal technique guarantees the recovery of absolute Doppler speeds from meteor head-echoes in the case of the JRO pulse-to-pulse Doppler estimation method. It is manifested as the smoothest progression of Doppler speed date points and the smallest standard deviation between the data points and their corresponding fitted line.

Figure 3-12 and Figure 3-13 show a meteor event with complex decelerating process. The alternating IPP technique frees us from making assumptions as in applying range-time fitting to get range-change-rates. It enables measurement of the absolute Doppler speed of meteor head-echoes regardless of the deceleration profile.

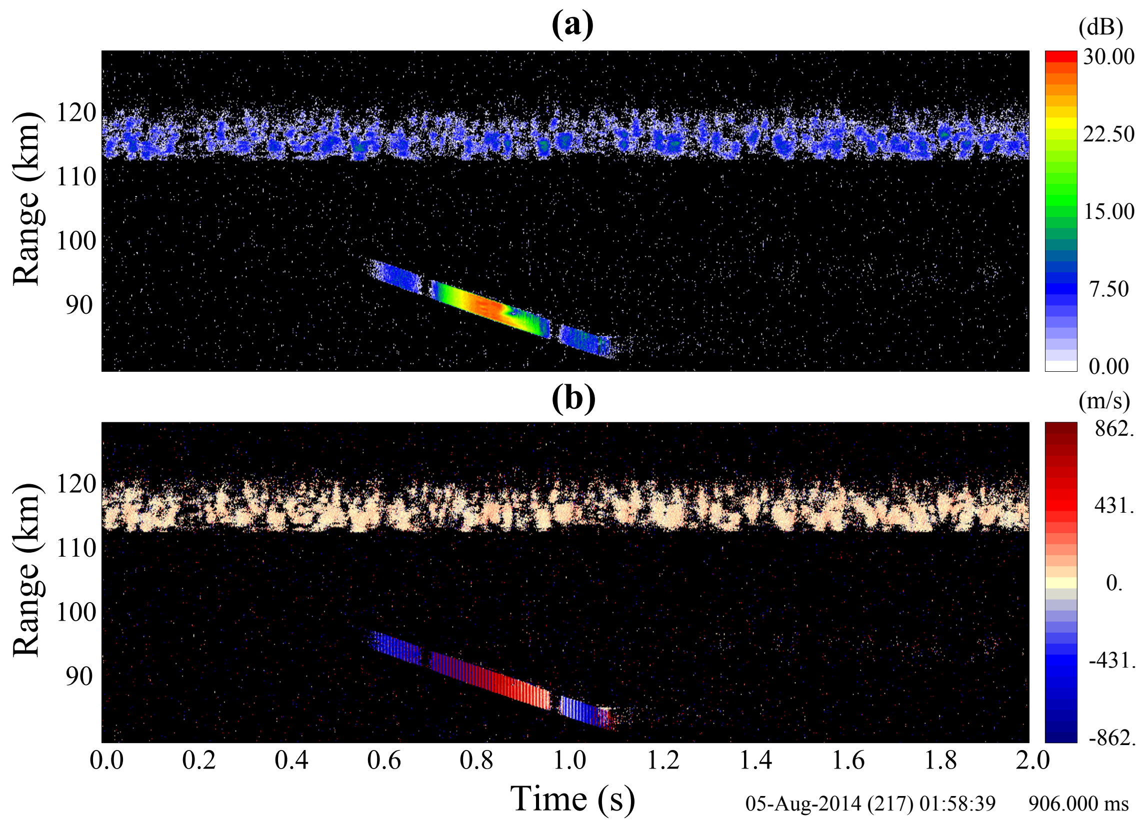

Figure 3-12. (a) Range-Time-Intensity (RTI) plot, and (b) Doppler plot of another meteor event with a more complex deceleration profile relative to the Figure 3-8 event. Notice the “striping” in the Doppler plot of the meteor head-echo.

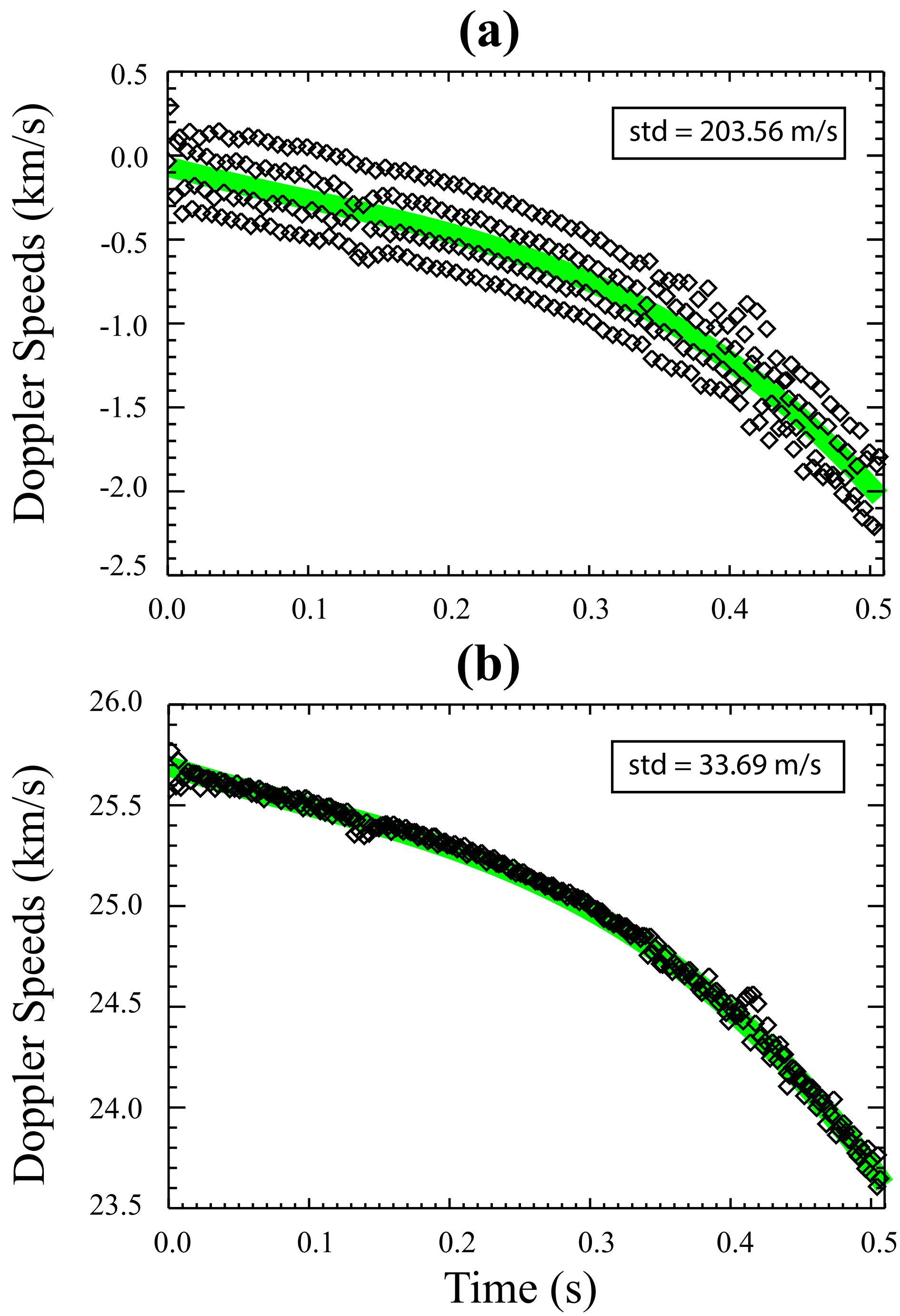

Figure 3-13. Doppler speeds of the meteor event shown in Figure 3-12 (a) before, and (b) after phase ambiguity removal (N=−15). Green curves are polynomial fitting of Doppler speed data points of degree of 3. The standard deviations between the data points and polynomial fitting are also calculated.

3.2.3 Summary

The alternating-IPP (AIPP) technique proves to be successful in resolving both Doppler speed and range ambiguities for meteor and satellite observations at JRO. This new technique enables recovery of absolute instantaneous (IPP-to-IPP) Doppler speeds of meteor head-echoes and the true ranges of LEO satellites. It remains effective for meteors with complex decelerating processes and frees us from making any assumptions of the deceleration variation in applying range-time fitting to obtain range-change-rates.

Accurate Doppler speeds of meteor head echoes will facilitate better estimates of the micrometeoroid mass flux as well as individual orbits and thus origins of these meteoroids. This alternating-IPP technique is designed specifically for observations when the radar system is operating at lower frequencies and with the shorter IPPs required to maintain sufficient time resolution of rapidly evolving events. The AIPP method can be easily adapted to other radar systems including the 430 MHz UHF radar at Arecibo Observatory. In this case the intra-pulse Doppler information [*Mathews et al.*, 2003] can be greatly refined by using the AIPP approach and pulse-to-pulse phase unwrapping to potentially achieve meter/sec speed resolution. This technique can be further refined by carefully choosing the differences between adjacent IPPs. By doing this, we can make the staggering in the Doppler and range outcomes even more obvious and thus more sensitive to phase ambiguity. Some distinctive prime number differences between adjacent IPPs would be highly recommended for future experiments where “blanking receive windows” when transmitting can be eliminated if needed. Of particular interest is use of the AIPP approach with short IPPs for classical upper HF and lower UHF meteor radars thus solving the undersampling dilemma and resolving features such as fragmentation and onset of the “ceiling effect” [*Roy et al.*, 2007].

Furthermore, the AIPP technique offers a method for separating meteor events from the EEJ (Equatorial ElectroJet) scattering when they occur in the same range. Meteor events have high Doppler speeds thus have large absolute N values. That is, unlike most meteor events, the EEJ return usually exhibits small Doppler shifts and no phase ambiguity.

Chapter 4

Future Work

Meteor observation experiments need to be carried out to collect more data on high-altitude radar meteor (HARM) events in the future. The new experiment configuration is suggested as in Figure 4-1.

This is an improvement of the radar configuration shown in Figure 2-3 in the following ways:

(1) It uses the same diagonal quarter arrays for transmission as in the experiment discussed in Section 2.2. This transmit configuration yields a unique radiation pattern of the main beam, which helps to utilize the headecho-matching technique to fine-tone observed radar meteors within the beam. In addition, the beam is also slightly narrower along the **k⊥B** direction, which facilitates using EEJ as a phase reference to calibrate the JRO array.

(2) It keeps the 3 interferometric receiving pairs in the previous experiment, BC-AB as the quarter-quarter receiving pairs, EG-GF as the module-module receiving pairs, and AF-GC as the quarter-module receiving pairs (Refer to Figure 4-1). However, more modules receivers offer more flexibility in choosing baselines. For example, HD-EI provides another perpendicular interferometric baselines with spacing of 80.50 meters, rotated ~26.565° clockwise with respect to the coordinates defined by the conventional Q-Q and M-M pairs. Moreover, four ajacent module receivers can be synthesized into one larger receiver, whose phase center is the also the common physical center of these four modules (Refer to Figure 4-2). This will increase the SNR of detected targets without narrowing the ambiguity circle.

(3) Combined with the Hysell module, which is located to the west of the main array, it can be applied to radar imaging.

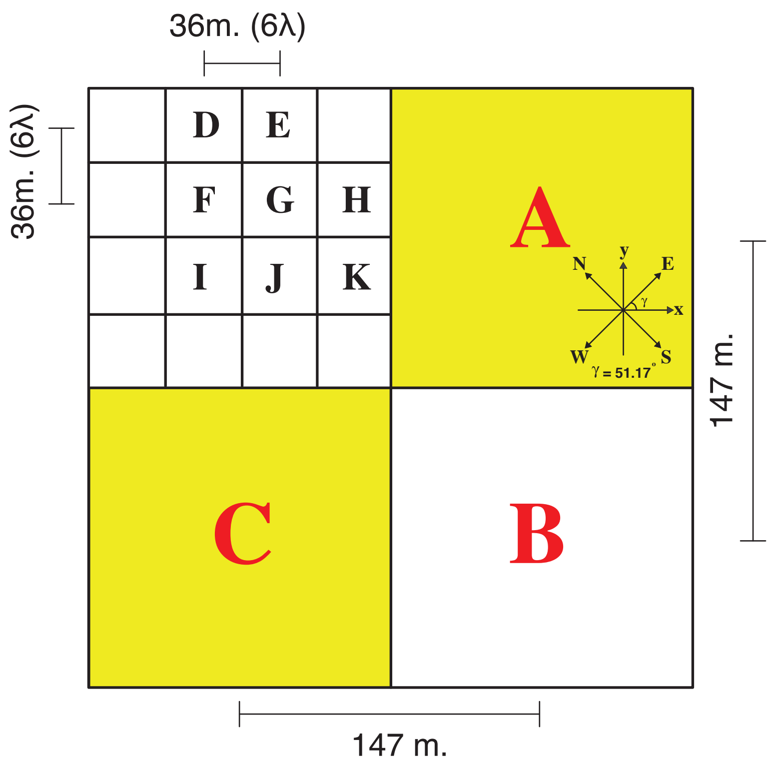

Figure 4-1. Suggested radar configuration for future meteor observations. East and West quarters were used for transmission, which are indicated in yellow. Channels A, B and C are quarter receivers while Channels D to K are module receivers. These receiving channels are of the same polarization as the transmitting quarters (NE).

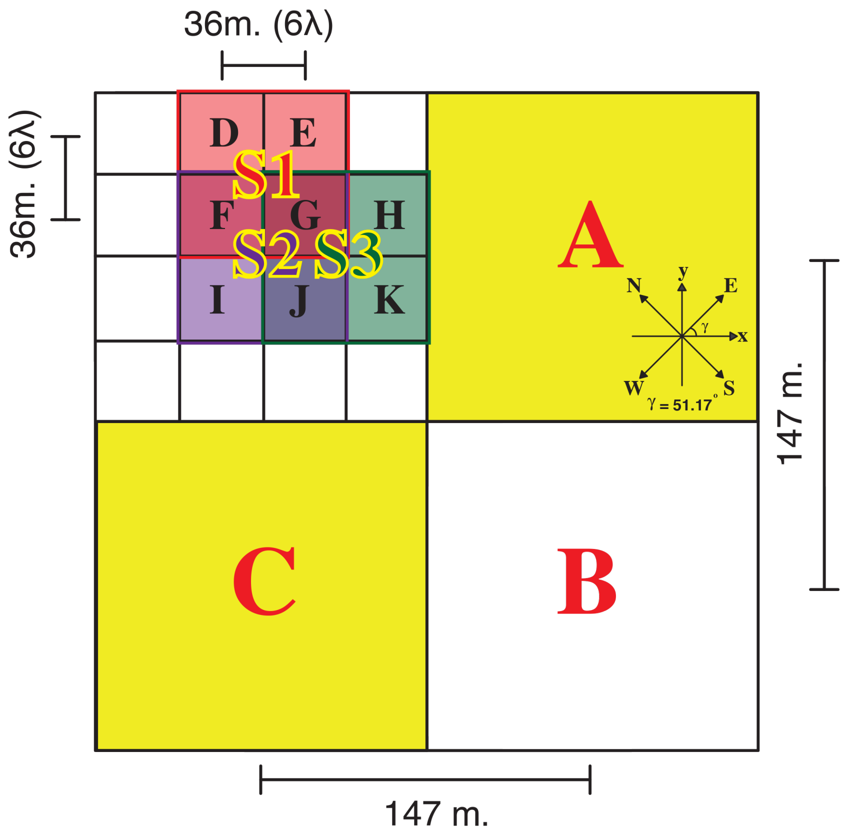

Figure 4-2. Synthetic receivers in the suggested radar configuration for future meteor observations. Receiver S1 is comprised of module receivers D, E, F, and G. Receiver S2 is comprised of module receivers F, G, I and J. Receiver S3 is comprised of module receivers G, H, J and K. The effective areas of these three synthetic receivers are quadrupled compared with one single module receiver, but the baseline spacings between two adjacent phase centers remain the same, 36 meters, as of two adjacent module receivers. Moreover, A-S1 and C-S3 form another perpendicular interferometric baselines with spacing of 151.34 meters, rotated ~13.761° clockwise with respect to the coordinates defined by the conventional Q-Q and M-M pairs.

In order to further calibration the JRO main array in future experiments, the International Space Station (ISS) flyby is highly suggested to be used to compare the radar results with its online ISS-tracker. There are many advantages of employing ISS for calibrating the JRO array:

(1) ISS is the most tracked object among all the Earth orbiters. Its information is available online, easy to access.

(2) ISS's orbit is closer to the earth surface. And it is the largest man-made object orbiting the Earth. It has strong backscattering of the radar energy to ensure analyzable return signals with high SNR.

(3) Regardless of its size, ISS can be still treated as a point target. Therefore the phase calibration results are valid for our meteor observation experiments.

This phase calibration technique using ISS flyby would apply to, but not be limited to, the JRO main array radar system. It could also be employed to calibrate other HPLA array systems having distinguishable radiation patterns and interferometric configurations to locate the targets within their beams.

References

B. B. Balsley (1964), Evidence of a stratified echoing region at 150 kilometers in the vicinity of the magnetic equator during daylight hours, Journal of Geophysical Research, 69(9), 2156-2202, 10.1029/JZ069i009p01925.

T. A. Blix, E. V. Thrane, J. Troim, and U.-P. Hoppe (1995), The role of charged aerosols in connection with noctilucent clouds and polar summer mesospheric echoes, Proceedings of 12th ESA Symposium on European Rocket and Balloon Programmes and Related Research, European Space Agency, esa SP-370, 55-60, Lillehammer, Norway,

V. A. Bronshten (1983), Physics of Meteoric Phenomena, 356 pp., D. Reidel, Dordrecht.

N. Brosch, L. S. Schijvarg, M. Podolak, and M. R. Rosenkrantz (2001), Meteor observations from Israel, *In: Proceedings of the Meteoroids 2001 Conference, 6 - 10 August 2001, Kiruna, Sweden. Ed.: Barbara Warmbein. ESA SP-495, Noordwijk: ESA Publications Division, ISBN 92-9092-805-0, 2001, p. 165 - 173*,

N. Brosch, I. Haggstrom, A. Pellinen-Wannberg, and A. Westman (2010), Unusual features in high statistics radar meteor studies at EISCAT, *MNRAS*, *401*, 1069-1079, doi: 10.1111/j.1365-2966.2009.15695.x.

N. Brosch, I. Häggström, and A. Pellinen-Wannberg (2013), EISCAT observations of meteors from the sporadic complex, *Monthly Notices of the Royal Astronomical Society*, *434*(4), 2907-2921,

D. Caswell, N. McBride, and A. Taylor (1995), Olympus end of life anomaly — a perseid meteoroid impact event?, *International Journal of Impact Engineering*, *17*(1–3), 139-150, dx.doi.org/10.1016/0734-743X(95)99843-G.

Z. Ceplecha, J. Borovicka, W. G. Elford, D. O. Revelle, R. L. Hawkes, V. Porubcan, and M. Simek (1998), Meteor phenomena and bodies, *Space Sci. Rev.*, *84*, 327-471,

E. Chapin, and E. Kudeki (1994), Radar interferometric imaging studies of long-duration meteor echoes observed at Jicamarca, *JGR*, *99*, 8937-8949, doi: 10.1029/93JA03198.

J. L. Chau, and R. F. Woodman (2004), Observations of meteor-head echoes using the Jicamarca 50MHz radar in interferometer mode, *Atmos. Chem. Phys.*, *4*(2), 511-521, 10.5194/acp-4-511-2004.

J. L. Chau, D. L. Hysell, K. M. Kuyeng, and F. R. Galindo (2008), Phase calibration approaches for radar interferometry and imaging configurations: equatorial spread F results, *Ann. Geophys.*, *26*(8), 2333-2343, 10.5194/angeo-26-2333-2008.

J. L. Chau, I. Strelnikova, C. Schult, M. M. Oppenheim, M. C. Kelley, G. Stober, and W. Singer (2014), Nonspecular meteor trails from non-field-aligned irregularities: Can they be explained by presence of charged meteor dust?, *Geophysical Research Letters*, *41*(10), 10.1002/2014GL059922.

X. Chu, Z. Yu, C. S. Gardner, C. Chen, and W. Fong (2011), Lidar observations of neutral Fe layers and fast gravity waves in the thermosphere (110–155 km) at McMurdo (77.8°S, 166.7°E), Antarctica, *GRL*, *38*, L23807, doi: 10.1029/2011GL050016.

S. Close, M. Oppenheim, S. Hunt, and L. Dyrud (2002), Scattering characteristics of high-resolution meteor head echoes detected at multiple frequencies, *JGR*, *107*, SIA 9-1 - SIA 9-12, doi: 10.1029/2002JA009253.

S. Close, P. Brown, M. Campbell-Brown, M. Oppenheim, and P. Colestock (2007), Meteor head echo radar data: Mass–velocity selection effects, *Icarus*, *186*(2), 547-556, dx.doi.org/10.1016/j.icarus.2006.09.007.

S. Close, P. Colestock, L. Cox, M. C. Kelley, and N. Lee (2010), Electromagnetic Pulses Generated by Meteoroid Impacts on Spacecraft, *J. Geophys. Res.*, *115*(A12), 2156-2202, doi:10.1029/2010JA015921.

S. Close, I. Linscott, N. Lee, T. Johnson, D. Strauss, A. Goel, Al. Fletcher, D. Lauben, R. Srama, A. Mocker, and S. Bugiel (2013), Detection of electromagnetic pulses produced by hypervelocity micro particle impact plasmas, *Physics of Plasmas*, *20*(9), 092102, dx.doi.org/10.1063/1.4819777.

J. Curtius, R. Weigel, H. J. Vössing, H. Wernli, A. Werner, C. M. Volk, P. Konopka, M. Krebsbach, C. Schiller, A. Roiger, H. Schlager, V. Dreiling, and S. Borrmann (2005), Observations of meteoric material and implications for aerosol nucleation in the winter Arctic lower stratosphere derived from in situ particle measurements, *Atmos. Chem. Phys.*, *5*(11), 3053-3069, 10.5194/acp-5-3053-2005.

T. L. Eckersley (1937), Irregular ionic clouds in the E-layer of the ionosphere, *Nature*, *140*, 846-847,

P. Erickson, F. Lind, S. Wendelken, and M. Faubert (2001), Meteor head echo observations using the Millstone Hill UHF incoherent scatter radar system, *Proceedings of the Meteoroids 2001 Conference, 6 - 10 August 2001, Kiruna, Sweden.*, 457 - 463,

D. T. Farley, and D. L. Hysell (1996), Radar measurements of very small aspect angles in the equatorial ionosphere, *J. Geophys. Res.*, *101*(A3), 5177–5184, doi:10.1029/95JA02640.

B. Gao, and J. D. Mathews (2015a), High-altitude meteors and meteoroid fragmentation observed at the Jicamarca Radio Observatory, *Monthly Notices of the Royal Astronomical Society*, *446*(4), 3404-3415,

B. Gao, and J. D. Mathews (2015b), Phase and pattern calibration of the Jicamarca Radio Observatory radar using satellites, *Monthly Notices of the Royal Astronomical Society*, *446*(4), 3416-3426,

C. Haldoupis, M. C. Kelley, G. C. Hussey, and S. Shalimov (2003), Role of unstable sporadic-E layers in the generation of midlatitude spread F, *JGR*, *108*, 1446, doi:1410.1029/2003JA009956,

J. S. Hey, S. J. Parsons, and G. S. Stewart (1947a), Radar Observations of the Giacobinid Meteor Shower, 1946, *Monthly Notices of the Royal Astronomical Society*, *107*(2), 176-183, 10.1093/mnras/107.2.176.

J. S. Hey, S. J. Parsons, and G. S. Stewart (1947b), Radar observations of the Giacobinid meteor shower, *MNRAS*, *107*, 176-183,

P. H. Hildebrand, and R. S. Sekhon (1974), Objective Determination of the Noise Level in Doppler Spectra, *Journal of Applied Meteorology*, *13*(7), 808-811, 10.1175/1520-0450(1974)013<0808:ODOTNL>2.0.CO;2.

J. Jones, A. R. Webster, and W. K. Hocking (1998), An improved interferometer design for use with meteor radars, *Radio Science*, *33*(1), 55-65, 10.1029/97RS03050.

T. J. Kane, and C. S. Gardner (1993), Lidar observations of the meteoric deposition of mesospheric metals, *Science*, *259*, 1297-1300,

J. Kero, C. Szasz, T. Nakamura, T. Terasawa, H. Miyamoto, and K. Nishimura (2012), A meteor head echo analysis algorithm for the lower VHF band, *Ann. Geophys.*, *30*(4), 639-659, 10.5194/angeo-30-639-2012.

T. Khayrov (2009), Investigation of meteor altitude distributions with the EISCAT incoherent scatter radars, MS thesis, 85 pp, Luleå University of Technology, Kiruna Sweden.

P. Koten, P. Spurný, J. Borovička, and R. Štork (2001), Extreme beginning heights for non-Leonid meteors, Proceedings of Meteoroids 2001, Noordwijk: ESA Publications Division, ESA SP-495, 119-122, Kiruna, Sweden,

P. Koten, P. Spurny, J. Borovicka, S. Evans, A. Elliot, H. Betlem, R. Stork, and K. Jobse (2006), The beginning heights and light curves of high altitude meteors, *MPS*, *41*, 1305-1320,

E. Kudeki, and D. T. Farley (1989), Aspect sensitivity of Equatorial Electrojet irregularities and theoretical implications, *JGR*, *94*, 426-434,

E. Kudeki, and F. Sürücü (1991), Radar interferometric imaging of field-aligned plasma irregularities in the equatorial electrojet, *Geophysical Research Letters*, *18*(1), 41-44, 10.1029/90gl02603.

G. Li, B. Ning, W. Wan, I. M. Reid, L. Hu, X. Yue, J. P. Younger, and B. K. Dolman (2014), Observational evidence of high-altitude meteor trail from radar interferometer, *Geophysical Research Letters*, *41*(19), 2014GL061478, 10.1002/2014GL061478.

S. G. Love, and D. E. Brownlee (1993), A direct measurement of the terrestrial mass accretion rate of cosmic dust, *Science*, *262*, 550-553,

A. C. B. Lovell (1947), Electron density in meteor trails, *Nature*, *160*, 670-671,

Y. Ma, Y. He, P. Xu, and H. Zhao (2008), Observation and Research on Strong Meteor Showers and Their Catastrophic Space Weather Events, *Chinese Astronomy and Astrophysics*, *32*, 186-196,

M. W. Maier (1993), Non-uniform PRI pulse-Doppler radar, Proceedings of System Theory, 1993. Proceedings SSST '93., Twenty-Fifth Southeastern Symposium on, 164-168, 7-9 Mar 1993, 10.1109/SSST.1993.522763.

A. Malhotra, J. D. Mathews, and J. V. Urbina (2007), A radio science perspective on long duration meteor trails, *JGR*, *112*, A12303, doi:10.1029/2007JA012576.

A. Malhotra, J. D. Mathews, and J. Urbina (2008), Effect of Meteor Ionization on Sporadic-E observed at Jicamarca, *GRL*, *35*, L15106, doi:10.1029/2008GL034661.

A. Malhotra, and J. D. Mathews (2011), A statistical study of meteoroid fragmentation and differential ablation using the Resolute Bay incoherent scatter radar, *JGR*, *116*, A04316, doi:10.1029/2010JA016135.

J. D. Mathews, D. D. Meisel, K. P. Hunter, V. S. Getman, and Q. Zhou (1997), Very High Resolution Studies of Micrometeors Using the Arecibo 430 MHz Radar, *Icarus*, *126*(1), 157-169, dx.doi.org/10.1006/icar.1996.5641.

J. D. Mathews (1998), Sporadic E: Current views and recent progress, *JASTP*, *60#4*, 413-435, doi: 10.1016/S1364-6826(97)00043-6.

J. D. Mathews, D. Janches, D. D. Meisel, and Q.-H. Zhou (2001), The micrometeor mass flux into the upper atmosphere: Arecibo results and a comparison with prior estimates, *GRL*, *28*, 1929-1932, doi:10.1029/2000GL012621.

J. D. Mathews, J. Doherty, C. H. Wen, S. J. Briczinski, D. Janches, and D. D. Meisel (2003), An update on UHF radar meteor observations and associated signal processing techniques at Arecibo Observatory, *Journal of Atmospheric and Solar-Terrestrial Physics*, *65*(10), 1139-1149, dx.doi.org/10.1016/j.jastp.2003.07.009.

J. D. Mathews (2004), Radio science issues surrounding HF/VHF/UHF radar meteor studies, *Journal of Atmospheric and Solar-Terrestrial Physics*, *66*(3–4), 285-299, http://dx.doi.org/10.1016/j.jastp.2003.11.001.

J. D. Mathews, S. J. Briczinski, D. D. Meisel, and C. J. Heinselman (2008), Radio and Meteor Science Outcomes From Comparisons of Meteor Radar Observations at AMISR Poker Flat, Sondrestrom, and Arecibo, in *Advances in Meteoroid and Meteor Science*, edited by J. M. Trigo-Rodríguez, et al., pp. 365-372, Springer New York.

B. A. McIntosh (1962), The meteoric head echo, *Journal of Atmospheric and Terrestrial Physics*, *24*(4), 311-315, dx.doi.org/10.1016/0021-9169(62)90101-0.

D. W. R. McKinley, and P. M. Millman (1949), A Phenomenological Theory of Radar Echoes from Meteors, *Proceedings of the IRE*, *37*(4), 364-375, 10.1109/JRPROC.1949.231641.

D. W. R. McKinley (1955), The meteoric head echo, *J. Atmos. Terr. Phys. 2 ("Meteors" special supplement: A Symposium on Meteor Physics)*, 65-72,

D. W. R. McKinley (1961), *Meteor Science and Engineering*, 309 pp., McGraw-Hill Book Company, New York.

L. Megner, M. Rapp, and J. Gumbel (2006), Distribution of meteoric smoke – sensitivity to microphysical properties and atmospheric conditions, *Atmos. Chem. Phys.*, *6*(12), 4415-4426, 10.5194/acp-6-4415-2006.

H. Nagaoka (1929), Possibility of disturbance of radio transmissions by meteoric showers, *Proceedings of the Imperial Academy Tokyo*, *5*, 233,

D. Nesvorny, P. Jenniskens, H. F. Levison, W. F. Bottke, D. Vokrouhlicky, and M. Gounelle (2010), Cometary origin of the zodiacal cloud and carbonaceous micrometeorites: Implications for hot debris disks, *Astrophys. J.*, *713*, 816-836, doi: 10.1088/0004-637X/713/2/816.

G. R. Ochs (1965), The Large 50MC/s Dipole Array at Jicamarce Radar Observatory,

A. Olech, P. Żoładek, M. Wiśniewski, K. Fietkiewicz, M. Maciejewski, Z. Tymiński, T. Krzyżanowski, M. Krasnowski, M. Kwinta, M. Myszkiewicz, K. Polakowski, and P. Zaręba

(2013), PF191012 Myszyniec – highest Orionid meteor ever recorded, *A&A*, *557*, A89, http://dx.doi.org/10.1051/0004-6361/201321729.

E. J. Opik (1959), Physics of meteor flight in the atmosphere. , *Quarterly Journal of the Royal Meteorological Society*, *85*(365), 320-320, 10.1002/qj.49708536526.

A. Pellinen-Wannberg, and G. Wannberg (1994), Meteor observations with the European incoherent scatter UHF radar., *JGR*, *99*, 11379-11390, doi: 10.1029/94JA00274.

J. A. Pierce (1938), Abnormal Ionization in the E Region of the Ionosphere, *Radio Engineers, Proceedings of the Institute of*, *26*(7), 892-908, 10.1109/jrproc.1938.228426.

J. M. C. Plane (2012), Cosmic dust in the earth's atmosphere, *CSR*, *41*, 6507-6518, doi: 10.1039/c2cs35132c.

S. Raizada, C. M. Brum, C. A. Tepley, J. S. Friedman, J. D. Mathews, and F. T. Djuth (2015), First Simultaneous Measurements of Na and K Thermospheric Layers along with TILs from Arecibo, *GRL*, *42*, doi: 10.1002/2015GL066714.

A. Roy, J. F. Doherty, and J. D. Mathews (2007), Analyzing Radar Meteor Trail Echoes using the Fresnel Transform Technique: A Signal Processing Viewpoint, *Earth, Moon, and Planets*, *101*(1), 27-39, 10.1007/s11038-007-9147-5.

J. P. Schafer, and W. M. Goodall (1932), Observations of Kennelly-Heaviside Layer Heights during the Leonid Meteor Shower of November, 1931, *Radio Engineers, Proceedings of the Institute of*, *20*(12), 1941-1945, 10.1109/jrproc.1932.227480.

A. M. Skellett (1931), The Effect of Meteors on Radio Transmission Through the Kennelly-Heaviside Layer, *Physical Review*, *37*(12), 1668-1668, http://link.aps.org/doi/10.1103/PhysRev.37.1668.

A. M. Skellett (1932), The Ionizing Effect of Meteors in Relation to Radio Propagation, *Radio Engineers, Proceedings of the Institute of*, *20*(12), 1933-1940, 10.1109/jrproc.1932.227479.

A. M. Skellett (1938), Meteoric ionization in the E region of the ionosphere, *Nature*, *141*, 472,

P. SpurnÝ, H. Betlem, K. Jobse, P. Koten, and J. Leven (2000a), New type of radiation of bright Leonid meteors above 130 km, *Meteoritics & Planetary Science*, *35*(5), 1109-1115, 10.1111/j.1945-5100.2000.tb01497.x.

P. Spurný, H. Betlem, J. Leven, and P. Jenniskens (2000b), Atmospheric behavior and extreme beginning heights of the thirteen brightest photographic Leonid meteors from the ground-based expedition to China, *Meteoritics & Planetary Science*, *35*(2), 243-249, 10.1111/j.1945-5100.2000.tb01773.x.

J. Vierinen, J. Fentzke, and E. Miller (2014), An explanation for observations of apparently high-altitude meteors, *Monthly Notices of the Royal Astronomical Society*, *438*(3), 2406-2412,

I. P. Williams (1996), The Evolution of Meteoroid Stremas, *Physics; chemistry; and dynamics of interplanetary dust; Astronomical Society of the Pacific Conference Series; Proceedings of the 150th colloquium of the International Astronomical Union held in Gainesville; Florida; USA;* , *104*, 89,

R. F. Woodman (1971), Inclination of the geomagnetic field measured by an incoherent scatter technique, *Journal of Geophysical Research*, *76*(1), 178-184, 10.1029/JA076i001p00178.

F. Yasunori, U. Masayoshi, S. Yasuo, S. Masatoshi, K. Masao, and S. Chikara (1998), Meteor luminosity at 160 km altitude from TV observations for bright Leonid meteors, *Geophysical Reserach Letters*, *25*(3), 285-288,

Q. Zhou, J. D. Mathews, and Q. Zhou (1999), Incoherent scatter radar study of the impact of the meteoric influx on nocturnal E-region ionization, *Geophys. Res. Lett.*, *26*, 1833-1836,

Curriculum Vitae

Boyi Gao

Education: Ph.D., Electrical Engineering
The Pennsylvania State University (December, 2016)

M.S., Electrical Engineering
The Pennsylvania State University (December, 2013)

B.S., Measuring and Control Technology and Instrument
Tianjin University (July, 2010)

Publications:

B. Gao, and J. D. Mathews (2015a), High-altitude meteors and meteoroid fragmentation observed at the Jicamarca Radio Observatory, *Monthly Notices of the Royal Astronomical Society, 446(4), 3404-3415*

B. Gao, and J. D. Mathews (2015b), Phase and pattern calibration of the Jicamarca Radio Observatory radar using satellites, *Monthly Notices of the Royal Astronomical Society, 446(4), 3416-3426*

B. Gao, and J. D. Mathews (2015c), High-altitude radar meteors observed at Jicamarca Radio Observatory using a multi-baseline interferometric technique, *Monthly Notices of the Royal Astronomical Society, 452, 4252-4262*

B. Gao, and J. D. Mathews (Under Review), An alternating inter-pulse period technique for range and Doppler speed de-aliasing applied to meteor observations at Jicamarca Radio Observatory

Q. Zhu, R. Dinsmore, B. Gao, and J. D. Mathews (2016), High-resolution radar observations of meteoroid fragmentation and flaring at the Jicamarca Radio Observatory, *Monthly Notices of the Royal Astronomical Society, 457(2), 1759-1769*

Conference Proceedings:

B. Gao, and J. D. Mathews, "The confirmation of high-altitude radar meteors observed with the Jicamarca 50MHz array radar," in *Radio Science Meeting (USNC-URSI NRSM), 2014 United States National Cmmittee of URSI National, vol., no., pp.1-1, 8-11 Jan. 2014, doi: 10.1109/USNC-URSI-NRSM.2014.6928097*

B. Gao, and J. D. Mathews, J. L. Chau, "Phase and pattern calibration of the Jicamarca radar using satellites," in *Radio Science Meeting (USNC-URSI NRSM), 2013 US National Committee of URSI National, vol., no., pp.1-1, 9-12 Jan. 2013, doi: 10.1109/USNC-URSI-NRSM.2013.6525060*